TECHNISCHE UNIVERSITÄT WIEN

DIPLOMARBEIT

Lattice Defects in Edge-free Graphene Quantum Dots

zur Erlangung des akademischen Grades

Diplom-Ingenieur

im Rahmen des Studiums

Technische Physik

eingereicht von

Christoph Schattauer
Matrikelnummer 01228718

ausgeführt am Institut für Theoretische Physik
der Fakultät für Physik der Technischen Universität Wien

Betreuung
Betreuer: Ass.-Prof. Dipl.-Ing. Dr.techn. Florian Libisch
Mitwirkung: Dipl.-Ing. Lukas Linhart

Wien, 18.6.2019

(Unterschrift Verfasser) (Unterschrift Betreuer)

Contents

1. Abstract

Graphene, a single atomic layer of carbon, first successfully fabricated in 2004 by A. Geim and K Novoselov [44], has since evoked great research interest. These efforts have lead to a good fundamental understanding of the electronic structure of the rather novel two-dimensional material [27,38,46].

Despite tremendous improvement in the synthesis of graphene nanostructures [45], which enables very clean samples with low defect density and high mobility, understanding the influence of lattice defects in graphene [9,10,11,12] is often crucial to understanding the properties of a much larger system.

Quantum dots (QDOT), popularly referred to as "artificial atoms", can be viewed as effectively zero dimensional structures in which confined electrons display sharp energy levels [47]. Their promising technological applications (quantum computation, quantum cryptography,...) recently increased research efforts in this field. The presence of Klein tunneling usually restricts graphene quantum dots to hold merely quasi-bound states. However, confinement in single layer graphene via a combination of both electric (scanning tunneling microscopy tip) and magnetic fields (Landau regime) allows for so called edge-free quantum dots [1,3,16,17,18,43]. As they are regarded to be possible alternatives for conventional semiconductor quantum dots (applications such as spin qubits, etc.) they generate growing research interest in past years.

The purpose of this thesis is to investigate the interplay of the these edge-free quantum dots with various types of lattice defects in graphene [9,11,12,21,33]. We particularly focus on investigating the level spacing (orbital splitting Δ_j^O and valley splitting Δ_j^k) of the QDOT states as a function of QDOT-defect distance and determine the "character" of the respective states compared to an edge-free QDOT in pristine graphene.

We describe the system on the tight-binding level of theory and extract the onsite and hopping terms for embedding different defect types from DFT supercell calculations (VASP, [39,40,41,42]) via wannier90 [6,7,8]. Aside from the "static" properties of such QDOT-defect systems we also investigate transition dynamics between QDOT states using time propagation by Magnus operators [32] and compare with analytical predictions (Landau Zener theory, [19,20]).

1. Abstract

Promising outlooks for the role of graphene in future spintronics applications (long spin life times and high spin mobility [5,10,48]) make the single vacancy defect (with its local magnetic moment) an interesting type of lattice defect in graphene. Our efforts to add the single vacancy defect to our "portfolio of wannierized graphene lattice defects" resonate with recent scientific work [35,36,37] and opens the possibility for modeling spin scattering in defect afflicted graphene in future projects.

2. Theory and Method

We very briefly introduce the theoretical framework of the methods necessary for this master thesis. After a brief introduction in density functional theory (DFT) we review the concept of maximally localized Wannier functions (MLWF). The specific way of embedding our "wannierized defects" into a substantially larger flake of pristine graphene via a tight-binding formalism is addressed as well.

2.1. Density Functional Theory DFT

2.1.1. Introduction

Investigating systems at the nanoscale usually necessitates modeling atomic interactions as accurately as possible while simultaneously keeping the computational effort manageable. Empirical interatomic potentials which are fitted to reproduce some measured quantity as accurately as possible are one of the more straightforward entry points to computational materials science. Unfortunately their ability to reproduce physical properties different from those they were designed for can be quite limited. Since all such theories that rely heavily on implicit assumptions for the type of chemical bonding and other degrees of freedom face problems when applied to systems showing chemical complexity, the intellectually more appealing choice are so called "ab initio" methods. These methods, such as density functional theory (DFT), start from basic principles of quantum theory to describe a system without prior knowledge and are thus predictive.

Since a straightforward solution of the many-body Schrödinger equation $\hat{H}\,|\Psi\rangle = E\,|\Psi\rangle$ is virtually impossible for systems of interest, approximations such as Hartree-Fock or DFT are the standard approach. The main problem is that the many-electron wavefunction $\Psi(\vec{r}_1, \sigma_1, ..., \vec{r}_N, \sigma_N)$ is a complex scalar field that depends on $3N$ spatial coordinates. Hartree-Fock simplifies this by introducing slater determinants of N single particle wavefunctions which corresponds to solving N coupled one-electron equations with a self-consistent potential V_i for the orbital Φ_i that depends on the other $N-1$ orbitals.

DFT, [13,15], solves the scaling problem in a different manner altogether, since it focuses on uniquely describing a system with a quantity whose complexity grows much slower (if not at all) with system size. The Hohenberg-Kohn theorems prove the electron density to fulfill such a uniqueness relation. Since the electron density $\rho(\vec{r})$ depends only on the spatial coordinates and does not encode degrees of freedom of individual particles it circumvents the scaling problem altogether.

2.1.2. Hohenberg-Kohn Theorems

Let us consider the non relativistic limit of a spin-compensated system of N-electrons subject to an external potential $V_{\text{ext}}(\vec{r})$. The Hamiltonian of such a system can be written as:

$$\hat{H} = \sum_{i=1}^{N} \Big[-\frac{\vec{p}_i^{\,2}}{2m} + V_{\text{ext}}(\vec{r}_i) \Big] + \sum_{i>j} \frac{e^2}{|\vec{r}_i - \vec{r}_j|} \tag{2.1}$$

Conventionally the electron density $\rho(\vec{r})$ is determined after solving for the wavefunction $|\Psi\rangle$ via:

$$\rho(\vec{r}) = \langle\Psi| \sum_{i=1}^{N} \delta(\vec{r} - \vec{r}_i) \, |\Psi\rangle \tag{2.2}$$

This "$\hat{H} \rightarrow \rho(\vec{r})$" procedure is fairly straightforward. It is however also possible to go "backwards", that is "$\rho(\vec{r}) \rightarrow \hat{H}$".

If one, for the sake of simplicity, considers an isolated atom whose ground state electron density $\rho_0(\vec{r})$ is known we can derive the 3 parameters Z, N and $\vec{R}$ that uniquely define our Hamiltonian, which will inevitably be of the following form:

$$\hat{H} = \sum_{i=1}^{N} \Big[-\frac{\vec{p}_i^{\,2}}{2m} - \frac{Ze^2}{|\vec{r}_i - \vec{R}|} \Big] + \sum_{i>j} \frac{e^2}{|\vec{r}_i - \vec{r}_j|} \tag{2.3}$$

The total number of electrons N, is simply given by $\int \rho_0(\vec{r}) d^3r$ while the nucleus position $\vec{R}$ is the position at which the density displays the cusp singularity. The remaining parameter Z can be associated with the radial density derivative at the cusp:

$$Z = -\left(\frac{a_0}{2\rho_0(\vec{r})} \frac{\partial \rho_0(\vec{r})}{\partial r} \right)_{\vec{r} \rightarrow \vec{R}} \tag{2.4}$$

The proof that this cannot only be done for the Coulomb interaction (Kato theorem) but for a general external potential was given by Hohenberg and Kohn in 1964. Their two theorems read:

1) The external potential $V_{ext}(\vec{r})$ as well as the total energy E are unique functionals of the non-degenerate ground state electron density $\rho(\vec{r})$.

Proof by Contradiction:

Assume two different external potentials $V_1(\vec{r})$, $V_2(\vec{r})$ yielding the same ground state density $\rho(\vec{r})$ realized by both Ψ_1 as well as Ψ_1. The two Hamiltonians, which share the same kinetic part $\hat{T}$ and electron-electron interaction $\hat{C}$ read:

$$\hat{H}_1 = \hat{T} + \hat{C} + V_1(\vec{r}) \tag{2.5}$$

$$\hat{H}_2 = \hat{T} + \hat{C} + V_2(\vec{r}) \tag{2.6}$$

Computing both ground state energies yields:

$$E_1 = \langle \Psi_1 | \hat{H}_1 | \Psi_1 \rangle < \langle \Psi_2 | \hat{H}_1 | \Psi_2 \rangle = E_2 + \int \rho(\vec{r}) \cdot \Big[V_1(\vec{r}) - V_2(\vec{r}) \Big] d\vec{r} \tag{2.7}$$

$$E_2 = \langle \Psi_2 | \hat{H}_2 | \Psi_2 \rangle < \langle \Psi_1 | \hat{H}_2 | \Psi_1 \rangle = E_1 + \int \rho(\vec{r}) \cdot \Big[V_2(\vec{r}) - V_1(\vec{r}) \Big] d\vec{r} \tag{2.8}$$

Adding (2.7) and (2.8) yields the contradiction $E_1 + E_2 < E_1 + E_2$ which in turn proves the existence of said unique mapping between external potential and viable electron densities. The first theorem can also be viewed as a Legendre transformation that allows one to express the total energy as a function of the density rather than of a potential.

2) $E[\rho]$ is minimized when ρ approaches the exact ground state density.

This second part generalizes the variational principle from wave functions to densities and naturally follows from the first theorem.

It has been shown that even in the presence of degenerate ground states a unique functional $E[\rho]$ still exists.

2.1.3. Energy functionals

The Hohenberg-Kohn theorems, despite very powerful, merely state the existence of a unique energy functional, yet provide no clue whatsoever about its form. Let us review the construction of the most simple (and by todays standards most seldom used) energy functional, the Thomas-Fermi-Hartree functional $E^{\mathrm{TFH}}[\rho]$. Starting from our non-relativistic N-electron Hamiltonian (2.1) we have to rewrite the three expressions in terms of the density.

The external-potential and the Coulomb contribution can, albeit with some approximations, be brought to:

$$E_{\mathrm{ext}}[\rho] = \int V_{\mathrm{ext}}(\vec{r})\rho(\vec{r})d\vec{r} \tag{2.9}$$

$$E_{\mathrm{Coulomb}}[\rho] \approx \frac{e^2}{2}\int\int \frac{\rho(\vec{r})\rho(\vec{r}')}{|\vec{r}-\vec{r}'|}d\vec{r}d\vec{r}' \tag{2.10}$$

The two major shortcomings of (2.10) involve firstly that we consider an electron distribution given by classical charges (as in Hartree theory) and secondly that we erroneously include the electron self interaction (which is circumvented by the $i > j$ constraint for the sum in (2.1)). It turns out reformulating the kinetic part is also not trivial at all. If we, for the sake of simplicity, consider the exceedingly simple reference system of a homogeneous electron gas we can obtain a kinetic energy functional by comparison of $E = \int_0^{E_F} \epsilon D(\epsilon)d\epsilon = V2^{3/2}(\sqrt{5}\pi)^{-2}E_F^{5/2}$ and $\rho = \int_0^{E_F} D(\epsilon)d\epsilon = 2^{3/2}(\sqrt{3}\pi)^{-2}E_F^{3/2}$. This leads to $T[\rho] = \alpha\int \rho^{5/3}d\vec{r}$, with some irrelevant constant α. The very crude approximation of generalizing this expression to non-constant $\rho(\vec{r})$ leads to:

$$T[\rho] = \alpha\int \rho(\vec{r})^{5/3}d\vec{r} \tag{2.11}$$

While this approximation can — to at least some extent — be justified for very slowly varying $\rho(\vec{r})$, it will, in general, yield only mediocre results at best.

With this we can collect the terms to form the "complete" Thomas-Fermi-Hartree energy functional:

$$E^{\mathrm{TFH}}[\rho] \coloneqq \alpha\int \rho(\vec{r})^{5/3}d\vec{r} + \int V_{\mathrm{ext}}(\vec{r})\rho(\vec{r})d\vec{r} + \frac{e^2}{2}\int\int \frac{\rho(\vec{r})\rho(\vec{r}')}{|\vec{r}-\vec{r}'|}d\vec{r}d\vec{r}' \tag{2.12}$$

Now that we have successfully expressed the total energy as a function of the density we can determine the ground state density. We have to restrain our minimization to densities that correspond to the fixed total number of electrons $\int \rho(\vec{r})d\vec{r} = N$ via Lagrange multiplier μ:

$$\frac{\delta}{\delta\rho(\vec{r})}\left[E^{\mathrm{TFH}}[\rho] - \mu\int\rho(\vec{r})d\vec{r}\right] = \frac{\delta E^{\mathrm{TFH}}[\rho]}{\delta\rho(\vec{r})} - \mu = 0 \tag{2.13}$$

2.1.4. Kohn Sham equations

There is an alternative way of computing the ground state density that includes solving one-particle equations instead of minimizing the energy functional directly. For the next part we introduce the kinetic energy of a virtual system of N non-interacting electrons (with the exact same density as the interacting one) $T_s[\rho]$. We can now write the exact kinetic energy of our interacting system of interest as $T[\rho] = T_s[\rho] + T_c[\rho]$ and treat the correction $T_c[\rho]$ as a marginal contribution. In a similar way the exact Coulomb term can be decomposed into Hartree term plus correction term $E_{\mathrm{Coulomb}}[\rho] = E_H[\rho] + \Delta E[\rho]$. Combining both correction terms we can introduce the exchange-correlation energy functional:

$$E_{\mathrm{XC}}[\rho] = T_c[\rho] + \Delta E[\rho] \tag{2.14}$$

This functional includes:

- exchange effects (Pauli repulsion between electrons of the same spin)
- compensation for the spurious self interaction in E_H
- correlation effects (tendency for electrons of different spin to mutually avoid each other)

Since E_{XC} does not depend on the external potential (it depends only on the density), once found, it should be equally valid for all materials and can be decomposed into $E_{\mathrm{XC}}[\rho] = E_X[\rho] + E_C[\rho]$. The exchange part can be explicitly written in terms of one-particle orbitals that are put into the Slater determinant (2.15).

$$E_X\left[\{\phi\}\right] = \frac{e^2}{2}\sum_{i,j}\int\int\frac{\phi_i(\vec{r})\phi_j(\vec{r}')\phi_i(\vec{r}')\phi_j(\vec{r})}{|\vec{r}-\vec{r}'|}d\vec{r}d\vec{r}' \tag{2.15}$$

However formulating it as a functional of the electron density is a very difficult problem that for the most part can only be done exactly for very academic systems such as the homogeneous electron gas (HEG). The remaining correlation term accounts for the so called Coulomb hole which describes the depression in electron density around another electron. Both exchange and correlation can be properly treated with diagrammatic techniques in many-body theory (which leaves the realm of mean-field theories such as DFT). The two most fundamental — and still widely used — approximations for E_{XC} are I) The Local Density Approximation and II) The Generalized Gradient Approximation.

I) The Local Density Approximation (LDA)

This approximation is very similar to the approach taken for E^{TFH}. It relies on the assumption that expressions derived for the homogeneous electron gas (HEG) have the same functional dependence on the electron density as the ones for inhomogeneous systems:

$$E_{\mathrm{XC}}^{\mathrm{LDA}}[\rho] = \int E_{\mathrm{XC}}^{\mathrm{HEG}}[\rho(\vec{r})]d\vec{r} \tag{2.16}$$

Surprisingly, this approximation produces relatively reasonable results even for systems that are far from homogeneous, due to conserving the so called sum rule of the exchange correlation hole $\int \rho_{\mathrm{XC}}(\vec{r},\vec{r}')d\vec{r}' = -1$ which leads to some degree of error compensation (LDA usually overestimates E_X while underestimating E_C). Unsurprisingly LDA also comes with some mayor deficits, some of which include:

- LDA tends to overbind
- electrons are generally too delocalized
- long-range effects are inherently not included
- the ubiquitous hydrogen bond is poorly accounted for

II) The Generalized Gradient Approximation (GGA)

A first attempt to improve LDA by expansion in terms of the density gradient ($\nabla\rho(\vec{r})$,..) resulted in a much worse description due to low density regions in which the gradient expansion tends to diverge. The fact that truncated gradient expansions would no longer fulfill the sum rule also meant that no error cancellation could occur. Using functionals of both density and gradient (generalized gradient approx.) finally improved the results:

$$E_{\mathrm{XC}}^{\mathrm{GGA}}[\rho] = E_{\mathrm{XC}}^{\mathrm{LDA}}[\rho] + \int e_{\mathrm{XC}}[\rho(\vec{r}),\nabla\rho(\vec{r})]d\vec{r} \tag{2.17}$$

The term for e_{XC} would then be either fitted to a set of molecule calculations performed with accurate many-body methods and/or analytically constructed in ways that conserve the sum rule while neglecting contributions from regions that would lead to divergences. The main characteristics of GGA include:

- GGA can overcorrect LDA
- GGA is better suited for XC-effects in spatially small systems (atoms, molecules,..)
- hydrogen bonds are well accounted for while long range effects are still missing
- strongly correlated systems are still out of reach

Our total energy functional now reads

$$E[\rho] = T_s[\rho] + \int V_{\mathrm{ext}}(\vec{r})\rho(\vec{r})d\vec{r} + E_H[\rho] + E_{\mathrm{XC}}[\rho] \tag{2.18}$$

while the variation with respect to the density yields

$$\frac{\delta E[\rho]}{\delta\rho(\vec{r})} = \frac{\delta T_s[\rho]}{\delta\rho(\vec{r})} + V_{\mathrm{ext}}(\vec{r}) + \frac{\delta E_H[\rho]}{\delta\rho(\vec{r})} + \frac{\delta E_{\mathrm{XC}}[\rho]}{\delta\rho(\vec{r})} \stackrel{!}{=} \mu \tag{2.19}$$

The ingenious conjecture of Kohn and Sham was that for any system of N interacting electrons ($\mathbb{S}_i$) with given potential $V_{ext}(\vec{r})$ there exists a system of N non-interacting electrons ($\mathbb{S}_n$), with the exact same density ρ, that is obviously subject to a different external potential $V_{single}(\vec{r})$.

$$\frac{\delta E[\rho]}{\delta\rho(\vec{r})} = \frac{\delta T_s[\rho]}{\delta\rho(\vec{r})} + V_{\mathrm{single}}(\vec{r}) \stackrel{!}{=} \mu \tag{2.20}$$

If we now look at the variational equation of $\mathbb{S}_n$ (2.19) and compare to that of $\mathbb{S}_i$ (2.20) we find a simple criterion for them to coincide (2.21):

$$V_{\mathrm{single}}(\vec{r}) \stackrel{!}{=} V_{\mathrm{ext}}(\vec{r}) + \frac{\delta E_H[\rho]}{\delta\rho(\vec{r})} + \frac{\delta E_{\mathrm{XC}}[\rho]}{\delta\rho(\vec{r})} \tag{2.21}$$

In principle, whenever (2.21) is fulfilled the solutions ρ and ρ_n for $\mathbb{S}_i$ and $\mathbb{S}_n$ respectively, are identical too. However, we still lack an explicit expression for the kinetic part $T_s[\rho]$ for a general inhomogeneous system. In contrast to that it is quite straightforward to solve $\mathbb{S}_n$ in the form of N non-interacting Schrödinger-like equations (2.22) and use the virtual single-particle orbitals to construct a density via an occupation weighted sum (2.23).

$$\Big[-\frac{\hbar^2\nabla^2}{2m} + V_{\text{single}}(\vec{r})\Big]\phi_n(\vec{r}) = \epsilon_n\phi_n(\vec{r}) \tag{2.22}$$

$$\rho_n(\vec{r}) = \sum_i f_i|\phi_i(\vec{r})|^2 \tag{2.23}$$

These are the famous Kohn-Sham equations, that while at first glance similar to a set of Schrödinger equations, contain V_{single} according to (2.21) and are thus non-linear. The usual approach is to solve them self-consistently starting from an initial guess for either density ρ or potential $V_{\text{single}}(\rho)$.

In general the Kohn-Sham eigenvalues ϵ_n lack physical meaning altogether. They are technically equivalent to Lagrange multipliers that provide the orthogonality between any two Kohn-Sham orbitals ϕ of $\mathbb{S}_n$. The only one to have physical meaning is the highest occupied one, since this theoretically represents the chemical potential of the system (quite often approximations for E_{XC} usually falsify this property).

2.1.5. Spin-polarized calculations

While having completely ignored the spin degree of freedom until now (our occupation numbers f_i in (2.23) range from 0 to 2, to compensate for that) it is no big deal to expand the formalism to non spin compensated systems. Instead of only specifying the total number of electrons N, we now fix initial values for $N_\uparrow$ as well as $N_\downarrow$ (while respecting $N_\downarrow + N_\uparrow = N$) and simply solve a set of Kohn-Sham equations for each spin component. The exchange-correlation energy will now depend on both $\rho(\vec{r}) = \rho_\uparrow(\vec{r}) + \rho_\downarrow(\vec{r})$ as well as $\sigma(\vec{r}) = \rho_\uparrow(\vec{r}) - \rho_\downarrow(\vec{r})$.

2.1.6. Pseudo-potentials

Many problems in physics allow a distinction in so called "active electrons" and "spectator electrons" by various criteria (considerably different energy scales, localized in different regions of space, etc.). Condensed matter physics usually defines the valence electrons of an atom as "active" since they are responsible for chemical bonding. Core electrons lie energetically well below the valence orbitals and are hence considered dormant. In order to reduce computational effort the influence of the core electrons will henceforth be encoded into an operator, a so called pseudo-potential.

Assembling an all-electron valence orbital $|\Psi_V\rangle$ (eigenenergy ϵ_V) as a linear combination of a smoothened pseudo orbital $|\Phi_V\rangle$ and core orbitals $|\Psi_C\rangle$ (eigenenergies ϵ_C):

$$|\Psi_V\rangle = |\Phi_V\rangle + \sum_C a_{C,V} |\Psi_C\rangle \tag{2.24}$$

Since $|\Psi_V\rangle$ and $|\Psi_C\rangle$ are both solutions to Schrödinger's equation it is straigthforward to arrive at:

$$\left[\hat{H} + \sum_C (\epsilon_V - \epsilon_C) |\Psi_C\rangle \langle\Psi_C|\right] |\Phi_V\rangle = \epsilon_V |\Phi_V\rangle \tag{2.25}$$

The Hamiltonian is extended by a non-local, repulsive, short ranged projector $\sum_C (\epsilon_V - \epsilon_C) |\Psi_C\rangle \langle\Psi_C|$, the pseudo potential. This formalism speeds things up by firstly reducing the number of KS orbitals in need of determination and secondly omitting the representation of rapidly oscillating all-electron valence orbitals (which arise from staying orthogonal to the core states). Pseudo potential choice is heavily intertwined with basis choice. A plane-wave basis usually requires "soft" pseudo potentials (its Fourier transform features a most compact support) to be computationally most efficient.

2.1.7. K-point sampling

There are systems of interest that behave invariant under translations in certain directions (periodic systems) that have consequences for their numerical treatment via DFT. In periodic systems, such as crystals, Bloch's theorem tells us that while the electronic density — as a physical observable — has to respect the periodicity exactly, the wavefunction needs only be periodic up to a unimodular phase:

$$\Psi(\vec{r} + \vec{R}) = e^{i\vec{k}\vec{R}} \Psi(\vec{r}) \tag{2.26}$$

The density of $\vec{k}$ vectors in the first Brilouin zone (BZ) is given by $\frac{V_c}{(2\pi)^D}$ with dimension D and unit cell volume V_c. Increasing system size thus leads to dense $\vec{k}$ points. Unsurprisingly, numerical treatment of such systems is restricted to a finite number of $\vec{k}$ points and will computationally benefit from including as few as necessary when calculating $\vec{k}$-dependent averages over the BZ (e.g. real space electron density, see (2.27)).

$$\rho(\vec{r}) = \sum_i \int_{BZ} f_{i,\vec{k}} |\Psi_{i,\vec{k}}(\vec{r})|^2 d\vec{k} \tag{2.27}$$

Since the Kohn Sham equations for different $\vec{k}$ points are completely decoupled we solve them independently and need only find a way of sufficiently sampling the BZ as efficiently as possible. For this purpose various strategies (special point technique — suited for smoothly varying functions within the BZ —, tetrahedron method — a simplex method for interpolation that takes the shape of the Fermi surface into account —, etc.) are readily available in modern DFT codes (in our case VASP).

2.1.8. Geometry Optimization

While DFT is a well developed tool for calculating the ground state density and the corresponding energy for a system of N electrons, experimental measurements usually provide insights into the response of a system to external change (for example the change in volume due to external pressure). The Hohenberg-Kohn theorems introduce the total energy of a system as a functional of the electronic density while concealing the parametric dependence on some external quantities λ (volume or shape of the unit cell, number and positions of atoms,...).

In order to make this dependence more obvious we henceforth note the total energy functional as $E_\lambda[\rho]$. For any given set of parameters λ the previously described standard DFT methods suffice for determining the ground state density ρ_λ. If we want to know how the total energy responds to variations of λ we will generally be interested in an n-th order derivative of the form $\frac{\delta^n E}{\delta \lambda^n}$.

We shall restrain our views to first order derivatives with special attention to atomic forces since they are most relevant for this thesis. Keeping ionic positions of a system fixed with predefined values (as we have considered up until now) will in general not lead to physically correct equilibrium configurations. In order to derive a scheme for ionic relaxation we must first introduce the total Hamiltonian of a system that depends on both electronic $\{\vec{r}_j\}$ and ionic $\{\vec{R}_i\}$ degrees of freedom:

$$\underbrace{\left[\hat{H}_e + \hat{T}_n + \hat{V}_n\right]}_{\hat{H}_{e+n}} |\Phi_{\{\vec{R}_i\},\{\vec{r}_j\}}\rangle = \mathbb{E}\, |\Phi_{\{\vec{R}_i\},\{\vec{r}_j\}}\rangle \tag{2.28}$$

This description includes the previously used electronic part $\hat{H}_e$, the kinetic energy of the nucleii $\hat{T}_n$ and the Coulomb interaction of the ions $\hat{V}_n$ which are detailed below:

$$\hat{H}_e = \sum_{i=1}^{N} \Big[-\frac{\hat{p}_i^2}{2m} + V_{\text{ext}}(\vec{r}_i, \{\vec{R}_j\}) \Big] + \sum_{i>j} \frac{e^2}{|\vec{r}_i - \vec{r}_j|} \tag{2.29}$$

$$\hat{T}_n = \sum_{i=1}^{N} \Big[-\frac{\hat{P}_i^2}{2M} \Big] \tag{2.30}$$

$$\hat{V}_n = \sum_{I>J} \frac{Z_I Z_J e^2}{|\vec{R}_I - \vec{R}_J|} \tag{2.31}$$

Employing a product ansatz from Born and Oppenheimer of the form $|\Phi_{\{\vec{R}_i\},\{\vec{r}_j\}}\rangle \coloneqq |\chi_{\{\vec{R}_i\}}\rangle \cdot |\theta_{\{\vec{R}_i\},\{\vec{r}_j\}}\rangle$ for the whole wave function and dropping some terms proportional to the ratio of masses m/M we end up at:

$$\hat{H}_e \, |\theta_{\{\vec{R}_i\},\{\vec{r}_j\}}\rangle = E(\{\vec{R}_I\}) \, |\theta_{\{\vec{R}_i\},\{\vec{r}_j\}}\rangle \tag{2.32}$$

and

$$\Big[\hat{T}_n + \hat{V}_n + E(\{\vec{R}_I\})\Big] \, |\chi_{\{\vec{R}_i\}}\rangle = \mathbb{E} \, |\chi_{\{\vec{R}_i\}}\rangle \tag{2.33}$$

The Schrödinger eqaution for the ionic wave function is now equipped with the potential energy surface $E(\{\vec{R}_I\})$ which describes the energy contribution from the electronic system. Under the assumption that the electronic system reacts perfectly adiabatically to changes in the nuclear system it would now suffice to minimize $\hat{V}_n + E(\{\vec{R}_I\})$ to find the equilibrium of atomic positions.

For such purposes calculating the atomic forces, that is the first order derivative of the total potential energy $\hat{V}_n + E(\{\vec{R}_I\})$ with respect to atomic positions $\vec{f}_{R_I} \coloneqq -\nabla_{R_I} \Big[\hat{V}_n + E(\{\vec{R}_I\})\Big]$, would simply be unfeasible for systems of interesting size.

There is however quite a clever alternative that makes use of the variational principle of DFT: substituting the eigenvalue $E(\{\vec{R}_I\})$ with the energy functional of DFT $E_{\vec{R}_I}[\rho]$ that only parametrically depends on ionic coordinates allows for

$$\vec{f}_I = -\frac{dV_n}{d\vec{R}_I} - \frac{dE_{\vec{R}_I}[\rho]}{d\vec{R}_I} \tag{2.34}$$

with

$$\frac{dE_{\vec{R}_I}[\rho]}{d\vec{R}_I} = \frac{\partial E_{\vec{R}_I}[\rho]}{\partial \vec{R}_I} + \int \underbrace{\frac{\delta E_{\vec{R}_I}}{\delta\rho(\vec{r})}}_{\mu} \frac{\partial\rho(\vec{r})}{\partial\vec{R}_I} d\vec{r} = \frac{\partial E_{\vec{R}_I}[\rho]}{\partial \vec{R}_I} + \mu \frac{\partial}{\partial \vec{R}_I} \underbrace{\int \rho(\vec{r}) d\vec{r}}_{N:=\text{const.}} \tag{2.35}$$

We thus find that the total and partial derivative simply coincide:

$$\frac{dE_{\vec{R}_I}[\rho]}{d\vec{R}_I} = \frac{\partial E_{\vec{R}_I}[\rho]}{\partial \vec{R}_I} \tag{2.36}$$

This general result known as the Hellman-Feynman theorem tells us that we need not determine the change of ρ with respect to any general external parameter λ. The ionic forces (which have to be evaluated with a converged ground state density) are then simply:

$$\vec{f}_I = -\frac{\partial(V_n + V_{ext})}{\partial \vec{R}_I} \tag{2.37}$$

This means we can electronically converge our system with some initial ionic positions using DFT, update our ionic positions according to the nuclear forces and continue with this twofold process until total convergence is acquired.

2.2. Wannierization

Solving for the ground state of periodic crystalline structures is often done in terms of Bloch orbitals $\Psi_{n,\vec{k}}(\vec{r})$. Here n denotes the corresponding band index and $\vec{k}$ the momentum. For some applications a different representation in terms of orbitals, localized in real space, so called Wannier functions, is preferable. These Wannier functions have been widely established in the analysis of excitons, binding forces acting on electrons and generally provide an elegant way to calculate tight binding parameters (which will be our main interest). A much more thorough introduction into the Wannier representation than is attempted here can be found in [6, 7, 8].

These Wannier functions $w_n(\vec{r} - \vec{R})$ can be formally defined via a Fourier transformation of the Bloch orbitals and carry again a band index n and the lattice vector $\vec{R}$ pointing to their corresponding unit cell of origin. In bra-ket notation we can write a Wannier function, $|\vec{R}, n\rangle$, as:

$$|\vec{R}, n\rangle = \frac{V}{(2\pi)^3} \int e^{-i\vec{k}\cdot\vec{R}} \, |n, \vec{k}\rangle \, d\vec{k} \tag{2.38}$$

Vice versa the Bloch orbitals, $|n, \vec{k}\rangle$ can be expanded in a "Fourier series" with the Wannier functions as their Fourier components:

$$|n, \vec{k}\rangle = \sum_{\vec{R}} e^{-i\vec{k}\cdot\vec{R}} \, |\vec{R}, n\rangle \tag{2.39}$$

It is important to realize that Wannier functions are by no means unique, since within a single band the choice of $\vec{k}$-dependent phases $f(\vec{k})$ for Bloch orbitals will result in another, equally valid set of Bloch orbitals:

$$|u_{m,\vec{k}}\rangle \to e^{if(\vec{k})} \, |u_{m,\vec{k}}\rangle \tag{2.40}$$

This freedom generalizes for "composite bands" (several bands connected by degeneracies) to a unitary transformation mixing several Bloch states and shall henceforth be referred to as "gauge freedom".

$$|u_{n,\vec{k}}\rangle \to \sum_{\vec{k}} U_{mn}(\vec{k}) \, |u_{m,\vec{k}}\rangle \tag{2.41}$$

Since the bands of interest will most often be intersected by bands that are to be neglected, the situation of non isolated bands will be the generic case. The problem of identifying which Kohn Sham eigenvalues correspond to which band thus poses certain problems in "crowded" regions where a vast number of bands crosses each other.

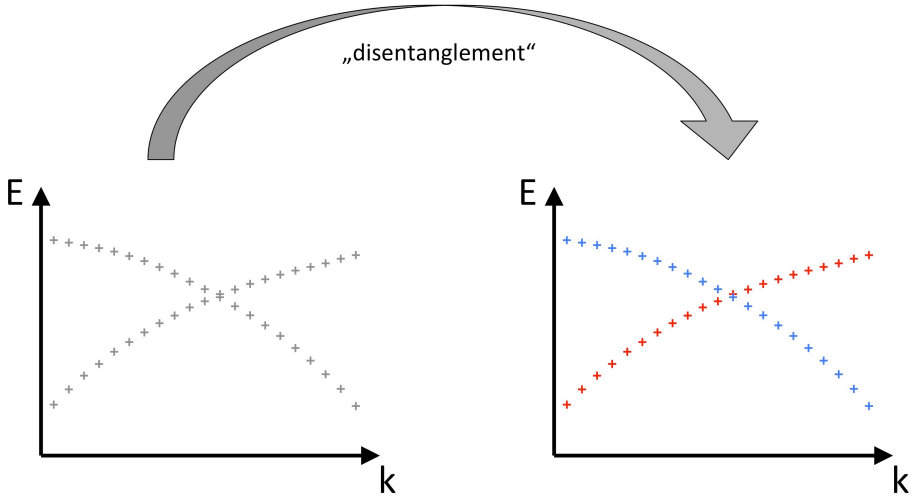

Figure 2.1.: Schematic depiction of the disentanglement process used for assigning band indices to KS eigenvalues.

Wannier90 uses a so called "disentanglement procedure" (see [8] for reference). Since the computer has no intrinsic notion of bands (only a set of eigenenergies for each $\vec{k}$ point), the purpose of the disentanglement procedure is to correctly "connect" the energies at each of the $\vec{k}$ point to form the bandstructure, see Fig. 2.1.

2.2.1. Spread functional Ω

The idea is to use the gauge degree of freedom to find a set of Wannier functions which are, according to some predefined criterion, maximally localized in real space. In order to find this particular $U_{mn}(\vec{k})$ we must first define our spread functional Ω.

$$\Omega := \sum_n \left[\langle r^2 \rangle_n - \langle \vec{r} \rangle_n^2 \right] \tag{2.42}$$

with:

$$\langle r^2 \rangle_n = \langle \vec{0}, n | \, \hat{\vec{r}}^2 \, | \vec{0}, n \rangle \tag{2.43}$$

$$\langle \vec{r} \rangle_n = \langle \vec{0}, n | \, \hat{\vec{r}} \, | \vec{0}, n \rangle \tag{2.44}$$

This particular spread functional can be decomposed in two terms Ω_i and Ω_g, with the first one being independent of $U_{mn}(\vec{k})$ (and thus carrying the subscript i for "independent of the chosen gauge") while the latter is gauge dependent (subscript "g").

$$\Omega = \underbrace{\sum_n \left[\langle r^2 \rangle_n - \sum_{\vec{R},m} | \langle \vec{R}, m | \, \hat{\vec{r}} \, | \vec{0}, n \rangle |^2 \right]}_{\Omega_i} + \underbrace{\sum_n \sum_{\vec{R}, m \neq \vec{0}, n} | \langle \vec{R}, m | \, \hat{\vec{r}} \, | \vec{0}, n \rangle |^2}_{\Omega_g} \tag{2.45}$$

Defining a projector onto the bands considered at a given $\vec{k}$ (2.9) allows for a quite intuitive picture of the "wannierization procedure".

$$\hat{P} := \sum_{\vec{k},n} |u_{n,\vec{k}}\rangle \langle u_{n,\vec{k}}| = \sum_{\vec{R},n} |\vec{R}, n\rangle \langle \vec{R}, n| \tag{2.46}$$

The Wannier functions obtained by minimizing Ω are found to be identical with the eigenfunctions of the "projected position operator" $\hat{P}\hat{x}\hat{P}$ in the one dimensional case. With an orthonormal Wannier eigenbasis and associated eigenvalues $x_0 m$, it follows that $\langle \vec{R}, m | \, \hat{P}\hat{x}\hat{P} \, | \vec{0}, n \rangle = x_0 m \delta_{R,0} \delta_{m,n}$. This means that Ω_g will exactly vanish, thus minimizing Ω to Ω_i. In three dimensions the situation is somewhat more complicated since the cartesian components of the projected space operator ($\hat{P}\hat{x}\hat{P}$, $\hat{P}\hat{y}\hat{P}$, $\hat{P}\hat{z}\hat{P}$) do not commute and one has to search for the optimal compromise to "maximally diagonalize" all three of them simultaneously. With that in mind we can write Ω_g as a sum of band-diagonal $\Omega_g^{(D)}$ and band-offdiagonal contributions $\Omega_g^{(OD)}$.

$$\Omega_g = \underbrace{\sum_n \sum_{\vec{R}\neq\vec{0}} |\langle \vec{R}, n|\, \hat{\vec{r}}\, |\vec{0}, n\rangle|^2}_{\Omega_g^{(D)}} + \underbrace{\sum_{m\neq n} \sum_{\vec{R}} |\langle \vec{R}, m|\, \hat{\vec{r}}\, |\vec{0}, n\rangle|^2}_{\Omega_g^{(OD)}} \tag{2.47}$$

It is quite straigthforward to see that matrix elements of powers of the position operator $\hat{\vec{r}}$ in a "Wannier basis" can be written as:

$$\langle \vec{R}, n|\, \hat{\vec{r}}\, |\vec{0}, m\rangle = i\frac{V}{(2\pi)^3} \int e^{-i\vec{k}\cdot\vec{R}} \langle u_{n,\vec{k}}|\, \nabla_k\, |u_{m,\vec{k}}\rangle\, d\vec{k} \tag{2.48}$$

$$\langle \vec{R}, n|\, \hat{\vec{r}}^2\, |\vec{0}, m\rangle = \frac{-V}{(2\pi)^3} \int e^{-i\vec{k}\cdot\vec{R}} \langle u_{n,\vec{k}}|\, \nabla_k^2\, |u_{m,\vec{k}}\rangle\, d\vec{k} \tag{2.49}$$

In a discrete $\vec{k}$-space, using the simplest finite difference expressions for the nabla operators and approximating the integral via a sum, the expressions above allow us to extract $\langle r\rangle_n$ and $\langle r^2\rangle_n$ as

$$\langle \vec{r}\rangle_n = \frac{i}{N} \sum_{\vec{k},\vec{b}} w_b \vec{b} \big[\, \langle u_{n,\vec{k}}|u_{n,\vec{k}+\vec{b}}\rangle - 1\big] \tag{2.50}$$

$$\langle r^2\rangle_n = \frac{1}{N} \sum_{\vec{k},\vec{b}} w_b \big[2 - 2\,\langle u_{n,\vec{k}}|u_{n,\vec{k}+\vec{b}}\rangle\,\big] \tag{2.51}$$

with $\vec{b}$ connecting k points to their nearest neighbour, N the number of cells and w_b the weights for each $\vec{b}$. We will now enforce a somewhat reasonable property to these expressions. It is evidently desirable that the choice of "home cell" (which cell we label $|\vec{0}, n\rangle$) shall not change the spread functional Ω. This means that a shift of a lattice vector $|u_{n,\vec{k}}\rangle \to |u_{n,\vec{k}}\rangle\, e^{-i\vec{k}\cdot\vec{R}}$ should lead to:

$$\langle \vec{r}\rangle_n \to \langle \vec{r}\rangle_n + \vec{R} \tag{2.52}$$

$$\langle r^2\rangle_n \to \langle r^2\rangle_n + 2\,\langle \vec{r}\rangle_n\, \vec{R} + R^2 \tag{2.53}$$

These properties are not yet fulfilled by (2.13) and (2.14) but can be incorporated as follows. Expanding the braket $\langle u_{n,\vec{k}}|u_{n,\vec{k}+\vec{b}}\rangle = 1 + ia_1 b + \frac{a_2}{2}b^2 + \mathcal{O}(b^3)$ with a_1 and a_2 real coefficients, we use the following approximations:

$$\langle u_{n,\vec{k}}|u_{n,\vec{k}+\vec{b}}\rangle - 1 \;\approx\; ia_1 b + \mathcal{O}(b^2) \;\approx\; i\, Im\big[ln(\langle u_{n,\vec{k}}|u_{n,\vec{k}+\vec{b}}\rangle)\big] + \mathcal{O}(b^2) \tag{2.54}$$

$$2 - 2\,\langle u_{n,\vec{k}}|u_{n,\vec{k}+\vec{b}}\rangle \;\approx\; -a_2 b^2 + \mathcal{O}(b^3) \;\approx\; 1 - |\,\langle u_{n,\vec{k}}|u_{n,\vec{k}+\vec{b}}\rangle\,|^2 + a_1^2 b^2 + \mathcal{O}(b^3) \tag{2.55}$$

Using (2.54) and (2.55) we can rewrite $\langle r^2\rangle_n$ and $\langle \vec{r}\rangle_n$ in a form that fulfills the aforementioned properties (2.52, 2.53):

$$\langle \vec{r}\rangle_n = -\frac{1}{N}\sum_{\vec{k},\vec{b}} w_b\,\vec{b}\,Im\Big[ln\big(\,\langle u_{n,\vec{k}}|u_{n,\vec{k}+\vec{b}}\rangle\,\big)\Big] \tag{2.56}$$

$$\langle r^2\rangle_n = \frac{1}{N}\sum_{\vec{k},\vec{b}} w_b\left\{1 - |\,\langle u_{n,\vec{k}}|u_{n,\vec{k}+\vec{b}}\rangle\,|^2\Big(Im\big[ln(\langle u_{n,\vec{k}}|u_{n,\vec{k}+\vec{b}}\rangle)\big]\Big)^2\right\} \tag{2.57}$$

After some rearrangement this notation allows us to rewrite the spread functional Ω and again identify Ω_I, Ω_g^{OD} and Ω_g^D, mentioned before, as:

$$\Omega_I = \frac{1}{N}\sum_{\vec{k},\vec{b}} w_b\left\{\bar{N} - \sum_{m=1,n=1}^{\bar{N}} |\,\langle u_{m,\vec{k}}|u_{n,\vec{k}+\vec{b}}\rangle\,|^2\right\} = \frac{1}{N}\sum_{\vec{k},\vec{b}} w_b\,Tr\big[\hat{P}_{(\vec{k})}(1-\hat{P}_{(\vec{k}+\vec{b})})\big] \tag{2.58}$$

$$\Omega_g^{OD} = \frac{1}{N}\sum_{\vec{k},\vec{b}} w_b \sum_{m\neq n} |\,\langle u_{m,\vec{k}}|u_{n,\vec{k}+\vec{b}}\rangle\,|^2 \tag{2.59}$$

$$\Omega_g^D = \frac{1}{N}\sum_{\vec{k},\vec{b}} w_b \sum_n \Big(- Im\big[ln(\langle u_{m,\vec{k}}|u_{n,\vec{k}+\vec{b}}\rangle)\big] - \vec{b}\cdot\langle\vec{r}\rangle_n\Big)^2 \tag{2.60}$$

As can easily be seen now, all three terms are positive definite and as shown in (2.58) encoding the complicated expression as a trace over projection operators ($\hat{P}_{(\vec{k})} := \sum_n |u_{n,\vec{k}}\rangle\,\langle u_{n,\vec{k}}|$) emphasizes the gauge-independence of Ω_I. It is quite obvious that this gauge-independent part Ω_I can be evaluated at the beginning of the "wannerization" procedure and will not affect the minimization of the total spread functional.

2.2.2. Gradient of the spread functional $\frac{d\Omega}{dU}$

In order to minimize the spread functional we have to know the variaton of Ω with respect to an infinitesimally different gauge to (at least) first order. Varying our unitary "gauge matrix" U_{mn}, introduced in (2.41), infinitesimally far from unity, $U_{mn}(\vec{k}) = \delta_{mn} + dU_{mn}(\vec{k})$, corresponds to a change of the Bloch states $|u_{n,\vec{k}}\rangle \rightarrow |u_{n,\vec{k}}\rangle + \sum_m dU_{mn}(\vec{k})\,|u_{n,\vec{k}}\rangle$. Rebranding $\langle u_{n,\vec{k}}|u_{n,\vec{k}+\vec{b}}\rangle$ as $W_{mn}(\vec{k})$ and inspecting its change yields:

$$dW_{nn}(\vec{k}) = -\big[dU(\vec{k}) \cdot W(\vec{k})\big]_{nn} + \big[W(\vec{k}) \cdot dU(\vec{k}+\vec{b})\big]_{nn} \tag{2.61}$$

Using the unitarity of U we can express the change for the combination of Ω_I and Ω_g^{OD} as:

$$d\Omega_{I,g^{OD}} = \frac{4}{N} \sum_{\vec{k},\vec{b}} w_b Re\Big[Tr\big[dW(\vec{k}) \cdot R(\vec{k})\big]\Big] \tag{2.62}$$

with:

$$R_{mn}(\vec{k}) \coloneqq W_{mn}(\vec{k}) W^*_{nn}(\vec{k}) \tag{2.63}$$

The diagonal part is found to be:

$$d\Omega_{g^D} = -\frac{4}{N} \sum_{\vec{k},\vec{b}} w_b Im\Big[Tr\big[dW(\vec{k}) \cdot T(\vec{k})\big]\Big] \tag{2.64}$$

with:

$$T_{mn}(\vec{k}) \coloneqq \frac{W_{mn}(\vec{k})}{W^*_{nn}(\vec{k})} \Big\{ Im\big[ln(W_{nn}(\vec{k}))\big] + \vec{b} \cdot \langle \vec{r} \rangle_n \Big\} \tag{2.65}$$

Lastly introducing the "super operators" $\hat{\mathrm{S}}[\hat{o}]$ and $\hat{\mathrm{A}}[\hat{o}]$ we can write the desired gradient of the spread functional quite elegantly as:

$$\frac{d\Omega}{dU(\vec{k})} = 4 \sum_{\vec{b}} w_b \Big\{ \hat{\mathrm{S}}\big[\hat{R}(\vec{k})\big] - \hat{\mathrm{A}}\big[\hat{T}(\vec{k})\big] \Big\} \tag{2.66}$$

$$\hat{\mathrm{S}}[\hat{o}] \coloneqq \frac{(\hat{o} - \hat{o}^\dagger)}{2} \tag{2.67}$$

$$\hat{\mathrm{A}}[\hat{o}] \coloneqq \frac{(\hat{o} - \hat{o}^\dagger)}{2i} \tag{2.68}$$

We can now numerically minimize the spread functional with steepest descent methods using the gradient obtained in (2.66). Updating the unitary matrix U of our gauge freedom by a small portion of this gradient ensures that we always minimize our spread functional. For further details of the numerical implementation see [6,7,8] as mentioned at the beginning of this chapter.

2.3. Tight-Binding formalism

The purpose of "wannierizing" our DFT solution is to obtain a set of localized "atomic-like" orbitals which warrant approximating the defect via a tight-binding parametrization. Tight-binding calculations are standard methods of solid state physics [2] that allow to treat substantially larger systems than for example ab initio methods such as DFT.

The idea is to treat the difference between the real crystal-potential and a periodically repeated single atom potential as a minor correction, thus allowing us to expand the wavefunction of the solid $|\Psi\rangle$ into any kind of localized states $|\Phi_i\rangle$ (in our case maximally localized Wannier functions):

$$|\Psi\rangle := \sum_m \sum_n \alpha_{m,n} |\Phi_{m,n}\rangle \tag{2.69}$$

While n runs over atomic sites and is confined to the number of atoms used to build our system, the number of atomic orbitals considered at each site (indexed by m) can be restricted to the most relevant bands (for example p_z orbitals in graphene) for numerical feasibility. Condensing both sums (m and n) into a single one over index j which subsumes both lattice and band indexes and neglecting potential overlap between atomic orbitals, $\langle\Phi_n|\Phi_m\rangle = \delta_{nm}$, (2.69) can be interpreted as an expansion over an orthonormal basis. Inserting this expansion into an effective one-particle Schrödinger equation yields a matrix equation which is a simple eigenvalue problem for the expansion coefficients α_j.

$$\sum_j \alpha_j \underbrace{\langle\Phi_i|\hat{H}|\Phi_j\rangle}_{H_{ij}} = E \sum_j \alpha_j \underbrace{\langle\Phi_i|\Phi_j\rangle}_{\delta_{ij}} \tag{2.70}$$

$$\sum_j H_{ij} \cdot \alpha_j = E \cdot \alpha_i \tag{2.71}$$

H_{ij} is usually multi-diagonal, depending on how many next neighbour interactions we choose to incorporate into the calculation. The diagonal parts are reffered to as onsite-energies while the off-diagonal terms are the so called hopping terms. It comes as no surprise that increasing the number of hopping terms increases accuracy and likewise computational effort.

2.4. Graphene

Graphene, a two dimensional material, consists of a single layer of carbon atoms. Its hexagonal honeycomb-lattice can be described via two trigonal sublattices A and B by using a Wigner-Seitz cell (green) that includes two basis carbon atoms, as shown in Fig. 2.2.

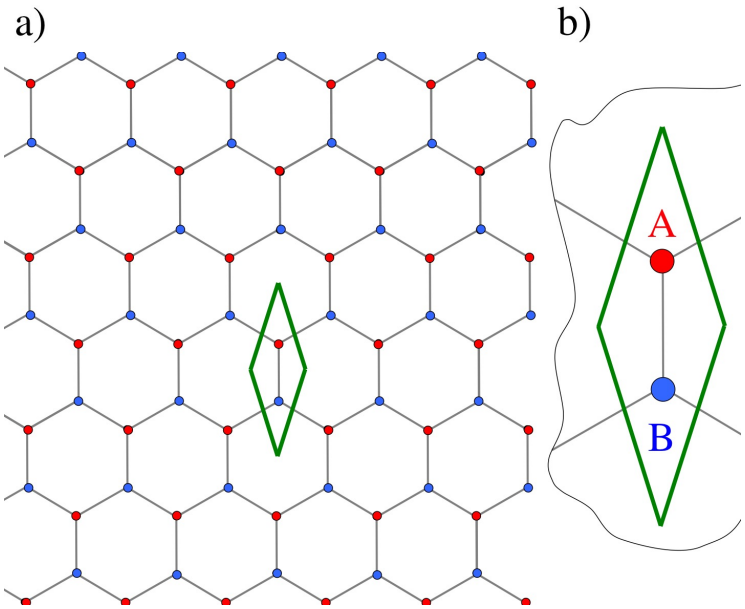

Figure 2.2.: **a)** Schematic depiction of the honeycomb structure of graphene and **b)** its irreducible unit cell with two-atomic base (sublattices A and B).

Due to its various unique characteristics, graphene is a promising candidate for future use in capacitors, quantum dot arrays for quantum computation, batteries and many more electronical applications. The extraction of this material has started with A. Geim and K. Novoselov through exfoliation from highly oriented pyrolytic graphite via pressing an adhesive-coated piece of glass onto a plasma etched graphite surface and removing it together with a thin layer of graphene. Nowadays synthesis methods such as chemical vapor deposition, epitaxial growth or chemical reduction from graphiteoxide are also in use.

2.4.1. Bandstructure

One especially interesting property of graphene is its linear dispersion relation caused by its hexagonal symmetry and diatomic base. The bandstructure of graphene exhibits two "disjunct" linear dispersion cones, the so called "Dirac cones". This name comes from the resemblance to the bandstructure derived from the Dirac equation for massless, free, ultrarelativistic particles (for small $\vec{k}$-values). These, in total, six cones only two of which are non-equivalent with respect to symmetry operations, schematically presented in Fig. 2.3, warp trigonally for increasing $|\vec{k}|$, before connecting in an arch-like structure.

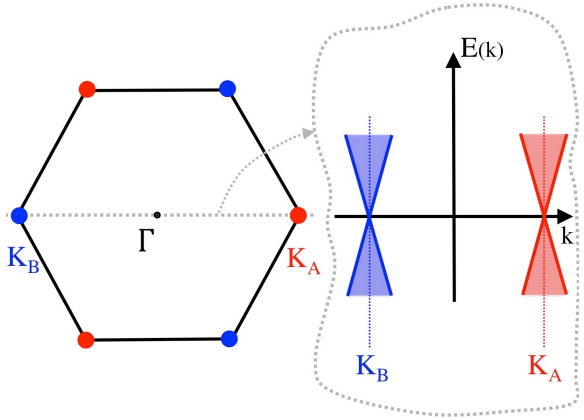

Figure 2.3.: Schematic picture of graphenes Brillouin zone with the Dirac cones of sublattices A and B

We can derive the initially linear dispersion relation via the Dirac equation by eliminating one spinor component:

$$v_F \begin{bmatrix} 0 & \hat{p}_x - i\hat{p}_y \\ \hat{p}_x + i\hat{p}_y & 0 \end{bmatrix} \begin{pmatrix} u \\ v \end{pmatrix} = E \begin{pmatrix} u \\ v \end{pmatrix} \tag{2.72}$$

$$E^2 = v_F^2 \cdot \underbrace{\left(\hat{p}_x^2 + \hat{p}_y^2\right)}_{\hbar^2\vec{k}^2} \quad \rightarrow \quad E = \pm v_F \hbar |\vec{k}| \tag{2.73}$$

The orbitals of the carbon atoms in graphene hybridize to three sp^2 (in the lattice plain) and one p_z orbital (orthogonal to the lattice plain) which takes part in transport processes.

2.5. Edgeless Quantum Dots

Quantum dots — nanoscale systems that hold a tunable, integer number of electrons — promise vast technological applications and are thus being increasingly researched in recent years. Often referred to as "artificial atoms", these systems feature sharp energy levels and are dominated by charging effects and quantum confinement. The most prominent, possible future use of quantum dots (QDOT), is as qubits used to perform quantum computation with the spin of the confined electron acting as the fundamental two-level system for information processing. In another popular research area, spintronic, QDOTs are manipulated to act as spin filters [50] or spin-blockades [49]. The most advanced QDOTs are based on heterostructures of GaAS and AlGaAs [51] while we will henceforth focus on graphene as a host material.

Electrostatically confining massless Dirac fermions —present in graphene — is usually quite challenging due to Klein tunneling [52]. In the case of graphene one usually has to etch desired structures (e.g. via e-beam lithography) or employ electric displacement fields which can be used to open band gaps in bilayer graphene. While the success of the first method is heavily influenced by edge roughness and the chemical nature of these edges (which mostly results in unintended charge localization or undesirable scattering processes) the latter is restricted by how well the localization can be tweaked. Additionally, the idea of spin qubits in graphene requires controlled lifting of the valley degeneracy.

An alternative way (proposed in [16,17,18]) is to use a combination of a homogeneous magnetic and an electric confinement field.

$$E_n = sgn(n)\sqrt{2\hbar e v_F^2 |B||n|} \qquad n \in \mathbb{Z} \tag{2.74}$$

While the magnetic field ensures Landau quantization (with the energy levels given above, see *Appendix A* for a concise derivation of relativistic Landau levels present in graphene), the electric field (typically induced via an STM tip) is used to induce confinement in the gaps between the bulk Landau levels thus completely circumventing any edge roughness altogether. The STM tip locally shifts the energy levels relative to the Landau levels (LL), see Fig. 2.4.

The detailed geometry of the tip determines its electrostatic potential and thus the form and energy of the induced quantum dot (QDOT) orbitals. We derive the specific shape of the confinement potential $V_{\text{tip}}(\vec{r})$ by solving a classical Poisson equation which is described in more detail in the supporting information of [1].

The energy splitting of the QDOT states is usually about one order of magnitude smaller than the first and largest Landau level gap ($\Delta E \approx 100$meV for $B \approx 7$T). Orbital splittings Δ_j^O (approx. $5 - 10$meV) separate these QDOT states. Taking both real spin and pseudo spin (sublattice degree of freedom) into account, each orbital will be fourfold degenerate in graphene. While any form of substrate interaction could in principle lead to finite valley splitting Δ_j^k, the homogeneous magnetic field creating the Landau quantization leads to a spin splitting Δ^σ (Zeeman) in the order of 800μeV.

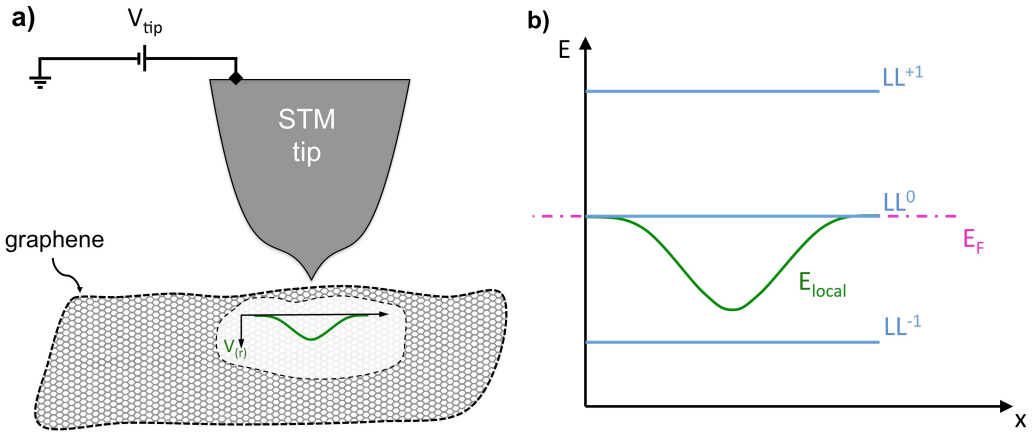

Figure 2.4.: **a)** schematic setup of STM tip and graphene flake, **b)** creation of the confinement within the first Landau gap

From an experimental viewpoint this setup is quite elegant as the STM tip cannot only be used to create the QDOT but also to measure its level spectrum to be measured.

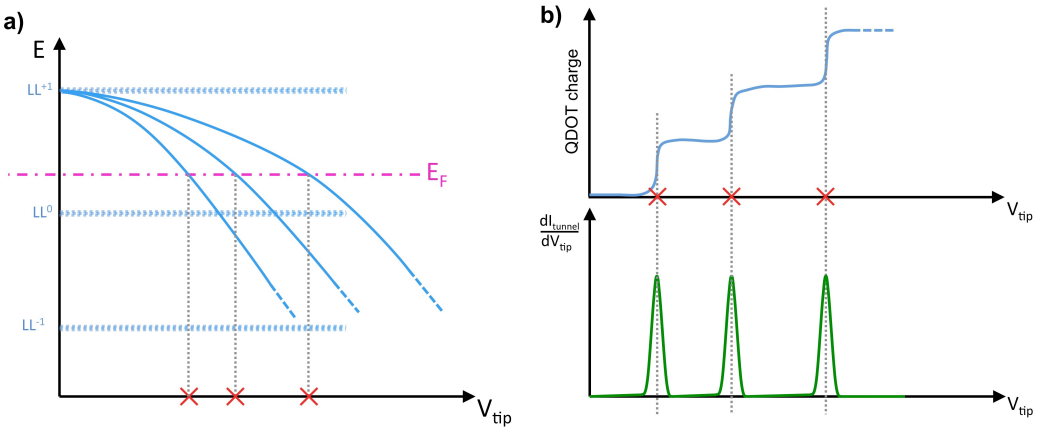

Figure 2.5.: Diagrammatical explanation of probing energy levels via a charging sequence. **a)** Energy vs tip-potential with the "emerging" QDOT states (three solid blue lines) and the three Landau levels closest to the Fermi energy (dashed partially transparent blue lines). **b)** Electrical charge within the QDOT vs tip potential and the differential tunnel current with peaks at the point where a QDOT level crosses E_F in a).

Let us briefly outline the process. Some of the, in theory perfectly degenerate, LL^n states (the ones which are spatially close to the STM tip, Fig. 2.5 only focuses on the LL^{+1} states) begin to lower their energy once the tip voltage, V_{tip}, is slowly switched on. Increasing V_{tip} shifts these emerging QDOT states energetically downwards. Whenever one such level then crosses the Fermi energy of our graphene flake the QDOT is charged (or discharged if V_{tip} is reduced) as an additional electron tunnels from the tip into the QDOT.

For this to happen any additional electron must overcome both the single particle energy spacings and the electrostatic repulsion of all the other electrons already present within the QDOT. This sudden increase of the Hartree energy for all states shifts additional local density of states from quasi-continuous bulk LLs into the energy window of $\mu_{\text{graphene}} - \mu_{\text{tip}}$, which in turn increases the tunneling current I. The addition energy spectrum of the QDOT can thus be deduced (including charging effects such as the Coulomb blockade) by investigating peaks in the differential tunneling current dI/dV_{tip}, see Fig. 2.5.

2.5.1. Why graphene?

Despite the various challenges encountered when investigating graphene quantum dots there is vast potential which upholds research interest in the recent past. As mentioned earlier, an arry of QDOTs combined with tunable coherent coupling equals a universal quantum computer. Graphene offers improvements for both of the main properties of an ideal qubit: *easy manipulation* and *weak coupling to the environment*. Most single spin qubit operations involve manipulating via electron spin resonance (ESR). The Rabi frequency of this process is given by $f_{\text{Rabi}} = \frac{g\mu_B B}{2h}$ and thus proportional to the electron spin g-facto, which is material specific. Compared to GaAs, graphene offers a five times larger g-factor, promising faster manipulation which is crucial for fault-tolerant quantum computing.

Since carbon is a light element ($Z = 6$) we expect weak spin-orbit interaction. While this argumentation alone is not sufficient in solids — where inversion asymmetry plays a critical role — the hopefully small ripples in graphene will most likely not suffice to introduce significant spin-orbit coupling. Carbon also comes in only two stable isotopes (^{12}C dominating resources up to 99% and ^{13}C). The hyperfine interaction with nuclear spins will also be negligible since only ^{13}C features non zero nuclear spin ($\frac{1}{2}$). Important quantities describing the stability of our qubit are the spin relaxation time (spin-orbit coupling weak but finite) and the spin decoherence time (real spin qubit), both of which will likely be larger in graphene. We can thus reasonably propose that graphene is in theory an excellent host material for future QDOT applications.

2.6. Lattice Defects of graphene

As most realistic materials are not pristine and will inevitably have some imperfections with respect to their lattice structure, this section is intended to briefly familiarize with the most common lattice defects of single layer graphene, as these are in our case intended and a major part of this thesis. Recent development has led to great improvements in sample processing which allows for graphene flakes with very low defect concentration. The overall idea of this project is to use lattice defects in graphene to actively induce valley splitting Δ_j^k in an edge-free QDOT located in their vicinity. Focusing only on at least metastable, static defects we can categorize them in two classes:

I) Imperfections which keep the number of carbon atoms unchanged and only shift them in position.

Two defects of this category, whose interplay with a nearby QDOT will be investigated in this thesis, are the so called flower defect (24 carbon atoms rotated 60 degrees, see Fig. 2.6a) and the Stone Wales defect (2 carbon atoms rotated 90 degrees, see Fig. 2.6b).

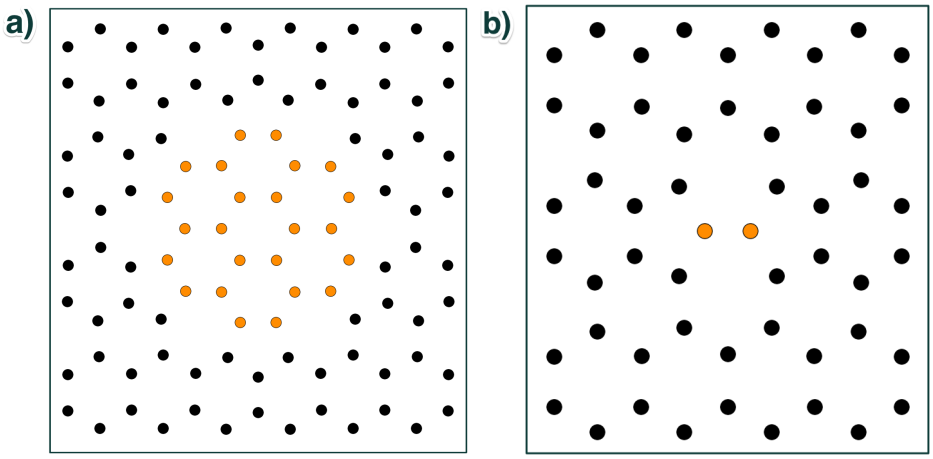

Figure 2.6.: Sketches of lattice defects in graphene (type I) with the relevant displaced carbon atoms colored in orange. **a)** flower defect **b)** Stone Wales defect.

II) Imperfections that locally remove, substitute or add any sort of atom to the system.

The most prominent defects in this category include double- (two neighbouring C atoms missing) and single- (single C atom missing) vacancy defects, see Fig. 2.7. One possible substitution defect is to replace one C atom with a Si atom, in short the "Si substitution" (Fig. 2.7b).

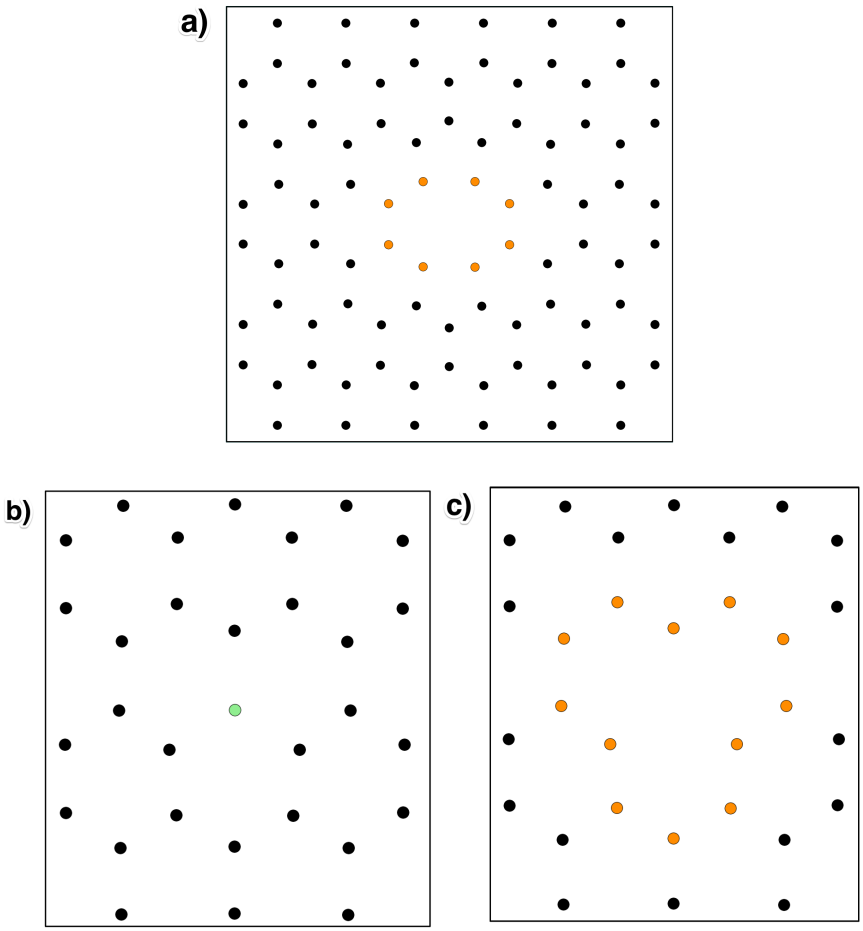

Figure 2.7.: Sketches of lattice defects in graphene (type II) with the carbon atoms in the vicinity of vacancies colored in orange and substituted atoms colored green. **a)** double vacancy defect **b)** silicium substitution defect **c)** single vacancy defect.

2.7. Embedding Scheme

In order to calculate properties of our QDOT as a function of position (relative to the defect center) we are inevitably forced to treat the total system within a tight binding description. The sheer size of the QDOT (approx. 30-40nm in diameter) simply excludes anything more intricate (DFT, etc.). Implementing defects within a pristine "tight binding graphene flake" (approx. 120nm × 100nm in size) can be done in several ways, two of which we shall examine more closely.

The poor man's approach to tight binding defects is to stay entirely on the tight binding level of theory and simply locally adjust on-site and hopping terms based on an educated guess. Since any such guessing is destined to be incorrect we think that this approach is only valid for vacancies (in our case

double- and single vacancy). Vacancies are in zeroth order approximated by setting the on-site energy of the respective "vacant" sites absurdly high (for example 100.000eV) thereby reducing any hopping to or from those sites to zero. This "simple" embedding scheme is useful as a reference model for more involved defect treatments.

A next step in accuracy is to model the defect in DFT. Since we utilize the VASP package [39-42] (which uses a plain wave basis set) we are restricted to periodic unit cells. We remove two atoms from such a pristine DFT cell (6 $\times$ 6 graphene irreducible unit cells $\equiv$ "DFT cell") before starting geometry optimization. Since starting from high-symmetry configuration often causes the geometry optimization algorithm to get stuck in local energy minima we slightly shift the initial positions of the atoms close to the defect to break any metastable configurations and allow for faster convergence. Geometry relaxation of the atomic positions (edges of the DFT cell fixed) is performed before the system is accurately converged electronically. Such a DFT cell is pictured in Fig. 2.5.

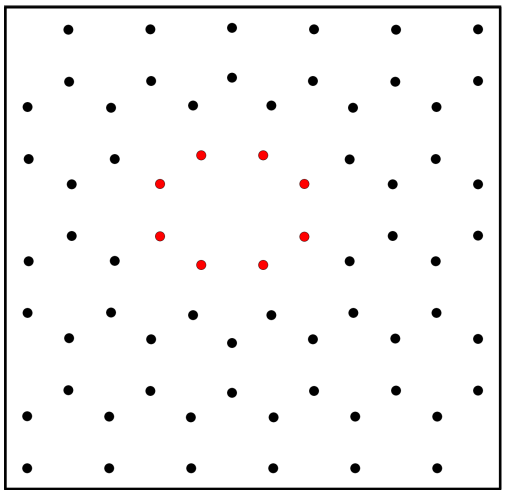

Figure 2.8.: Periodic DFT cell used for the double defect with atoms close to the defect color coded in red.

We then use wannier90 [6,7,8] to extract maximally localized Wannier functions in real space and conveniently calculate tight-binding parameters at the same time. The final embedding step is to replace the respective entries of a pristine graphene Hamiltonian with the on-site and hopping parameters achieved via Wannierization (granted the pristine flake features the same number of NN as the defect, in our case ten neighbours). All the defects used in this thesis (except for the single vacancy defect) have been provided in "wannierized form" by Lukas Linhart.

If a ten NN description of the total system is not feasible (e.g. electronic transport through large scale structures) one can make use of the curtain approach of L. Linhart et. al. [9] which tries to smoothly transition from a ten NN defect region to a three NN pristine environment by surrounding the defect with various "curtains" that sequentially utilize less NN.

2.7.1. Re-enforcing symmetries

Embedding a defect in the previously defined manner — by simply replacing elements in the Hamiltonian — is quite obviously a simplified approximation. It is, however, still possible to improve the description by making clever use of symmetries. In almost all cases a defect does not break all symmetries of the pristine lattice but leaves a few of them intact. It turns out our DFT-Wannier-TB process has room for improvement regarding those. The restriction to periodic super cells on the DFT level means that almost all defects suffer (to some degree) symmetry breaking. For example, the double vacancy defect is in principle perfectly mirror symmetric regarding its vertical and horizontal axes. The DFT cell however is not (due to its required periodicity). This results in tight binding parameters that do not satisfy the symmetries of the original defect. While the degree of symmetry breaking varies for the specific defect under consideration we encountered imbalances of onsite parameter values of about $1-5$meV as well as symmetry related 1^{st} and 2^{nd} NN hopping terms that, on average, differ by $10-30$meV. While this magnitude is probably not enough to raise real concerns about the super cell description used, we still came up with a very fast and simple way to improve the description, even if only by a small margin.

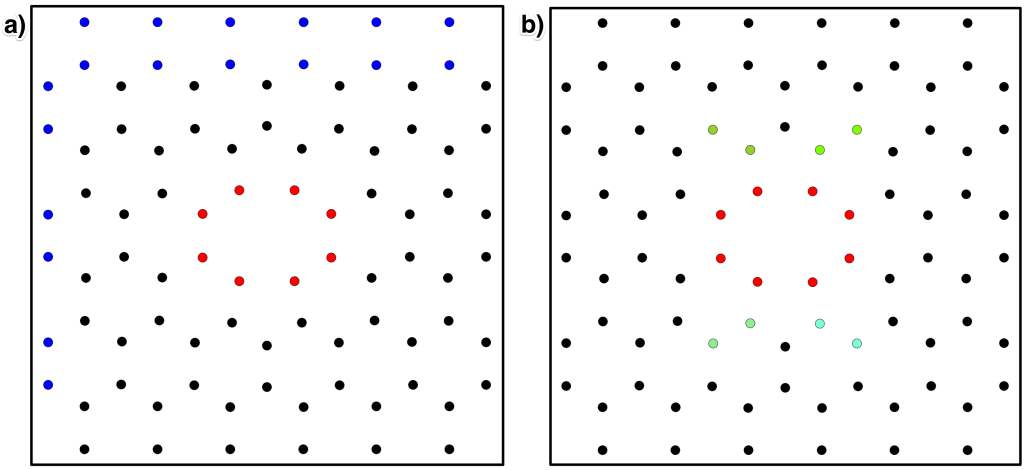

Figure 2.9.: **a)** Symmetry expanded, "wannierized" super cell with added atoms colored blue and defect vicinity in red as guide to the eye. **b)** Four pairs of symmetry equivalent atoms (different shades of green) used for the averaging in the symmetrization process.

We go on to reimpose the original symmetries to our "wannierized" defect. To do that we first add additional atoms (depictured in blue color in Fig. 2.9a) whose interactions we copy from already existing atom pairs of the same symmetry. The second part of the symmetrization sees all other atom pairs of the same symmetry (example of four such pairs pictured in Fig. 2.9b) assigned an average value of their respective interactions. We thus reestablish the inherent symmetries of our defect and also increase the average spatial distance between defect center and bulk description which is quite impressive, given the simplicity of the procedure.

3. Results

After recapitulating the DFT-wannierization process for the single vacancy defect, we calculate the change in level spacing of the six lowest QDOT states as a function of the distance to the defect center for various defects. Investigating transition dynamics of our system via a state-of-the-art Magnus time propagation algorithm allows for a comparison with analytic predictions of Landau Zener theory. Lastly we try to combine defects in certain configurations to precisely tailor the size of avoided crossings in the level spacing landscape.

3.1. Parametrization of the single vacancy defect (DFT)

One of the main ambitions of this thesis is to add the single vacancy defect to our "portfolio" of wannierized defects. A single vacancy is one of the most common defects in any crystal structure. In graphene, the "removal" of a C atom causes the system to undergo bond reconstruction [36, 37] (in the form of a Jahn-Teller distortion). Two of the three atoms neighbouring the vacancy form a complete $\sigma - \pi$ bond, whereas the remaining atom is left with both a dangling σ and a dangling π bond. There remains some discord about whether or not the structure stays flat or if the latter of the three atoms is moved out of plane. Both results have been acquired theoretically and seem very close in total energy.

Since this defect is experimentally known to carry a magnetic moment [33, 35, 37] we will have to perform a spin polarized DFT calculation. We choose a 6×6 DFT supercell with one C atom removed (Fig. 3.1). This is a reasonable compromise between numerical feasibility while trying to keep spurious defect-defect interaction, introduced by the periodic boundary conditions, minimal. Using a 6×6 SC, that is one of the $(3n \times 3n)$ symmetric family, causes the K and K' points to fold back onto the Γ point of the SC Brillouin zone. This is beneficial by allowing us to pre-converge with a "Γ-only" VASP calculation and use the acquired density as a starting point for a subsequent calculation sampling the Brillouin zone with a 3×3×1 Monkhorst k-grid, thereby hopefully saving some computation time.

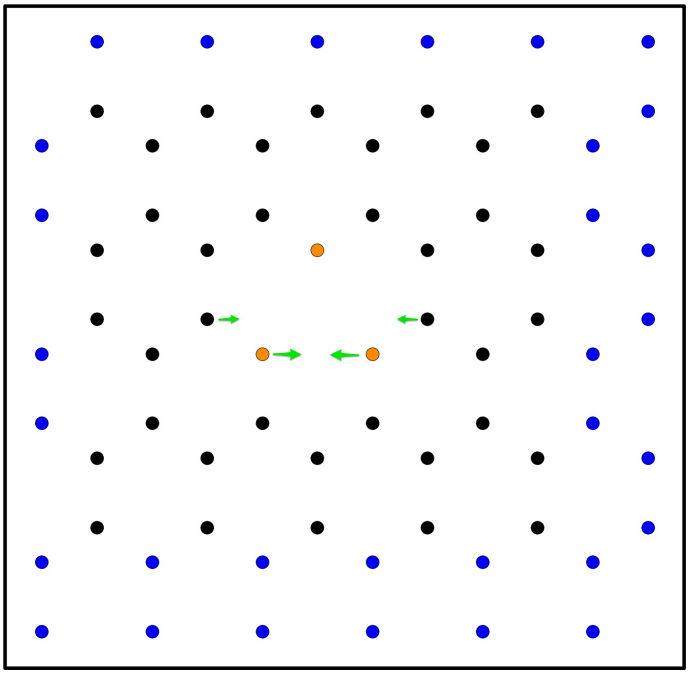

Figure 3.1.: DFT super cell used for the single vacancy. Atoms next to the vacancy colored orange and atoms kept fixed during the geoemtry optimization depicted in blue. Green arrows indicate initial displacement to break trigonal symmetry.

Insights of an impressively thorough investigation of the magnetic moment of such a single vacancy [11] suggest that standard DFT, using local approximations of exchange-correlation functionals, is not well suited to describe the transition of delocalized π-states (pristine graphene) to localized defect states (C atom removed) due to its erroneous self-interaction. We therefore choose a hybrid functional composed of the PBE functional (Perdew-Burke-Ernzerhof) and a fraction of Hartree-Fock exchange ($\alpha = 0.25$). As can be expected this method drastically increases overall computation times.

We first perform geometry optimization via the Hellman-Feynman theorem with the edge atoms of our SC fixed. As mentioned before we do so in two steps with an initial calculation involving only the Γ point before continuing with a 3×3×1 Monkhorst k-grid. We slightly break all relevant symmetries (move some atoms out of plane, break trifold angular symmetry) in the defect region to avoid getting stuck in a metastable configuration. Breaking the trifold symmetry distinctly and limiting the position change in between each electronic convergence cycle (POTIM parameter in VASP) proved the safest way to end at the supposedly "correct reconstruction" with a magnetic moment of 2 μ_B. Future steps include the wannierization of the single vacancy and introducing a tight binding formalism that includes physical spin to investigate the magnetic properties of this defect in various setups (e.g. quantum transport, etc.).

3.2. Level-spacing landscapes / QDOT states

Having not yet successfully "wannierized" the single vacancy in the process outlined in the previous section we still have a multitude of graphene lattice defects usable on the tight-binding level of theory. As concisely outlined in chapter 2.5 we will now calculate the lowest eigenstates as of our edgeless QDOT (as well as their level spacings) in various set ups (defect type, distance to defect, direction of approach).

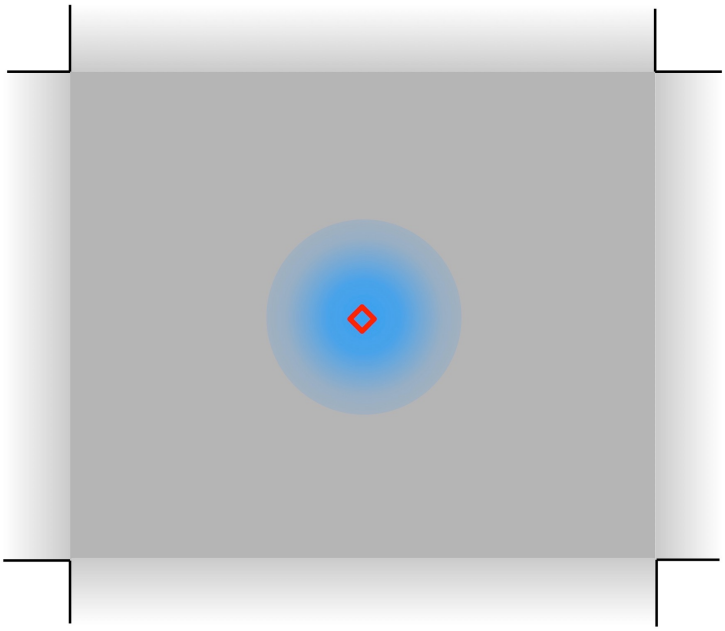

Figure 3.2.: Schematic depiction of the system under consideration. Graphene flake as a grey rectangle with open boundary conditions on all four sides indicated via black lines and fading grey colour. Center of the structure marked by red rhombus with the approximate size of the STM tip potential as semi-transparent blue circle.

Our system for this calculation consists of a graphene flake (that will initially be pristine, approx. 120nm $\times$ 100nm) with open boundary conditions on all four sides (Fig. 3.2). The center of the tip potential coincides with the center of our rectangular flake.We include a homogeneous magnetic field (7 Tesla) perpendicular to the flake via a Peier's phase. Due to our wannierized defects (10^{th} NN wannierized) which will eventually be embedded into the center, the entire flake uses a 10^{th} next-neighbour tight-binding description.

We choose to do so since initial testing revealed the eigenstates to be quite sensitive to any form of boxing or "curtaining" [9] which would allow us to use a 3^{rd}-NN description for the bulk. In order to determine the level spacing of our QDOT in a way akin to an experimental realization we calculate the eigenvalue spectrum of our system for varying magnitude of our STM tip potential V_{tip}.

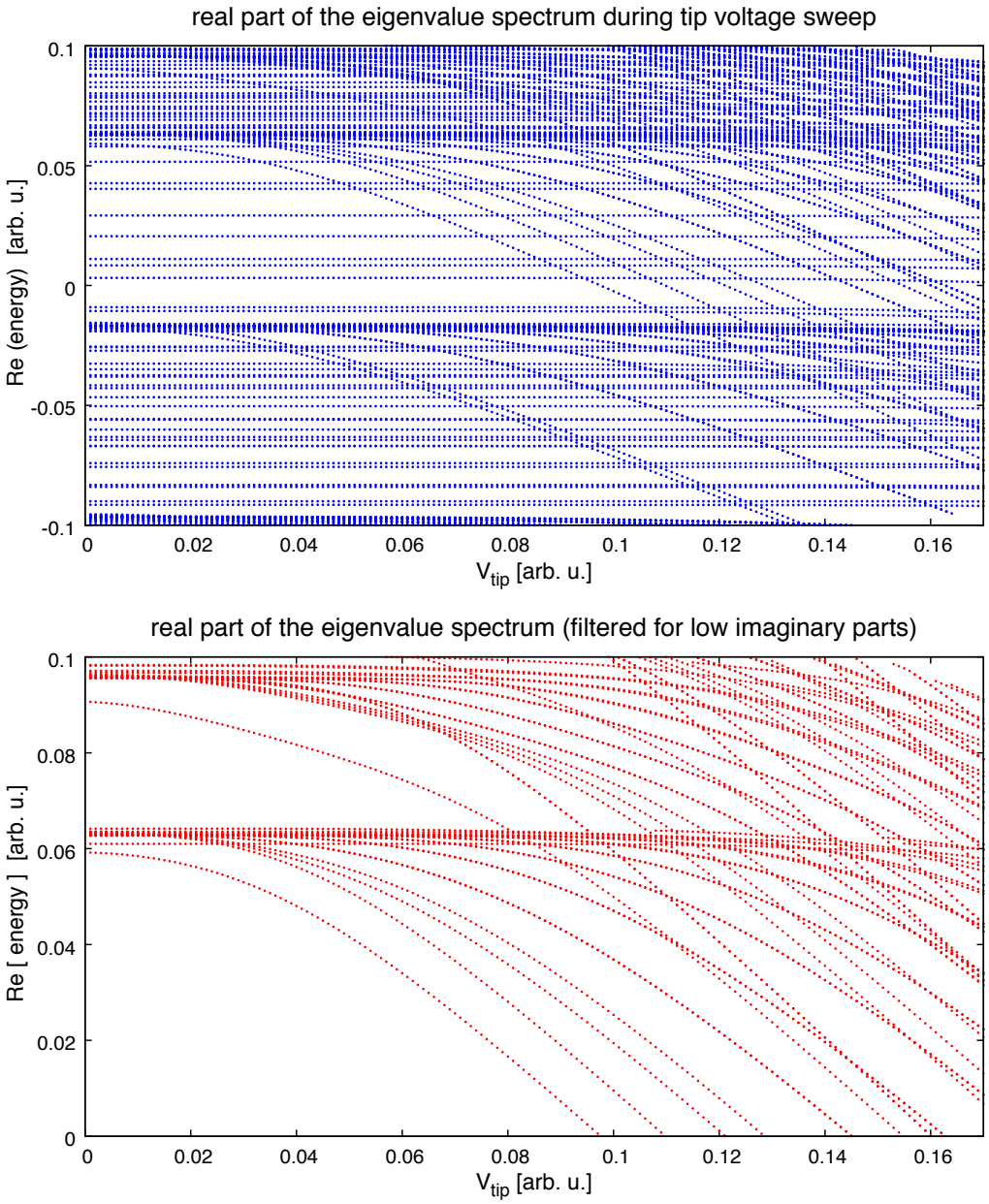

Figure 3.3.: **top)** real part of the eigenvalue spectrum for varying magnitudes of V_{tip}. **bottom)** same as top) but now only displaying positive real part values whose corresponding imaginary part is below a predefined threshold.

Fig. 3.3 shows a section of the real parts of the eigenvalue spectrum for varying magnitude of the tip potential (charging sequence in the experiment). We can clearly determine the Landau levels as the darker sections formed by massive aggregation of almost perfectly degenerate states (note a shifted Dirac point in our tight binding parameters, LL^0 not at zero energy).

These Landau level energies are the "starting point" for lines of eigenvalues decreasing with increasing V_{tip}. As outlined in chapter 2.5 these are the LL-states localized near the center of the STM potential well that start to confine and change into the "QDOT states". Introducing the Fermi energy of our system at zero ($E_{Fermi} \coloneqq 0$) means that extracting the roots of these lines (more precisely the points at which they cut the Fermi energy) will be enough to determine their orbital splitting Δ_j^O and valley splitting Δ_j^k. At some point all of these lines will have the same slope and the seemingly random choice for E_{Fermi} will only introduce an arbitrary shift of our values but leave the relative spacing unchanged. The open boundaries mentioned in the previous paragraph will now merely act as a tool to elegantly separate the sloping lines (confined states $\rightarrow$ low imaginary part of the eigenenergy) from the "noise" in the background (delocalized bulk-states $\rightarrow$ high imaginary part of the eigenenergy), see Fig. 3.3b. We will restrict ourselves to investigating the lowest six QDOT states — that is the first two orbital splittings Δ_j^O and the first three valley splittings Δ_j^k — as they stem from the first LL and seem to remain "isolated" from the diving lines originating from the second LL. Past this point interpreting the densely spaced sequence of QDOT states can become quite challenging.

Since the valley splitting Δ_j^k for the pristine system essentially vanishes we ensure clean numerical separation by adding an on-site energy of 1meV with different sign for each sublattice (A,B) to the entire flake which allows us to separation the almost degenerate pairs in a reproducible manner.

Embedding a defect into the center of our graphene flake (red rhombus in Fig. 3.2) leaves our method unchanged and allows us to investigate the influence of said defect on both orbital- (Δ_j^O) and valley splitting (Δ_j^k) of our QDOT. We can now go a step further and choose to position our tip potential slightly offset from the defect center. This allows us to study the influence of defect-QDOT distance on said level splittings and will reveal any "directionality" of our defects, as we can displace our QDOT in different directions (we focus on zigzag and armchair direction due to simplicity).

One very straightforward test to somewhat estimate the quality of our embedding scheme is to plot the onsite energies for the section of our graphene flake where we embedded the respective defect (see Fig. 3.4). This reveals that the geometrically small defects (double vacancy, Si substitution) meet the bulk value of the onsite energy (approx. 0.28eV) quite well at the borders of their DFT super cell while the flower defect (even though using an 8×8 DFT super cell to accommodate the larger footprint) would need an even larger super cell to smoothly transition to the bulk level. Even though our

symmetrization procedure has already improved this, whether or to what extent this discrepancy warrants further investigation — in the form of re-calculating the DFT solution with a differently sized super cell — for this defect is hard to discern.

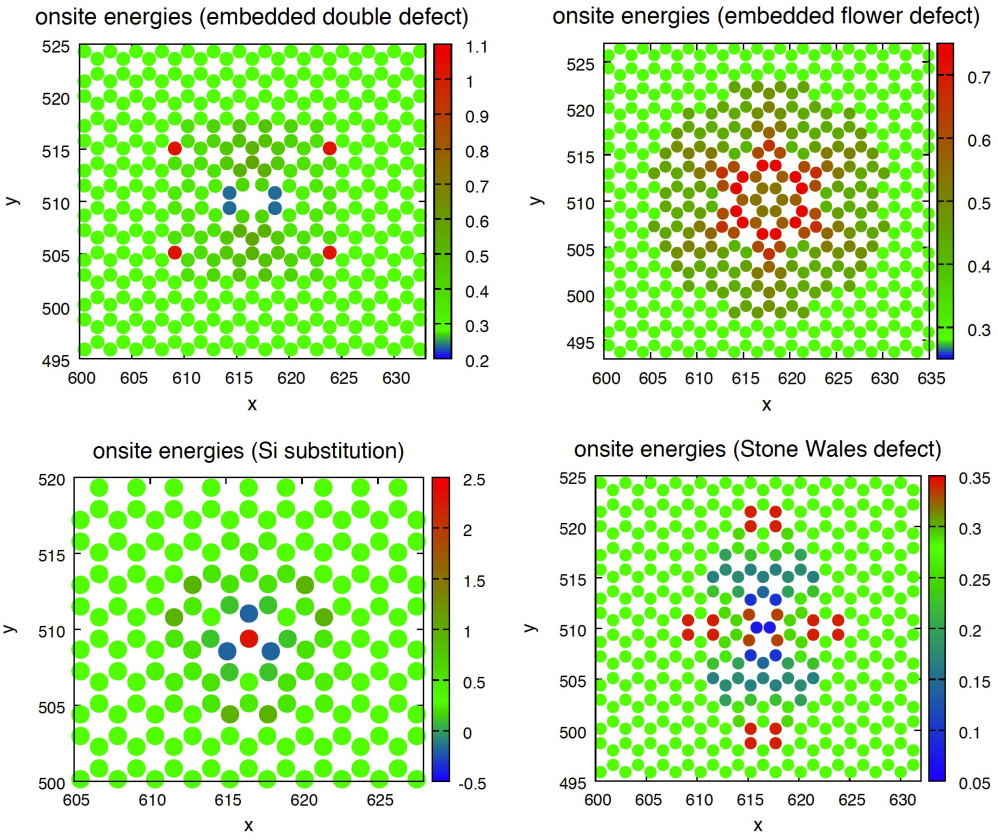

Figure 3.4.: Onsite energies of the graphene flake section where the corresponding defect has been embedded. Mind the different max/min values for the respective color scales (the bulk level of 0.28 has been kept green for all defects). **top left)** double vacancy defect, **top right)** flower defect, **bottom left)** Si substitution, **bottom right)** Stone Wales defect.

Further analysis in the form of plotting the hopping terms (from 1^{st}- to 10^{th}- NN) could provide more insight but is not attempted here (benefit-cost estimates point against recalculating the flower defect using a larger DFT supercell). The Stone Wales defect shows evidence of its trapezoidal super cell. It is however again quite hard to give an error estimate and decide whether or not a quadratic super cell (as used for all other defects) would have resulted in a less obtrusive embedding pattern for the onsite terms.

3.2.1. Pristine graphene

Applying the aforementioned procedure without embedding a defect yields the addition energy spectrum of the QDOT in pristine graphene. As shown in [1, 38] the eigenstates of bulk LL in pristine graphene are of the form:

$$|\Psi_N^K\rangle = |\Psi_{|N|-1}\rangle \otimes |\Downarrow\rangle + |\Psi_{|N|}\rangle \otimes |\Uparrow\rangle \tag{3.1}$$

$$|\Psi_N^{K'}\rangle = |\Psi_{|N|}\rangle \otimes |\Downarrow\rangle + |\Psi_{|N|-1}\rangle \otimes |\Uparrow\rangle \tag{3.2}$$

Where $|\Uparrow\rangle$ / $|\Downarrow\rangle$ represent the sublattices A / B respectively, while K/K' denote the two inequivalent valleys of graphene. We mention that for nonzero LL indices ($N \neq 0$) the indices on the respective sublattices differ by one while for $N = 0$ the part indexed with $|N| - 1$ simply vanishes. The electrostatic tip potential features radial symmetry and thus suggests a description via radial ($n_r \in \mathbb{N}_0$) and angular ($m \in \mathbb{Z}$) quantum numbers for the modified QDOT states. A possible adiabatic mapping from LL index N to allowed combinations of n_r and m is given in [1, 53].

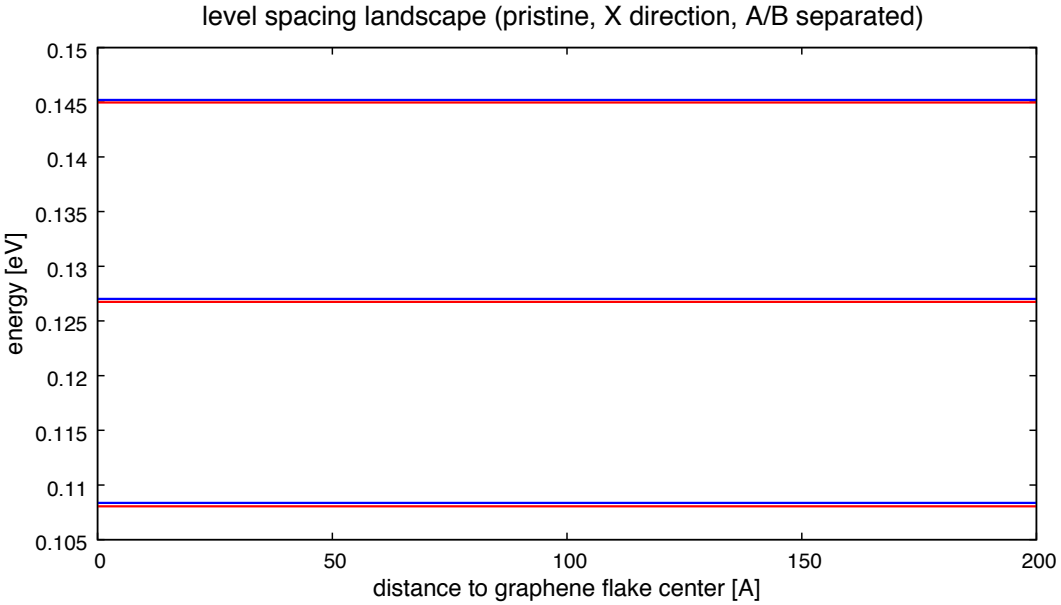

Figure 3.5.: Level spacing of the six lowest QDOT eigenstates depending on the distance of QDOT and flake center (pristine, no defect!) in x-directiono. Levels alternately color coded in red/blue for visibility.

As can be expected from this we find "degenerate" pairs of QDOT states whose level spacings (Δ_j^O and Δ_j^k) do not depend on the position relative to the flake center (Fig. 3.5).

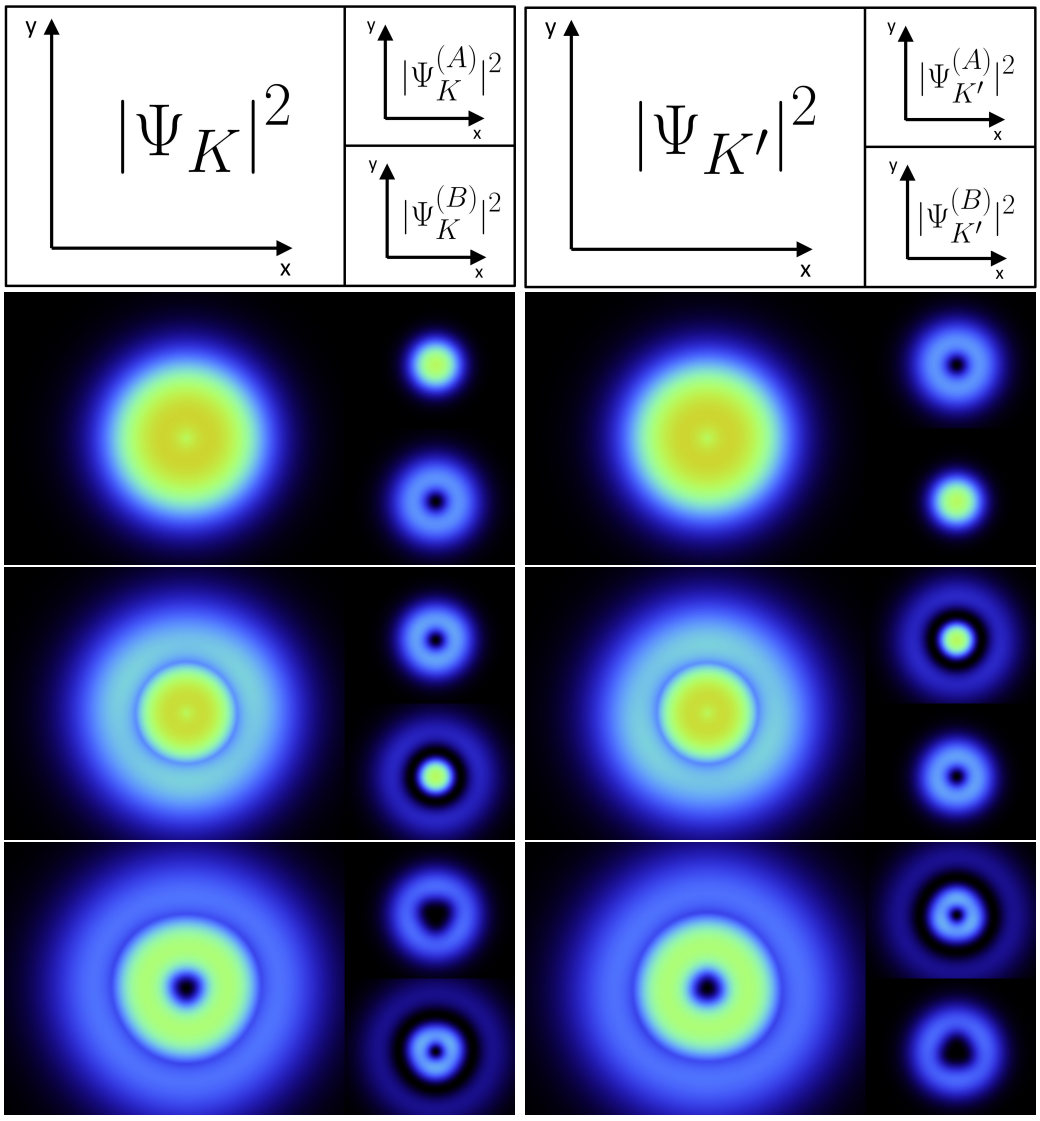

Figure 3.6.: Probability density of the first six QDOT states along with the densities present on each sublattice plotted in two smaller boxes stacked vertically to the right of each total density plot (see pictorial description at the top of the plot). Order: (top left) - P1, (top right) - P2, (center left) - P3, (center right) - P4, (bottom left) - P5, (bottom right) - P6, with P* indicating a Pristine state.

As can be seen in Fig. 3.6, we clearly find the eigenstate properties of (3.1, 3.2) with the degenerate pairs (horizontal) differ only by switching their respective sublattice projections (two smaller depictions at the righthand side of each of the six subplots). While the two lower pairs stay almost perfectly spherical we can identify some "trigonal" warping for state five and six (bottom of Fig. 3.6) representing the lattice symmetries of graphene.

3.2.2. Stone Wales defect

Embedding a defect into the center of our graphene flake we investigate the dependence of the level spacing (orbital Δ_j^O and valley Δ_j^k) on the distance and direction of the QDOT displacement (relative to the defect center). Since we can now take our pristine QDOT states as reference we can always use the projection $|\langle \Psi_{\text{defect}} | \Psi_{\text{pristine}} \rangle|^2$ to characterize the change of the wave function together with a change in level spacing. This projection will henceforth be included in our level spacing plots via color coding. A concise explanation of this projection is attempted in Fig. 3.7.

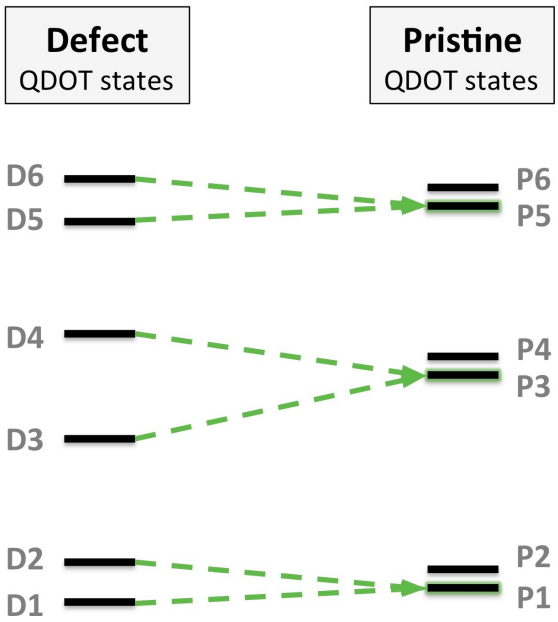

Figure 3.7.: Schematic explanation of the projection scheme used to determine the change of the defect QDOT states by projecting them onto the lower of the respective pristine QDOT state pair ($|\langle D1 | P1\rangle|^2$, $|\langle D2 | P1\rangle|^2$, ...).

Since the Stone Wales defect essentially represents two neighbouring atoms rotated 90 degrees — that is it removes no atoms and can be viewed as a very localized lattice distortion to the pristine lattice — we expect small level splittings and general likeness to the pristine states.

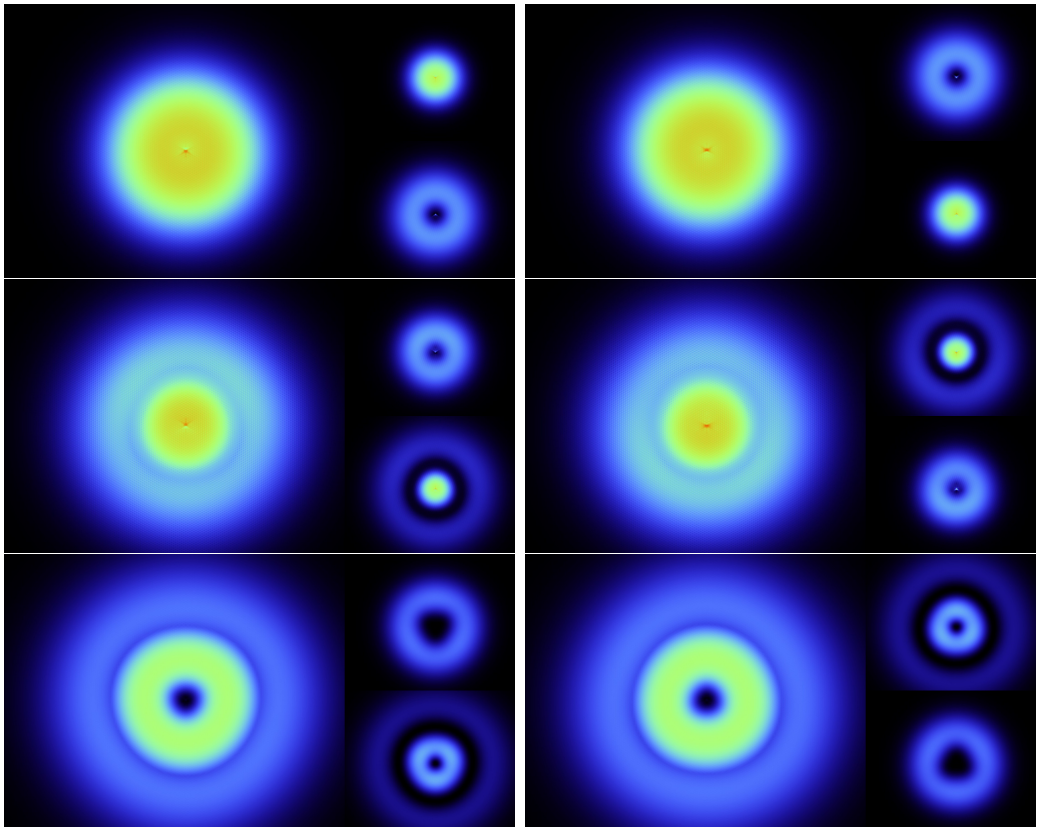

Figure 3.8.: Probability density of the first six QDOT states along with the densities present on each sublattice plotted in two smaller boxes stacked vertically to the right of each total density plot . Order: (top left) - D1, (top right) - D2, (center left) - D3, (center right) - D4, (bottom left) - D5, (bottom right) - D6, with D* indicating a Defect state.

Inspecting the QDOT states with the defect at its centre (Fig. 3.8) reveals states not unlike the ones of the pristine system with the only difference being very localized density accumulations at the defect site. Unlike prior defects we see no clear splitting of the valley-degenerate pairs (1^{st}-2^{nd}, 3^{rd}-4^{th}, 5^{th}-6^{th}) into more-localized and less-localized defect states.

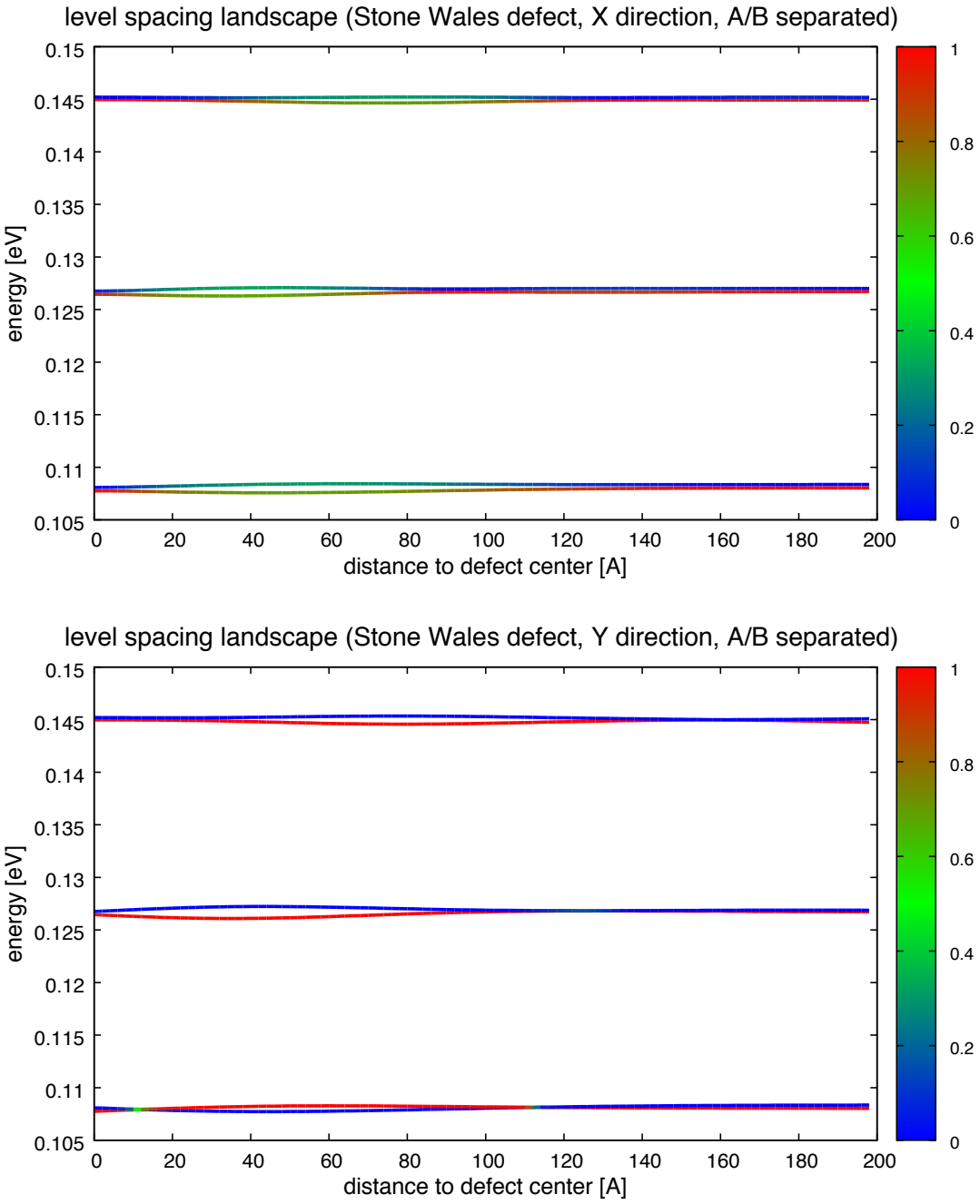

Figure 3.9.: Level spacing of the six lowest QDOT eigenstates depending on the relative distance of QDOT and defect center in **top)** x-direction and **bottom)** y-direction. Color coding represents the "K-projection" (see detailed explanation in the beginning of this section) onto the corresponding QDOT state of pristine graphene ($|\langle \Psi_{\text{defect}} \,|\, \Psi_{\text{pristine}} \rangle|^2$)

As can be seen in Fig. 3.9 our initial expectations are met quite well. In fact the defect is so weak that the "pristine ordering" (blue on top of red, caused by our A/B separation) remains unchanged for all positions. While orbital splitting Δ_j^O remains essentially unchanged for all relative positions, valley splitting in the order of 1-2meV can be found for all three orbitals at distances ranging from 1.5nm to 12nm.

There is however a clear difference in the QDOT state character (color scale in Fig. 3.23, explained on p. 35). While traversing in x direction causes a unitary rotation of the pristine states within the valley subspace (green color in Fig. 3.9) for QDOT-defect distances between 2nm and 11nm (which ultimately do not change the pristine ordering, blue on top of red), traversing in y direction shows very narrow mixing regions at 1nm and 11.5nm only for the two lowest levels and keeps the four higher levels unchanged (no green regions and blue on top of red for all positions).

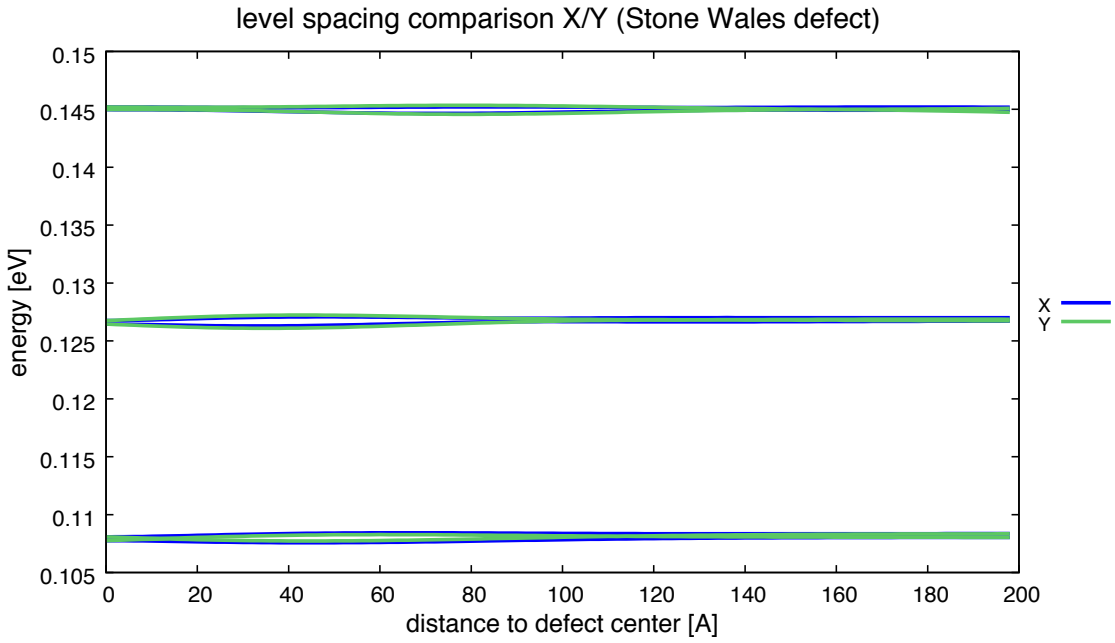

Figure 3.10.: Level spacing of the six lowest QDOT eigenstates depending on the relative distance of QDOT and defect center in both x and y direction

Since the Stone Wales defect is far from spherical we expect some form of directionality regarding its level splitting. The magnitudes of both orbital- and valley-splitting however do not seem to be very different when traversing in y (armchair) direction instead of in x (zigzag) direction (Fig. 3.10).

3.2.3. Si substitution

The Si substitution meets initial expectations of it being a rather "weak" defect quite well. In contrast to most other defects we feel hard pressed to see clear localization at the defect site. A very tight zoom would reveal some increase in density at the defect, resulting in a trigonal shape (respecting the trigonal symmetry of the defect).

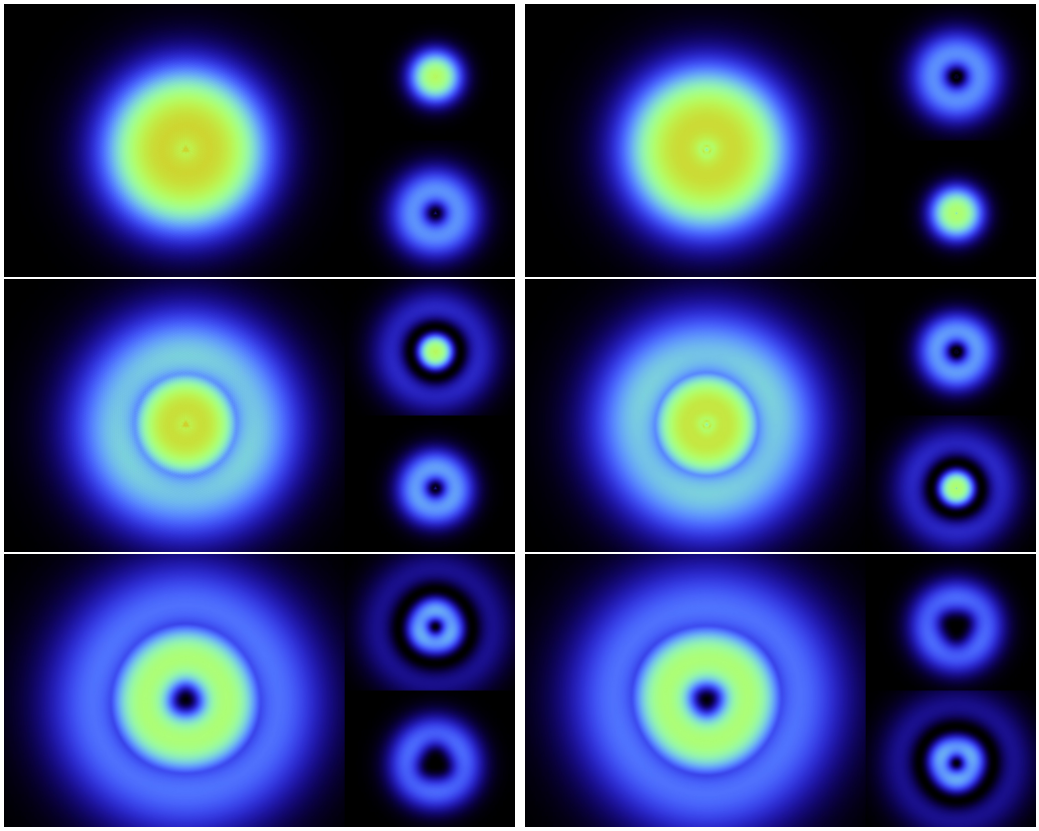

Figure 3.11.: Probability density of the first six QDOT states along with the densities present on each sublattice plotted in two smaller boxes stacked vertically to the right of each total density plot . Order: (top left) - D1, (top right) - D2, (center left) - D3, (center right) - D4, (bottom left) - D5, (bottom right) - D6, with D* indicating a Defect state.

We find a surprisingly strong similarity between the QDOT states of the Si substitution defect and their pristine counter parts (see Fig. 3.11). Valley splitting Δ_j^k caused by the Si defect is similar to the Stone Wales defect in the order of 1-2meV. This once again suggests that the degree in which the sublattice degree of freedom is broken (Si substitution sees only one sublattice change a C atom in a Si atom) does not directly result in a large valley splittings.

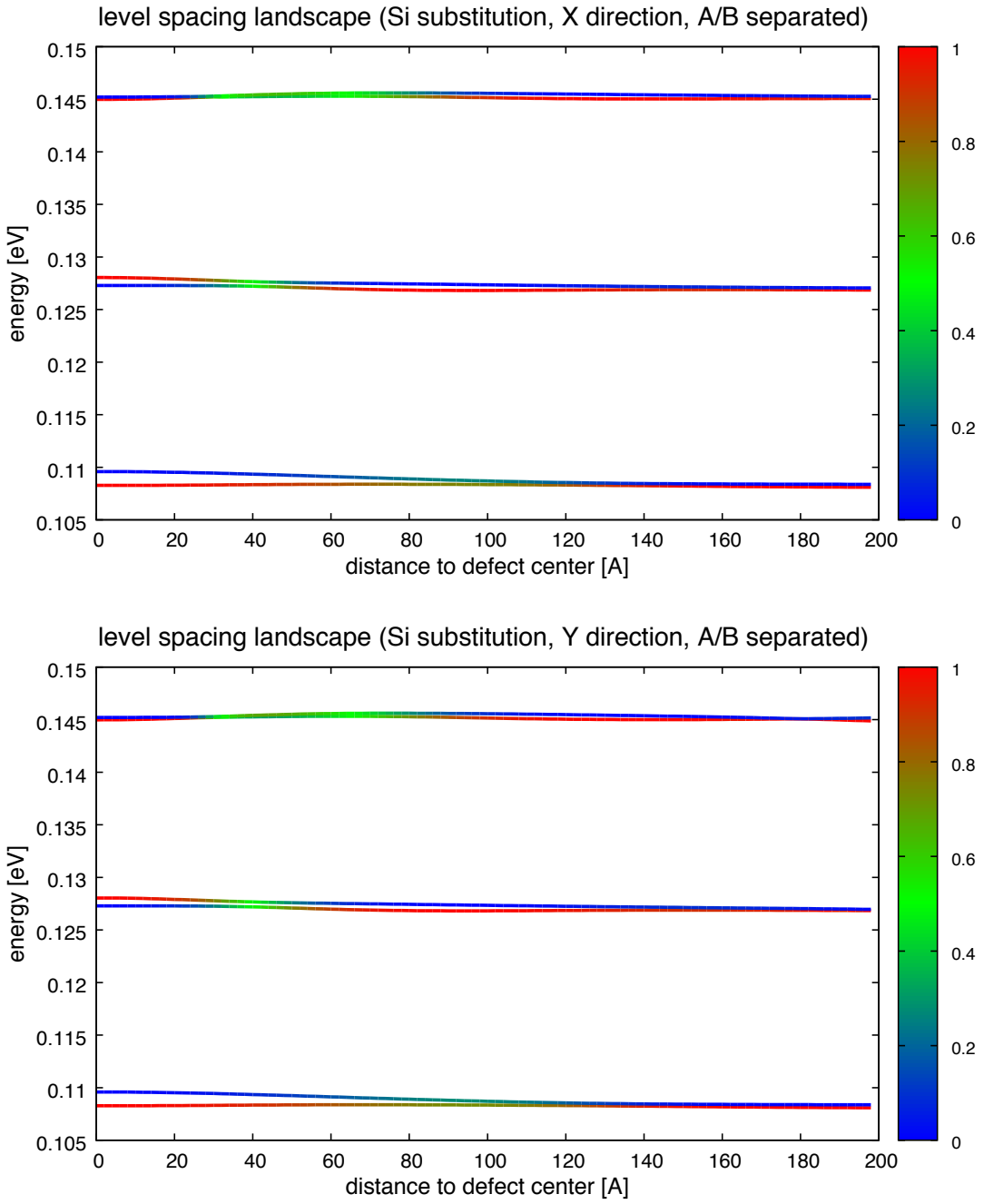

Figure 3.12.: Level spacing of the six lowest QDOT eigenstates depending on the relative distance of QDOT and defect center in **top)** x-direction and **bottom)** y-direction. Color coding represents the "K-projection" (see detailed explanation in the beginning of this section) onto the corresponding QDOT state of pristine graphene ($|\langle \Psi_{\text{defect}} \mid \Psi_{\text{pristine}} \rangle|^2$)

We again find that all states remain "pristine" at distance zero despite having density on the defect site. The most noticeable feature (regardless of displacement direction) is the relatively wide green region for the 5^{th} and 6^{th} state occuring when the defect traverses the wide density maximum of those states (Fig. 3.12).

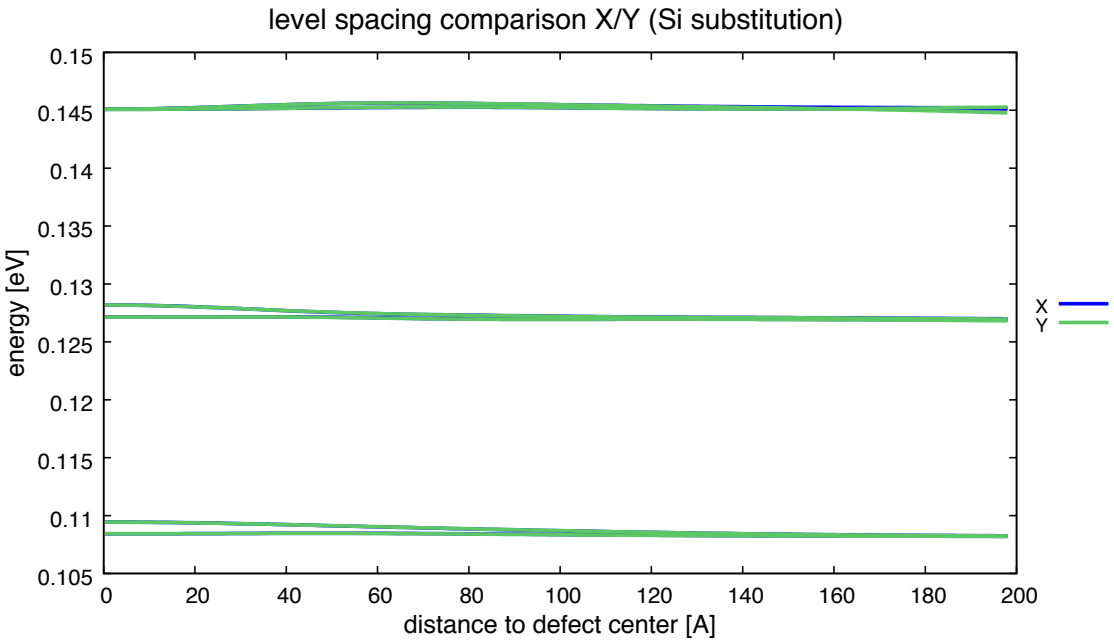

Figure 3.13.: Level spacing of the six lowest QDOT eigenstates depending on the relative distance of QDOT and defect center in both x and y direction

Similar to the Stone Wales defect, comparing x and y direction in Fig. 3.13 reveals the level splittings to be identical. This time however Fig. 3.12 also suggests that the projection (color scaling) is also identical.

3.2.4. Single vacancy defect

Since the DFT calculation of the single vacancy defect proved to be much more time consuming (not to mention computationally demanding) than initially expected (see section 3.1) we do not yet have a correctly converged wannierized tight binding description for this defect. However in contrast to Stone Wales defect and Si substitution the single vacancy allows us to implement a poor man's description by setting the onsite energy of a specific lattice place to arbitrarily high values while setting all hopping to the site to zero. Results of this description can be used as a reference for the "full" defect description used in future calculations.

simple single vacancy defect

The simple variant of the single vacancy displays somewhat different properties to most other defects. While we usually found the valley pair to split (Δ_j^k) into an energetically lower state that is highly localized around the defect site and an energetically higher one with much less density at the defect, the situation appears inverted for the single vacancy (Fig. 3.14). The states that localize around the defect feature higher energy.

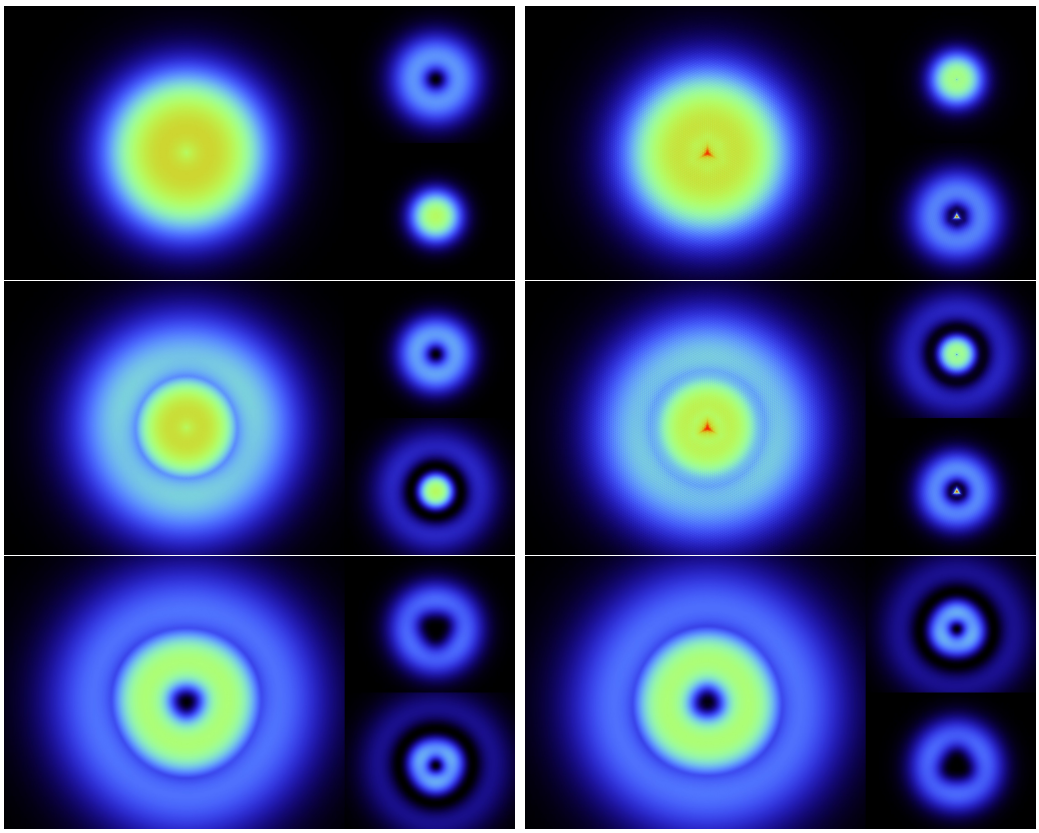

Figure 3.14.: Probability density of the first six QDOT states along with the densities present on each sublattice plotted in two smaller boxes stacked vertically to the right of each total density plot . Order: (top left) - D1, (top right) - D2, (center left) - D3, (center right) - D4, (bottom left) - D5, (bottom right) - D6, with D* indicating a Defect state.

More generally the valley splitting (Δ_j^k) seems to act very asymmetric, with the energy of the ultimately lower state almost unchanged (Fig. 3.15). This appears to reflect that we break the sublattice symmetry in an uneven way by effectively removing an atom of only one sublattice. We again find no clear correlation between valley splitting (Δ_j^k) and the character of the associated states (color scale of the pristine projection in Fig. 3.15).

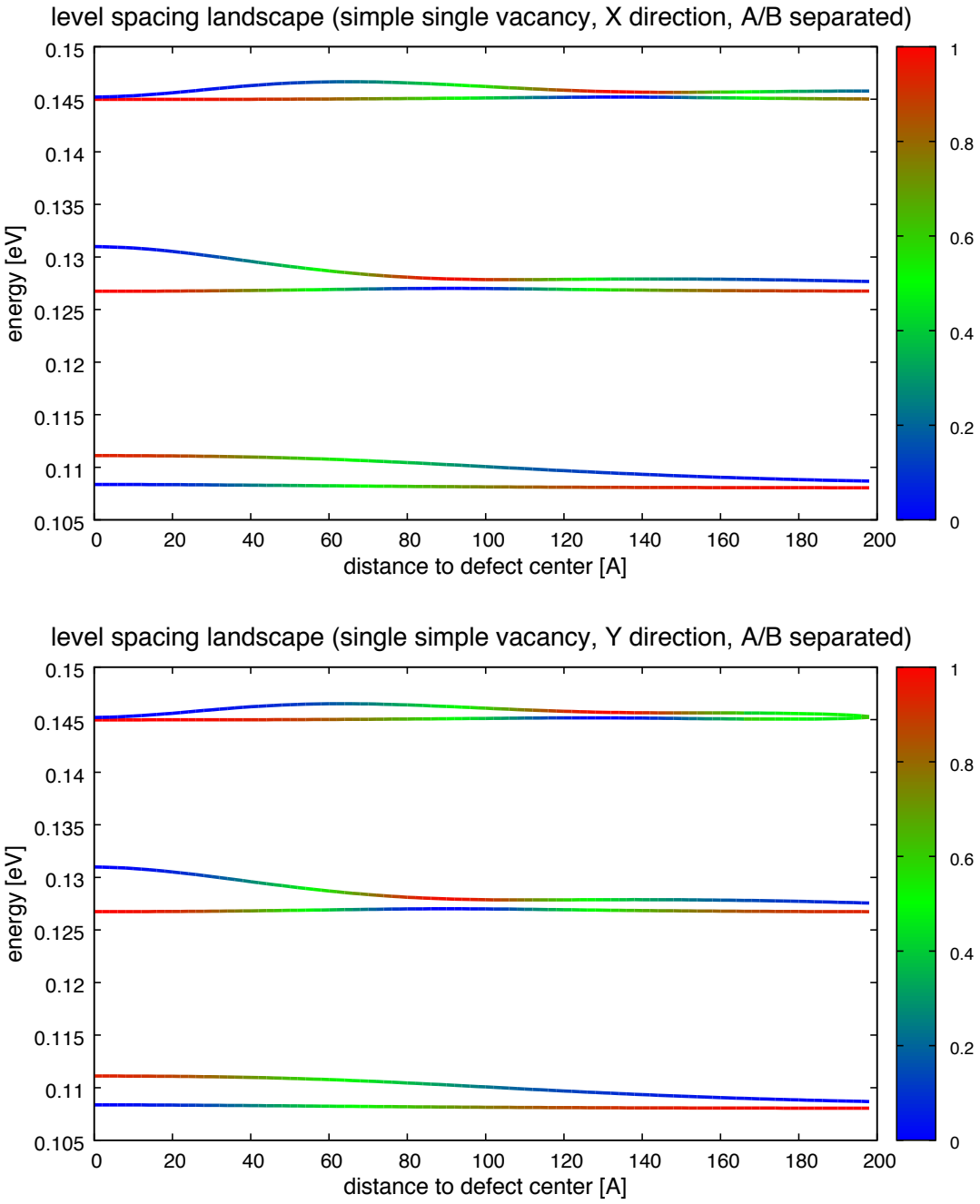

Figure 3.15.: Level spacing of the six lowest QDOT eigenstates depending on the relative distance of QDOT and defect center in **top)** x-direction and **bottom)** y-direction. Color coding represents the "K-projection" (see detailed explanation in the beginning of this section) onto the corresponding QDOT state of pristine graphene ($|\langle \Psi_{\text{defect}} | \Psi_{\text{pristine}} \rangle|^2$)

While the density distribution of the states themselves remains mostly pristine (blue/red color scale) — even with the QDOT right on top of the defect — we still encounter a sizable (asymmetric) valley splitting Δ_j^k (approx. 3-5meV) for the four lowest QDOT states. While such a splitting is not present for the 5^{th} and 6^{th} states (as with all other defects due to a lack of density at the origin), the 3^{rd} and 4^{th} states remain noticeably split up to a distance of about 9nm and the 1^{st} and 2^{nd} level reach their effectively pristine splitting only for QDOT-defect distances greater than 18nm. We also find various avoided crossings that connect regions of different valley ordering (red → blue / blue → red) along both zigzag (x) and armchair (y) directions.

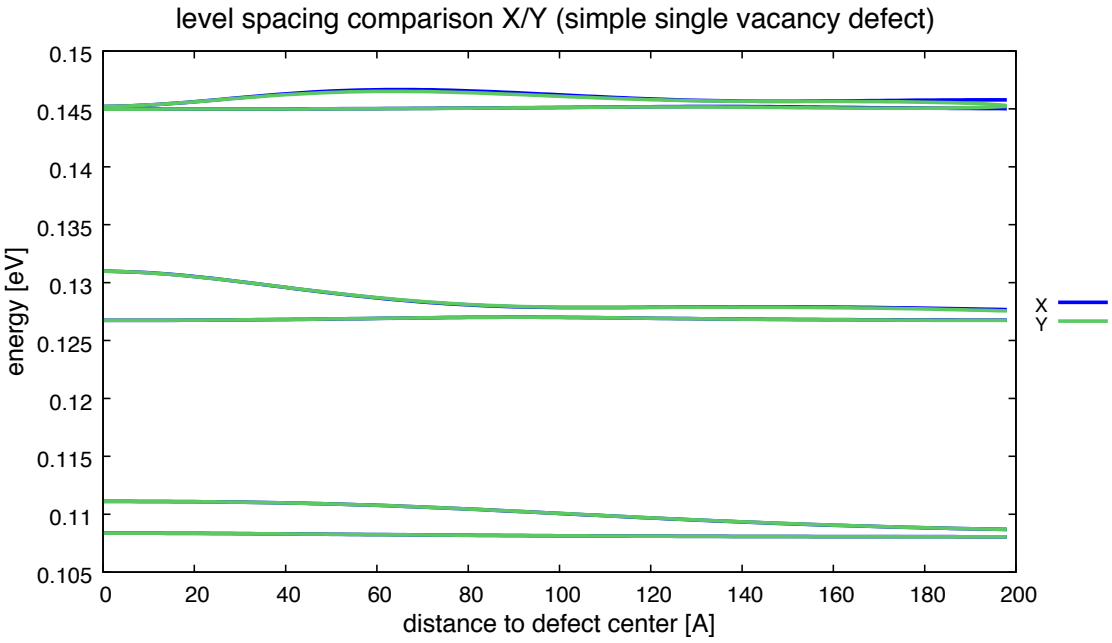

Figure 3.16.: Level spacing of the six lowest QDOT eigenstates depending on the relative distance of QDOT and defect center in both x and y direction

We calculate almost identical level spacing landscapes for both traversing directions as can be expected from a highly point symmetric defect type (Fig. 3.16).

3.2.5. double vacancy defect

Contrary to initial expectations the double defect seems to be a very "strong" type of defect and appears to break the valley degeneracy in a peculiar way. Despite affecting both sublattices equally (both lack one C atom) we see large, asymmetric valley splittings Δ_j^k (approx. 8-13meV) when the QDOT is on top of the defect with wave functions that appear to be almost perfect admixtures of the pristine states (green color coding in Fig. 3.8 and Fig. 3.9). Unlike all the previous defects the double vacancy causes not only a unitary rotation in the initially degenerate valley subspace but also leaves this subspace to a significant degree. The sum of squared projections does not add up to 1 ($|\langle\Psi^{(k)}_{\text{defect}}|\Psi^{(k)}_{\text{pristine}}\rangle|^2 + |\langle\Psi^{(k')}_{\text{defect}}|\Psi^{(k)}_{\text{pristine}}\rangle|^2 \neq 1$). For some positions this sum gives a value as low as 0.75. This is also apparent in Fig 3.17 by the different (and not complimentary) shades of green within the respective valley subspaces at all those positions that exhibit strong defect localization and hence strong valley splitting. This stems from the fact that our pristine QDOT states are no longer a sufficient basis to describe the strong localization caused by this defect type.

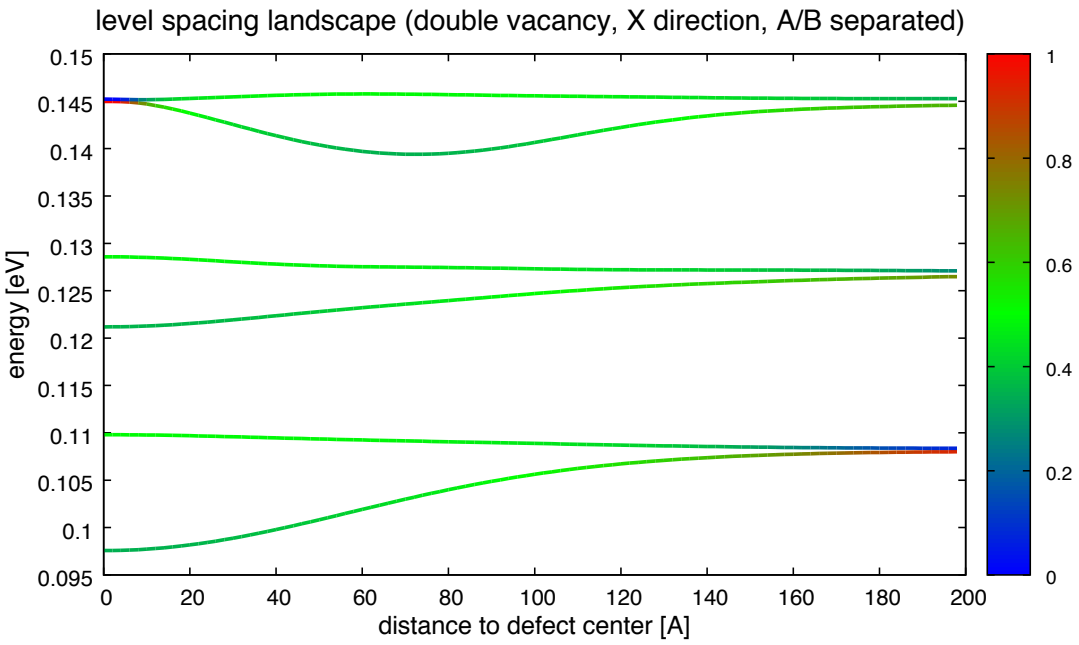

Figure 3.17.: Level spacing of the six lowest QDOT eigenstates depending on the relative distance of QDOT and defect center in **x-direction**. Color coding represents the "K-projection" (see detailed explanation in the beginning of this section) onto the corresponding QDOT state of pristine graphene ($|\langle\Psi_{\text{defect}}|\Psi_{\text{pristine}}\rangle|^2$)

This pronounced level splitting at zero distance is much weaker for the 3^{rd} and 4^{th} states while state five and state six are very akin to the pristine counter part and virtually degenerate. Understanding this is most simply done via Fig. 3.18 where we again plot the density of the first six QDOT states (at distance zero). Similar to the pristine system we see no density at the center for states five and six. These states are thus incapable of detecting the lattice defect and stay "pristine" in character, as they have for all defect types investigated.

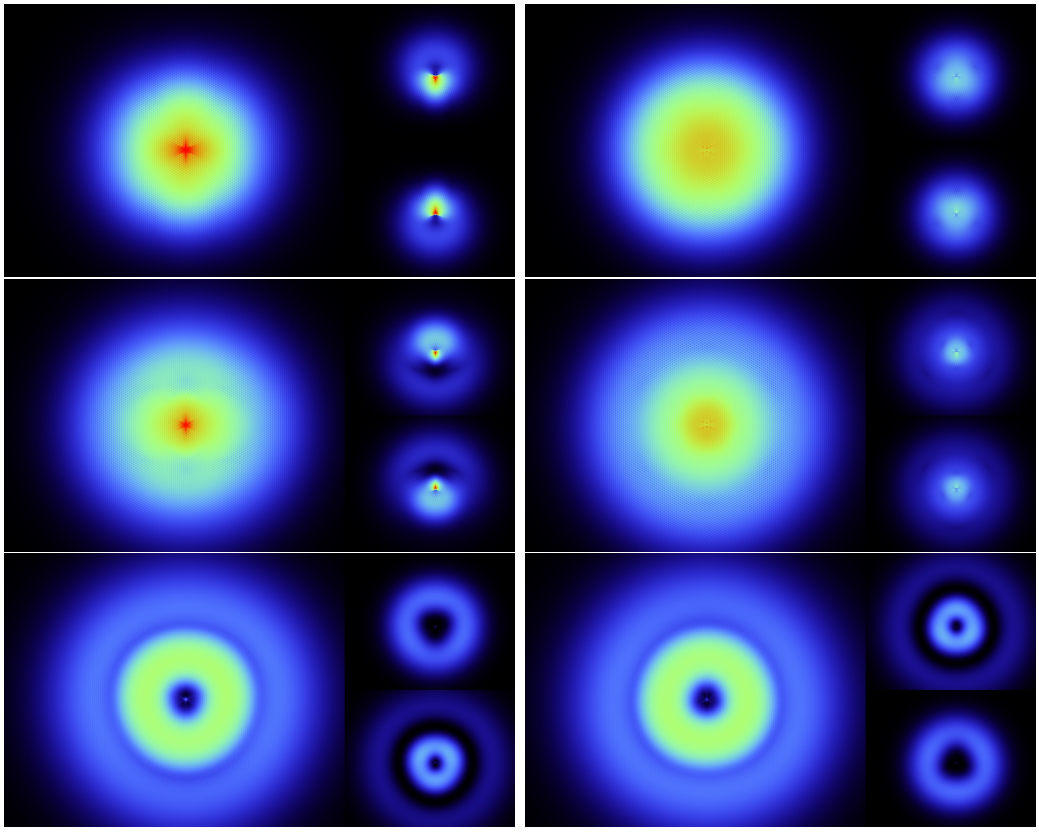

Figure 3.18.: Probability density of the first six QDOT states along with the densities present on each sublattice plotted in two smaller boxes stacked vertically to the right of each total density plot . Order: (top left) - D1, (top right) - D2, (center left) - D3, (center right) - D4, (bottom left) - D5, (bottom right) - D6, with D* indicating a Defect state.

We also observe that for each "valley pair" the lower of the two states seems to strongly localize on the defect and exhibits an interesting segregation in real space when plotting only the density on the respective sublattice A/B (Fig. 3.18). This segregation (level 1 plotted in the top left of Fig. 3.18: sublattice A $\rightarrow$ south orientation, sublattice B $\rightarrow$ north orientation) remains unchanged when inverting the sign of $\vec{B}$. It is also present for the less localized states, albeit in a much less pronounced form.

Displacing the QDOT potential in x-direction reveals a profound stability of the observed valley mixing. States five and six quickly start to populate the defect site with density and are thus also subject to increasing valley splitting Δ_j^k. This mixing/splitting holds for quite some distance for all six states. The lowest two and thus spatially narrowest states begin to slowly fall back to their pristine character at a distance of about 180Å. The higher states which are larger in real space will return to their pristine state at slightly larger distances which we chose not calculate with this setup due to possible interplay of our QDOT steadily approaching the "open" flake border.

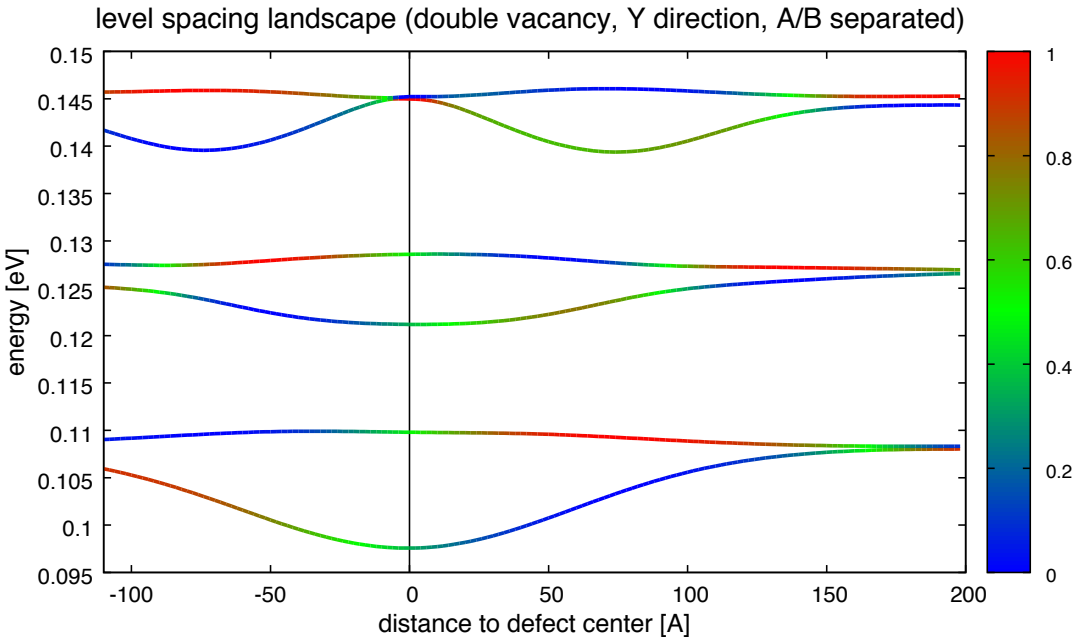

Figure 3.19.: Level spacing of the six lowest QDOT eigenstates depending on the relative distance of QDOT and defect center in **y-direction**. Color coding represents the "K-projection" (see detailed explanation in the beginning of this section) onto the corresponding QDOT state of pristine graphene ($|\langle \Psi_{\text{defect}} | \Psi_{\text{pristine}} \rangle|^2$)

Displacement in y direction renders quite a different picture (Fig. 3.19). Due to the north/south weighted sublattice segregation discussed in the second last paragraph the expected symmetry ($+y$ direction equivalent to $-y$ direction) is not fully realized. While the valley splitting Δ_j^k itself seems to respect this symmetry, the character of the associated states is vastly different when displacing the QDOT a certain distance in $+y$ or $-y$ direction.

Moving the QDOT in $-y$ direction sees the admixture (for 1^{st}-2^{nd} states) fall back to pristine character after only about 50Å while displacement in $+y$ direction sees them become "inverted pristine" for about 150Å before the total defect influence subsides and reveals pristine states in the "correct order". Looking at the higher state pairs (3^{rd}-4^{th}, 5^{th}-6^{th}) reveals similar behaviour albeit more avoided crossings are present before permanently reaching "correct pristine" character. This directionality of the double defect which entails fairly opposite behaviour for the $+y$ and $-y$ direction in combination with a pretty stable admixing for the x direction makes it one of the "strongest" and most interesting defects we have investigated so far. Dropping the color coding for the level separation plots and combining x and y direction yields Fig. 3.20. Despite the drastically different character of the associated states we see little difference for the level separation acquired in the different directions. However, compared to Si substitution, Stone Wales defect and single vacancy which all feature point symmetry these marginal differences are comparatively large.

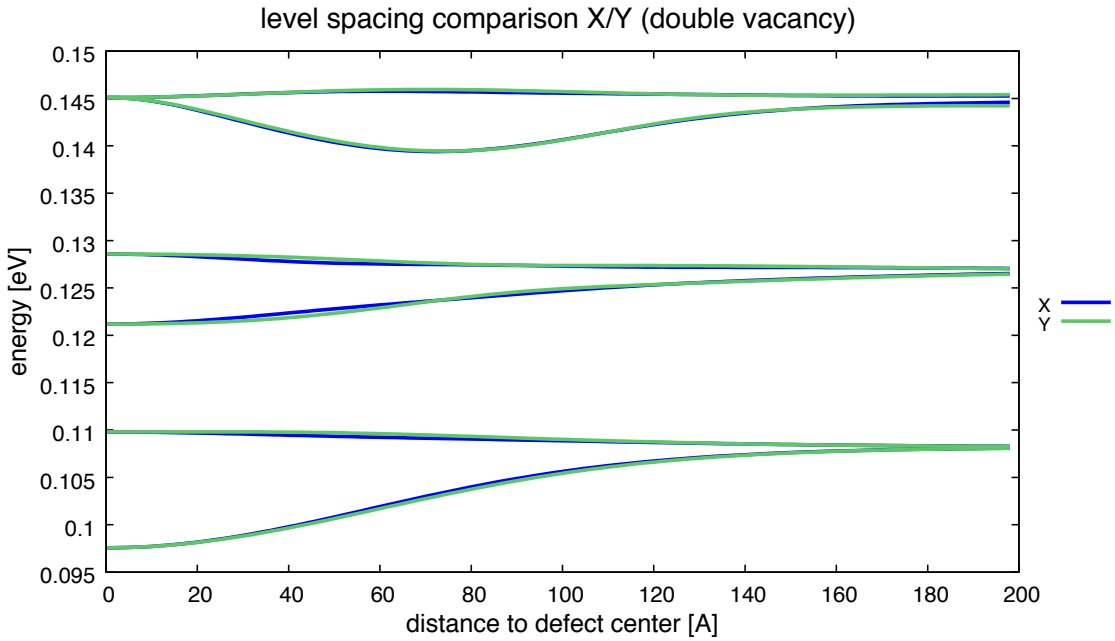

Figure 3.20.: Level spacing of the six lowest QDOT eigenstates depending on the relative distance of QDOT and defect center in both x and y direction

Simple double vacancy defect

As a sort of consistency check we can perform the very same calculations for the poor man's description of the double defect (setting the on-site energy of two adjacent atoms to ridiculously large values while putting all hopping terms to those sites to zero).

As displayed through Fig. 3.12 and 3.13 we see a quantitative change for the valley splitting Δ_j^k which is in general much lower for the simple defect description. The associated states again display enhanced localization on the defect site for the lower of the valley state pairs and again exhibit a much less pronounced north/south segregation in the sublattice density plots (overall defect now smaller → harder to discern without close zoom). Qualitatively we see good agreement for the level spacing plots in both x and y direction with the number and position of avoided crossings matching those of the "full" defect description.

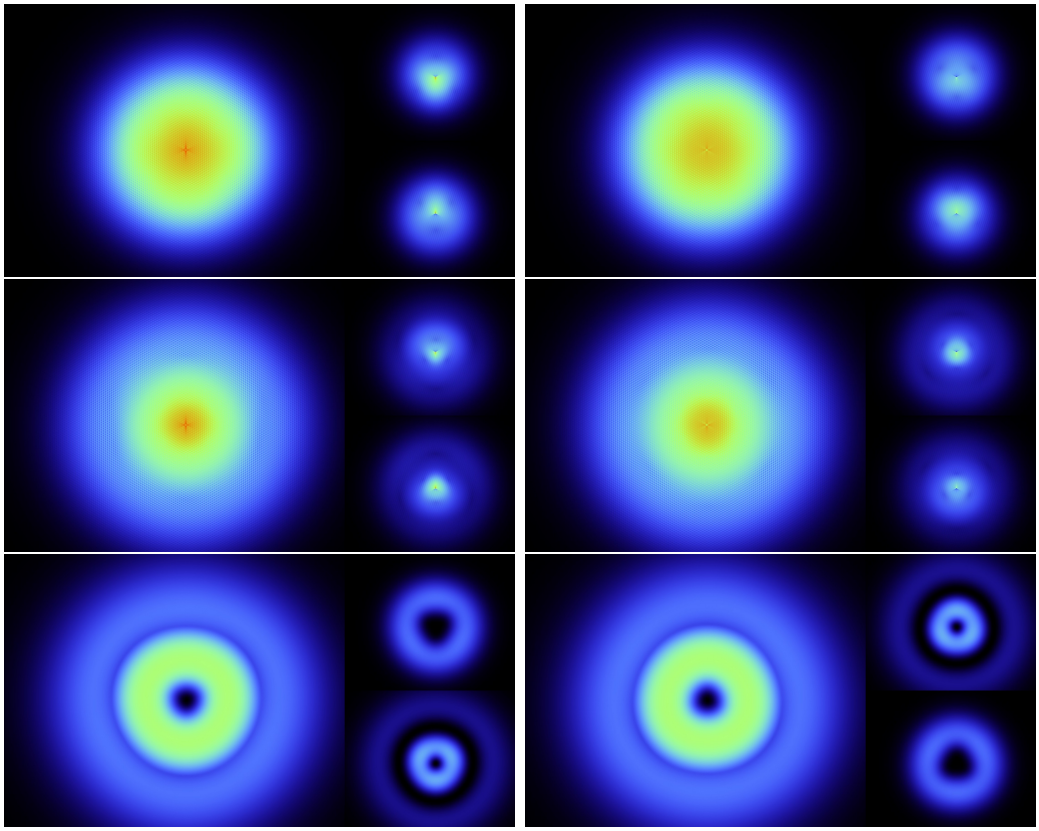

Figure 3.21.: Probability density of the first six QDOT states along with the densities present on each sublattice plotted in two smaller boxes stacked vertically to the right of each total density plot . Order: (top left) - D1, (top right) - D2, (center left) - D3, (center right) - D4, (bottom left) - D5, (bottom right) - D6, with D* indicating a Defect state.

We notice that the valley splitting Δ_j^k is not only smaller for the poor man's description (approx. 3-4meV) but also much more symmetric. The localization effects of this description seem to be suppressed as well since the color scale remains complementary for all positions in both directions ($|\langle\Psi^{(k)}_{\text{defect}}|\Psi^{(k)}_{\text{pristine}}\rangle|^2 + |\langle\Psi^{(k')}_{\text{defect}}|\Psi^{(k)}_{\text{pristine}}\rangle|^2 \approx 1$).

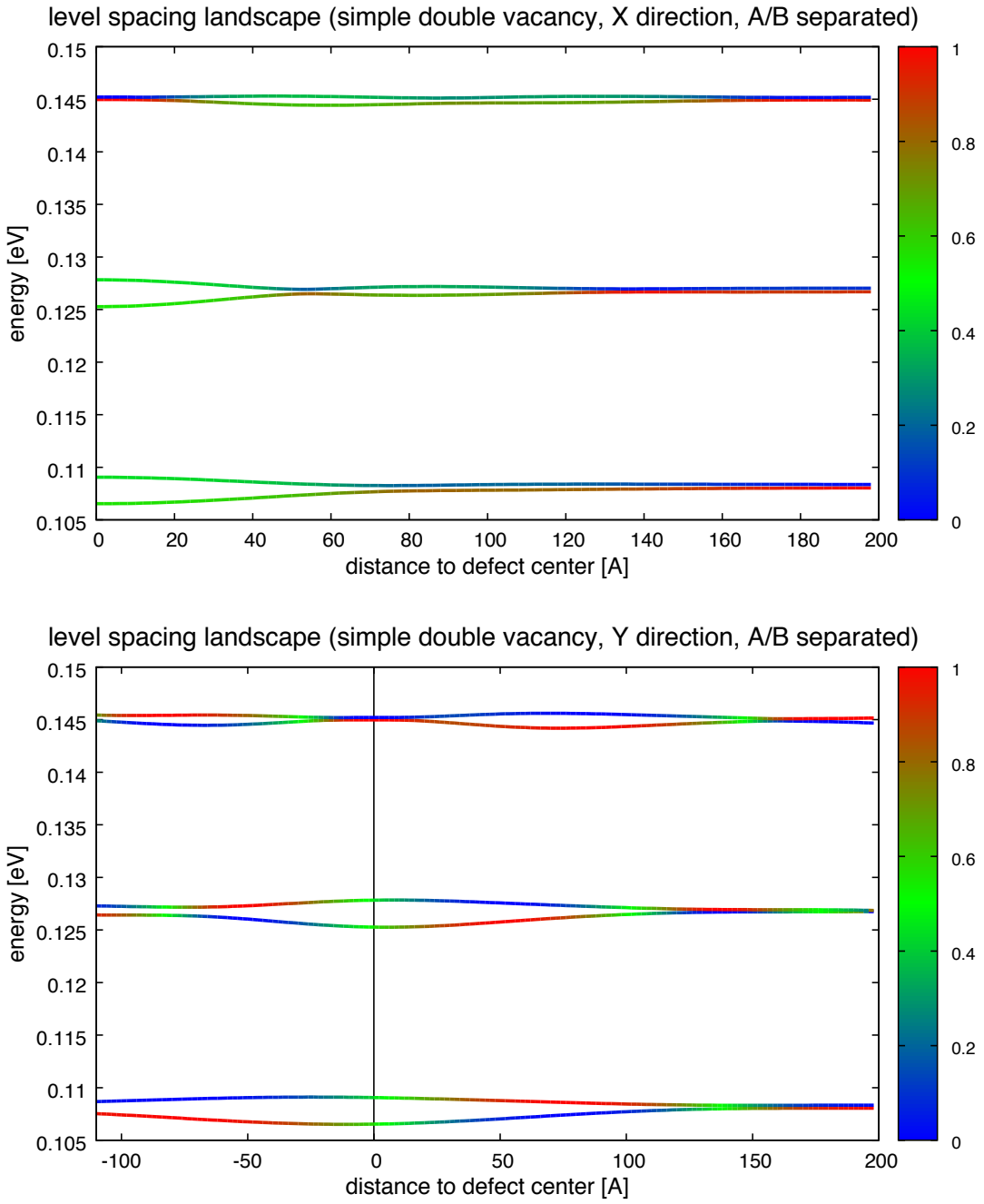

Figure 3.22.: Level spacing of the six lowest QDOT eigenstates depending on the relative distance of QDOT and defect center in **top)** x-direction and **bottom)** y-direction. Color coding represents the "K-projection" (see detailed explanation in the beginning of this section) onto the corresponding QDOT state of pristine graphene ($|\langle \Psi_{defect} | \Psi_{pristine} \rangle|^2$)

3.2.6. Flower defect

The flower defect has sixfold rotational symmetry which is represented in the respective QDOT states in the form of a star-like density pattern at the defect. We again find the energetically lower states to localize more strongly. At distance zero the four lower states are equal mixtures of the pristine counterparts while the highest two again lack the necessary density on the defect site and remain pristine.

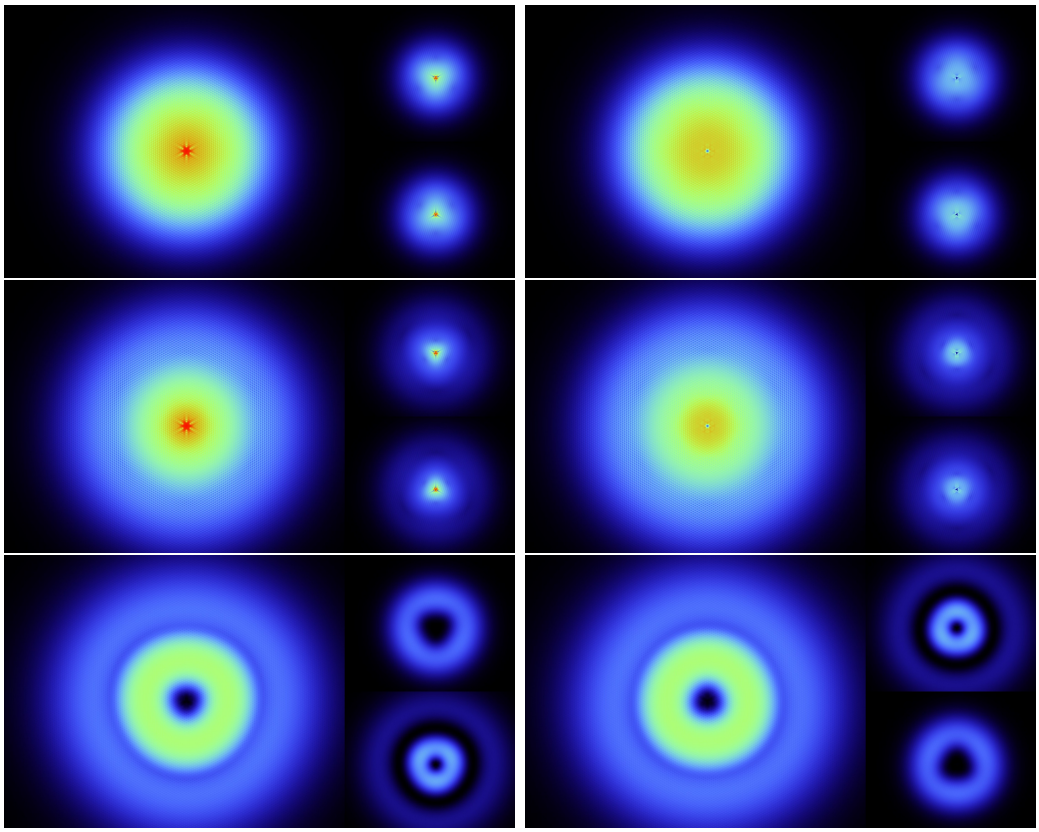

Figure 3.23.: Probability density of the first six QDOT states along with the densities present on each sublattice plotted in two smaller boxes stacked vertically to the right of each total density plot . Order: (top left) - D1, (top right) - D2, (center left) - D3, (center right) - D4, (bottom left) - D5, (bottom right) - D6, with D* indicating a Defect state.

Projection of the density onto each sublattice (Fig. 3.23) reveals a decomposition of the six-fold pattern into two trifold patterns rotated 60° against each other. This however does not lead to the surprising symmetry breaking found with the double defect. The valley splitting in $+y$ and $-y$ direction is now perfectly symmetric in both its value and the character of the associated QDOT states (projection onto pristine states $\rightarrow$ color coding).

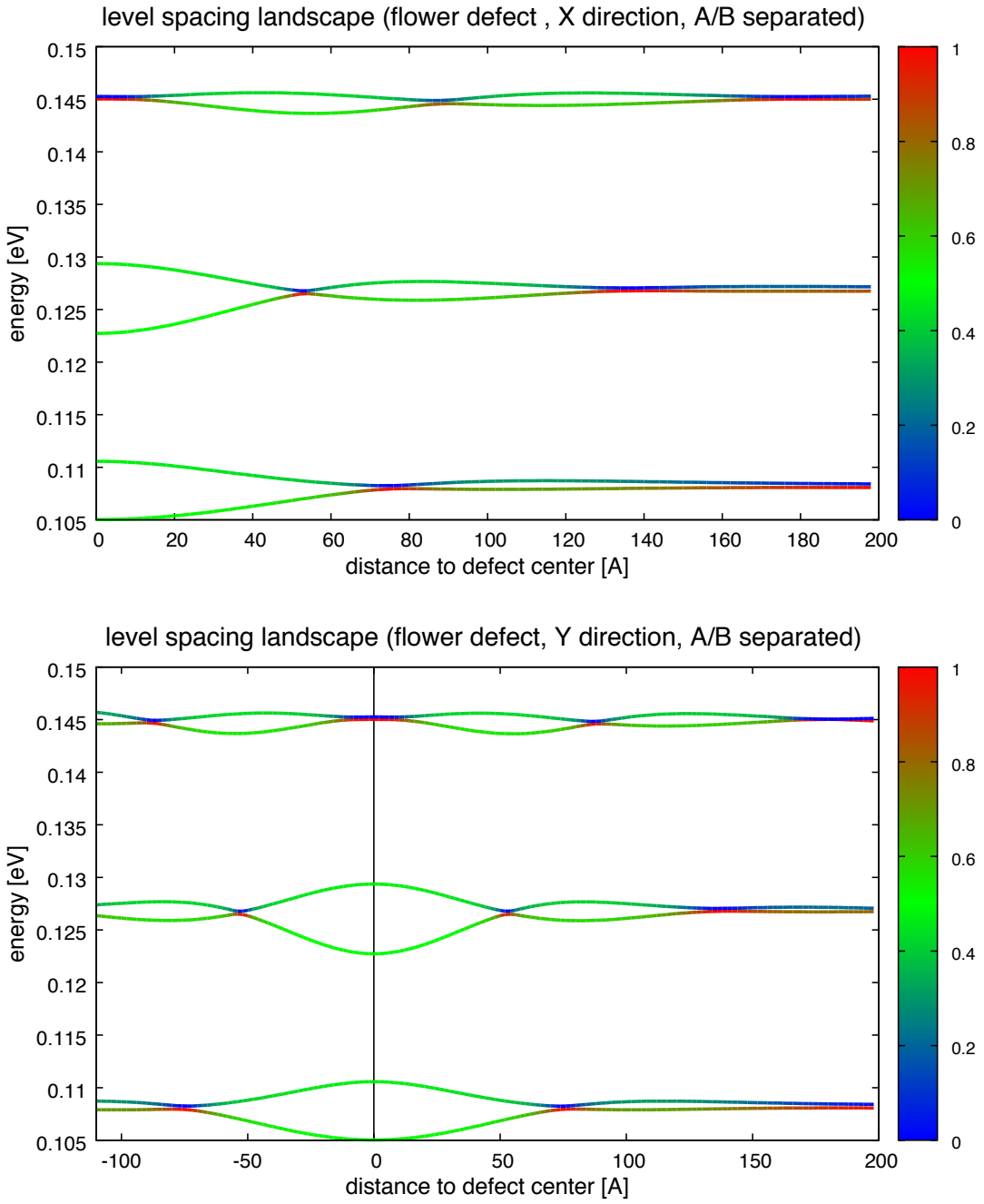

Figure 3.24.: Level spacing of the six lowest QDOT eigenstates depending on the relative distance of QDOT and defect center in **top)** x-direction and **bottom)** y-direction. Color coding represents the "K-projection" (see detailed explanation in the beginning of this section) onto the corresponding QDOT state of pristine graphene ($|\langle \Psi_{\text{defect}} \,|\, \Psi_{\text{pristine}} \rangle|^2$)

Compared to the double defect we now encounter a valley splitting Δ_j^k much more symmetric with respect to the degenerate pristine energy levels while the total magnitude of the splitting is of the same order of magnitude (approx. 5-7meV). Both displacement direction show much more pronounced avoided crossings. Those avoided crossings are of different nature this time since they are more naturally viewed as crossings of defect-mixed states that briefly demix into pristine character (the double defect in y direction featured comparatively more pristine like regions (red/blue) with only brief mixing regions (green)).

Interestingly enough it stands out that a green mixing region for this defect connects two regions of the same pristine ordering (blue on top of red) (Fig. 3.24) while the double defect in y direction always saw green regions "causing" an inversion of red and blue states (Fig. 3.19).

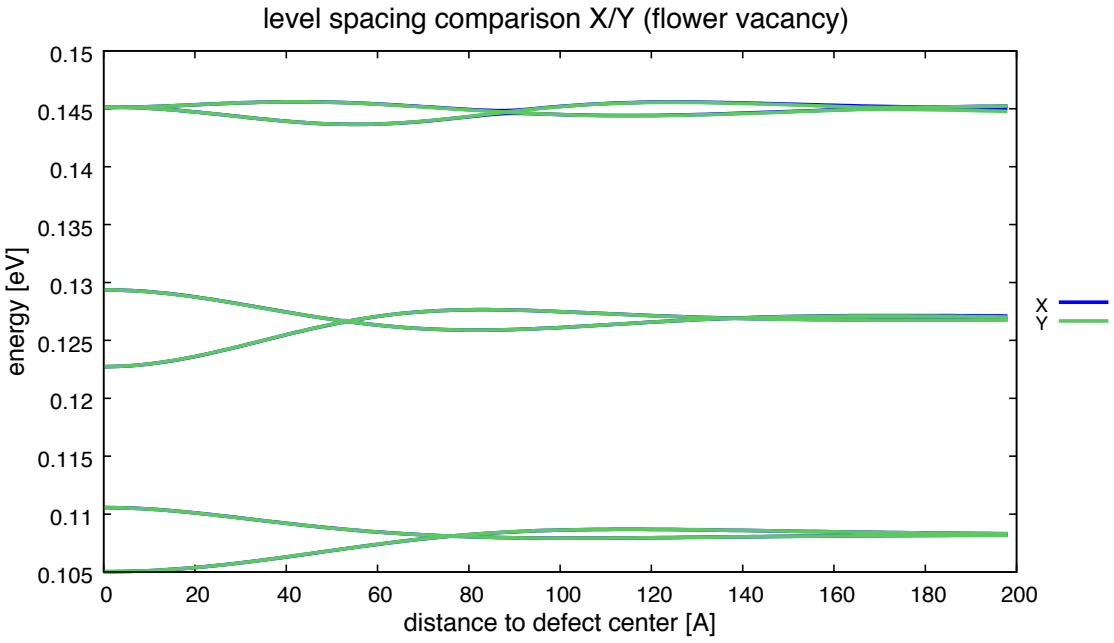

Figure 3.25.: Level spacing of the six lowest QDOT eigenstates depending on the relative distance of QDOT and defect center in both x and y direction

Omitting the projection color scale for the level spacing plots it becomes very apparent that the sixfold rotational symmetry of the flower defect means that displacing in x or y direction makes virtually no difference to the observed spacing (Fig. 3.25).

3.2.7. Defect comparison

Comparing the level spacing landscapes of the various defects (Fig. 3.26) proves our initial expectations conceived from geometrical properties of the defects (overall size, expected degree of breaking the sublattice symmetry, type I) or II) classification). The flower defect, despite being spatially largest, causes relatively large valley splitting Δ_j^k, the double vacancy however still surpasses it significantly. Since removing atoms can be interpreted as a much stronger perturbation to the lattice than simply changing their positions, this seems plausible. It also suggests that removing two adjacent atoms (that means constituents of different sublattices) does in no way break the sublattice symmetry any less. Orbital splittings Δ_j^O are essentially unaffected by the presence of lattice defects. These are primarily defined by the specific choice of electrostatic confinement potential.

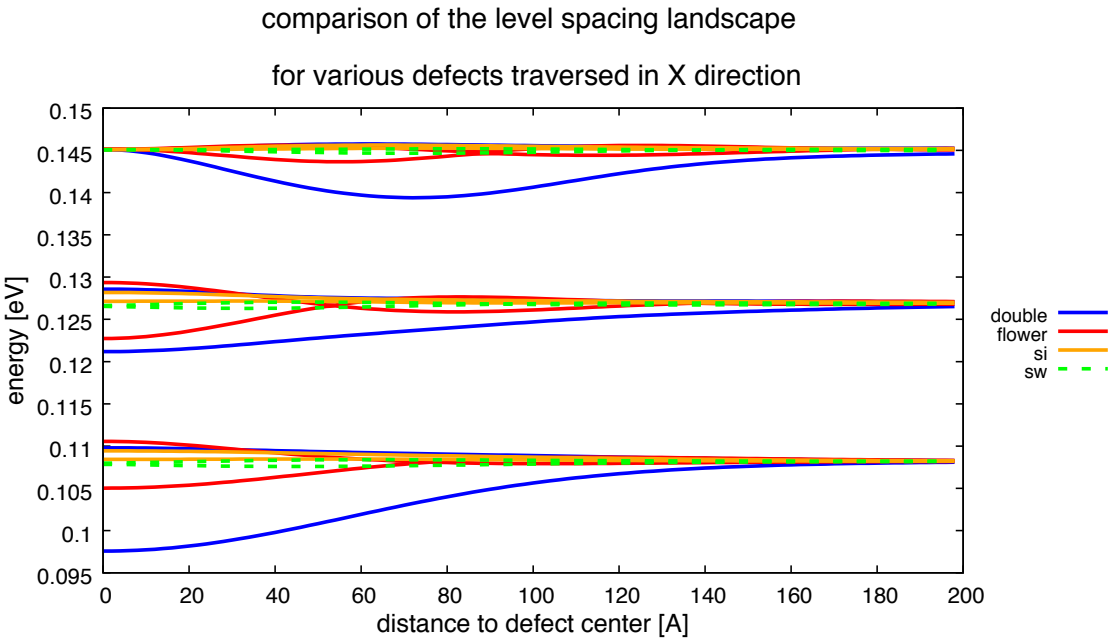

Figure 3.26.: QDOT-defect distance dependent level spacing for the four types of defects which allowed for a symmetrized DFT embedding scheme.

The Si substitution also shows very little level spacing, since Si is very similar to C and thus introduces little perturbation. Since the substitution only affects one sublattice we find an asymmetric valley splitting Δ_j^k. This asymmetry, however, is still much smaller than that introduced by removing two C atoms (double vacancy) which is somewhat counterintuitive. The Stone Wales defect is kindred to the flower defect (almost rigidly rotating a certain region of the original lattice) but shows smaller valley splitting due to its overall smaller size.

3.2.8. Influence of correlated disorder

Aiming to be predictive for experimental realization we investigate the influence of long range disorder, which will most definitely be present (be it from specific substrates or other external sources) in an experimental setup.

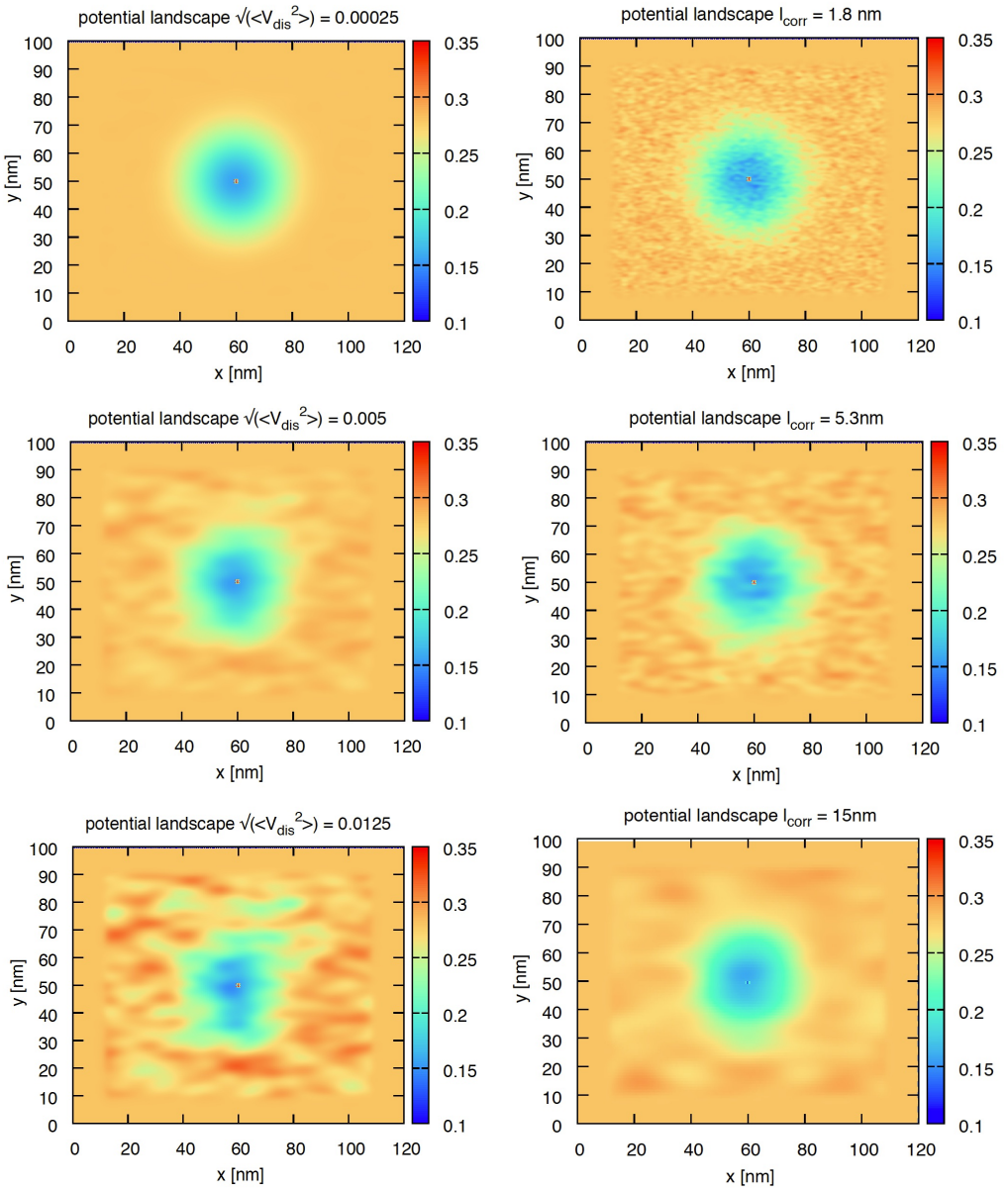

Figure 3.27.: Total potential of the graphene flake (embedded defect + STM tip + correlated disorder) with **left column)** varying amplitude and **right column)** varying correlation length. Mind the cutoff for the disorder near the system edges to keep the open boundary conditions fully unscathed.

We choose to recalculate the level spacing landscapes for both double vacancy in x direction (which displayed long range mixing of the pristine states) and for the flower defect in x direction (which featured pronounced avoided crossings), this time including a long range disorder potential with varying amplitude and correlation length (Fig. 3.27). To avoid messing with our "localized states filter" (open boundary conditions give all the states not localized at the defect an increased imaginary part to their eigenenergies) we omit applying our disorder potential on the outskirts of our graphene flake (with measurements $W_x \times W_y$) by a applying a proper weighting function (3.3) that introduces a smooth cut off towards the flake boundaries (also visible in Fig. 3.27). Assessing possible changes will tell us how resilient to disorder our QDOT-defect properties will be in an actual experiment.

$$f(x,y) = \frac{1}{1+e^{\frac{(0.1W_x - x)}{8}} + e^{\frac{(x-0.9W_x)}{8}}} \times \frac{1}{1+e^{\frac{(0.1W_y - y)}{8}} + e^{\frac{(y-0.9W_y)}{8}}} \tag{3.3}$$

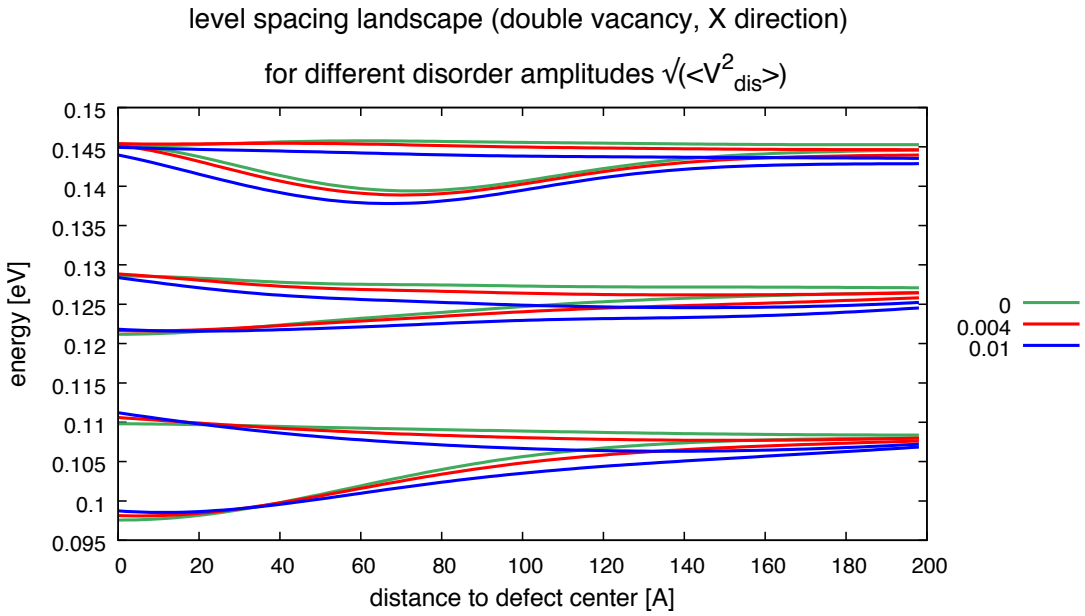

Figure 3.28.: Level spacing landscape of the double vacancy defect for varying disorder potential amplitude of 0 eV (green), 4 meV (red) and 10 meV (blue), ($l_{\text{corr}} = 8.8nm$ fixed).

Fig. 3.28 presents the results for the level spacing of the double vacancy traversed in x direction for varying the amplitude ($\sqrt{\langle V_{\text{dis}}^2 \rangle}$) of the correlated disorder. It appears as though the disorder merely shifts the QDOT levels locally without affecting valley splittings Δ_j^k.

Once the disorder is sufficiently strong, the loss of the mirror symmetry of the original setup is reflected by the QDOT levels no longer starting horizontally at zero QDOT-defect distance. Adding the projection onto the corresponding pristine QDOT states (that is pristine without disorder) as has been introduced on p. 41, as a color scale, gives Fig. 3.29. While the overall appearance seems similar for all disorder strengths we see that the pristine character (blue on top of red) of levels five and six is lost with disorder strengths of 4meV and above.

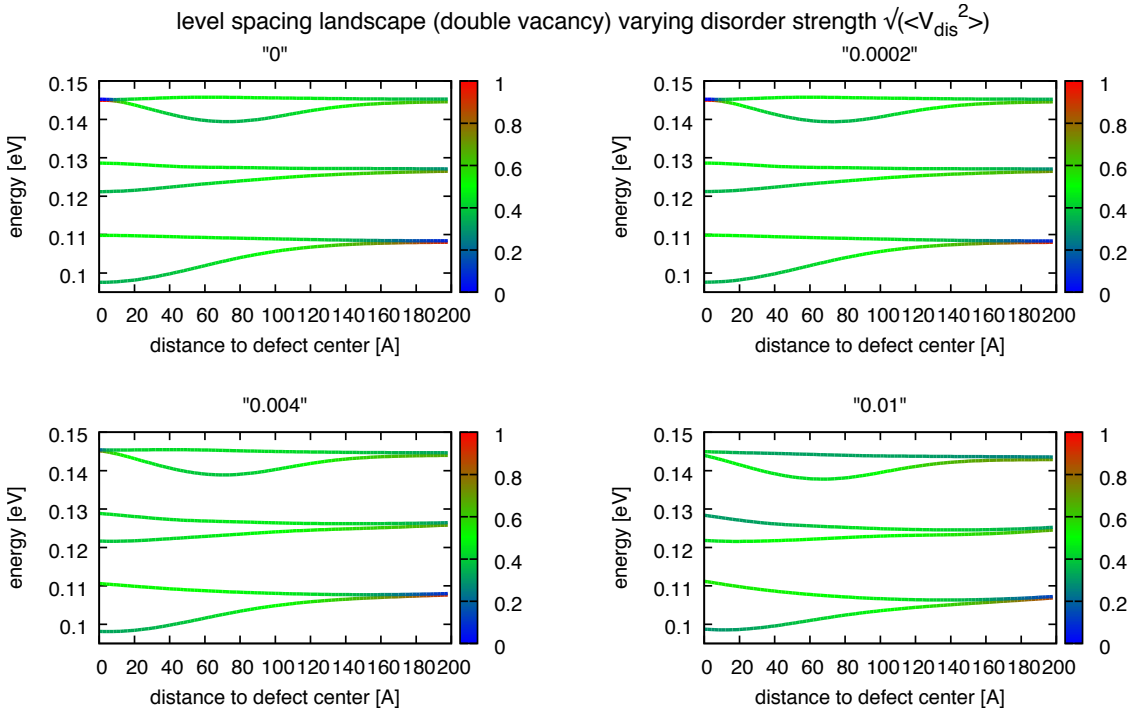

Figure 3.29.: Level spacing of the six lowest QDOT eigenstates depending on the relative distance of QDOT and defect center in x direction for various amplitudes of the disorder potential **top left)** $\sqrt{\langle V_{dis}^2 \rangle} = 0$meV, **top right)** $\sqrt{\langle V_{dis}^2 \rangle} = 0.2$meV, **bottom left)** $\sqrt{\langle V_{dis}^2 \rangle} = 4$meV, **bottom right)** $\sqrt{\langle V_{dis}^2 \rangle} = 10$meV. Color coding represents the "K-projection" (see detailed explanation in the beginning of this section) onto the corresponding QDOT state of pristine graphene ($|\langle \Psi_{\text{defect}} | \Psi_{\text{pristine}} \rangle|^2$)

Since we established that the prominent mixing property of the double vacancy defect in x direction is resilient to various amplitudes of disorder we now want to determine whether the pronounced avoided crossings of the flower defect are less stable with respect to correlated disorder. At first glance (Fig. 3.30) we again see merely locally shifted QDOT levels. Closer inspection however reveals that while still present, the avoided crossings have also been shifted horizontally.

This is a direct consequence of the QDOT state preferably populating the disorder valleys which simply deforms it and causes the defect site to pass through high density regions somewhat sooner (or possibly later for a different disorder potential).

Similar to the double defect we see very robust wavefunction character (color scale in Fig. 3.31). This time however the pristine character of level five and six (for QDOT-defect distance zero) remains unchanged even for a disorder potential of up to 10meV.

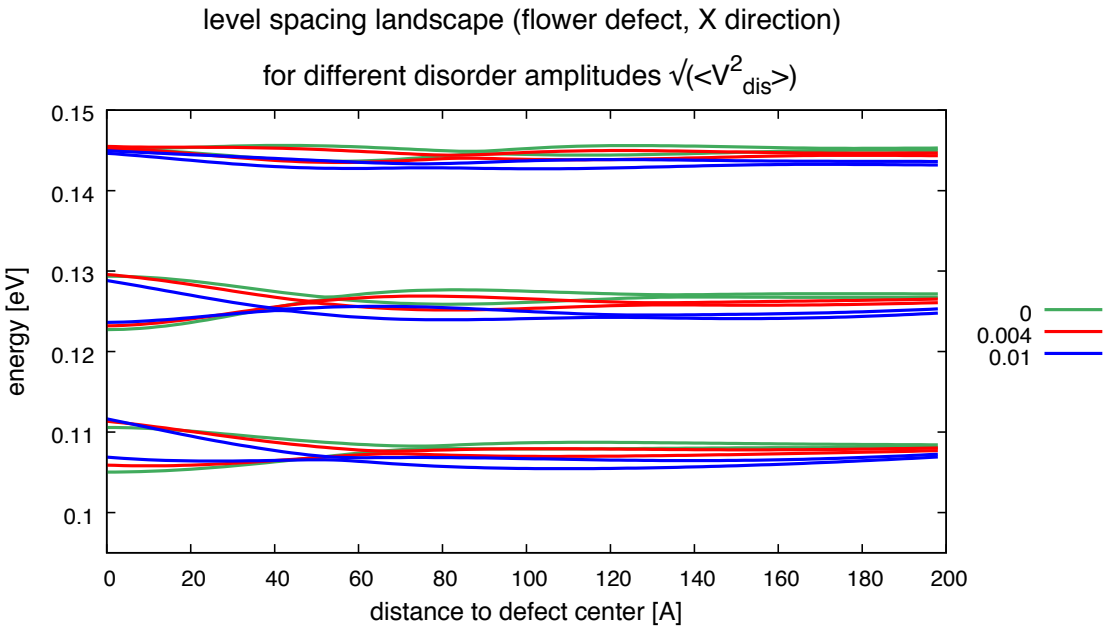

Figure 3.30.: Level spacing landscape of the flower defect for varying disorder potential amplitude of 0 eV (green), 4 meV (red) and 10 meV (blue), ($l_{\text{corr}} = 8.8nm$ fixed).

Next we investigate the influence of varying the correlation length l_{corr} of the disorder potential, that is its characteristic length scale (see right column of Fig. 3.27). While it is quite apparent that correlation lengths roughly the size of our QDOT (FWHM $\approx$ 20nm) will only result in global shifts of our energy levels without affecting the level splittings (see Fig. 3.33 top left), shorter correlation lengths lead to different results. Since we are in the Landau regime ($|\vec{B}| \approx 7$T), a second very important length scale for our system is given by the magnetic length (3.4).

$$l_B \approx \frac{25\text{nm}}{\sqrt{B}} \quad \rightarrow \quad 9.4\text{nm} \tag{3.4}$$

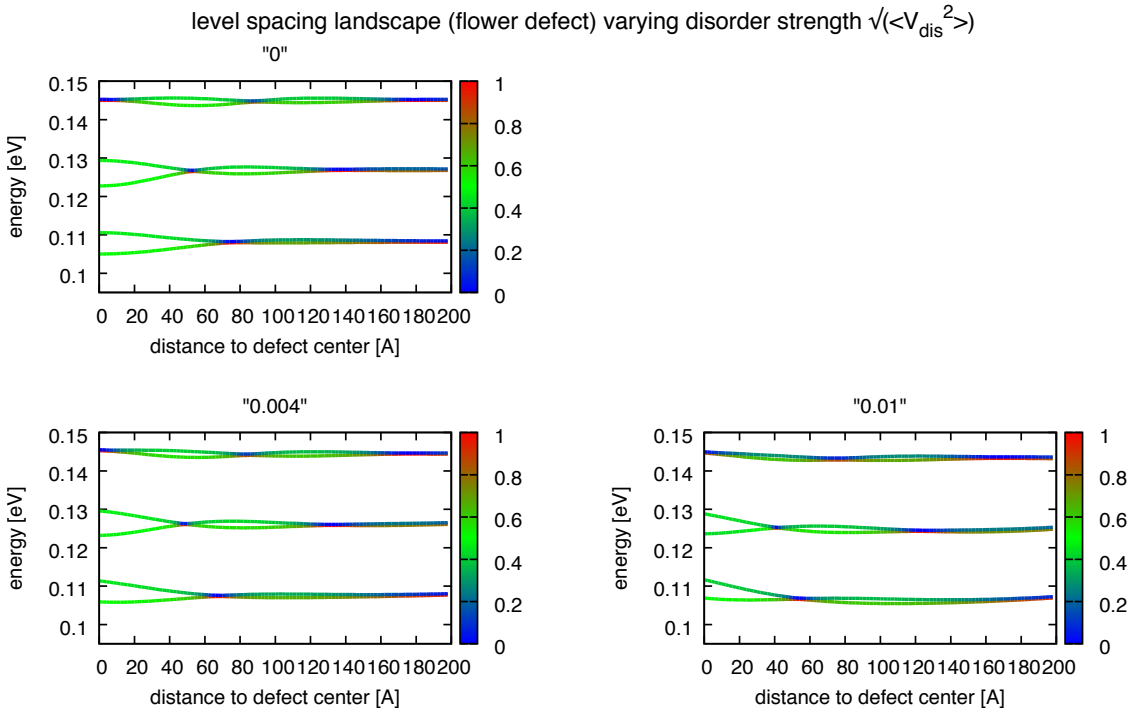

Figure 3.31.: Level spacing of the six lowest QDOT eigenstates depending on the relative distance of QDOT and defect center in x direction for various amplitudes of the disorder potential **top left)** $\sqrt{\langle V_{dis}^2 \rangle} = 0$meV, **bottom left)** $\sqrt{\langle V_{dis}^2 \rangle} = 4$meV, **bottom right)** $\sqrt{\langle V_{dis}^2 \rangle} = 10$meV. Color coding represents the "K-projection" (see detailed explanation in the beginning of this section) onto the corresponding QDOT state of pristine graphene ($|\langle \Psi_{\text{defect}} | \Psi_{\text{pristine}} \rangle|^2$).

Our largest investigated l_{corr} of 15nm, which is somewhat larger than the magnetic length l_B while still below the QDOT size, leads to almost no changes in the valley splittings (top left in Fig. 3.33) and results in an almost homogeneous shift of the levels for most positions. The nature of the states is slightly affected with levels five and six again no longer pristine. Since those states have virtually no density at their origin (without disorder) they can not know that there is a double vacancy present. Introducing disorder — and with it local puddles of density that fill its "potential dips" — allows for finite density at the origin which almost immediately causes these states to rotate within their sub space (loosing the pristine character → green color scale) because they are now aware of the vacancy.

The slight tendency of level three towards blue color scaling is merely an artifact of the specific disorder generated. Since the correlation length under consideration is now about the same size as the relevant features of the QDOT states, enhancing or suppressing their characteristic shapes via the disorder is, while chosen purely random, very plausible.

Reducing l_{corr} to 9nm, which is close to the magnetic length l_b of our system, we find slightly more variation of the position dependent level spacing since the disorder now varies on a smaller scale. While the pristine character of states five and six at position zero is again vacant we no longer see the somewhat blue hue of state three, which shows that this feature was indeed (most likely) specific to the previously used disorder realization.

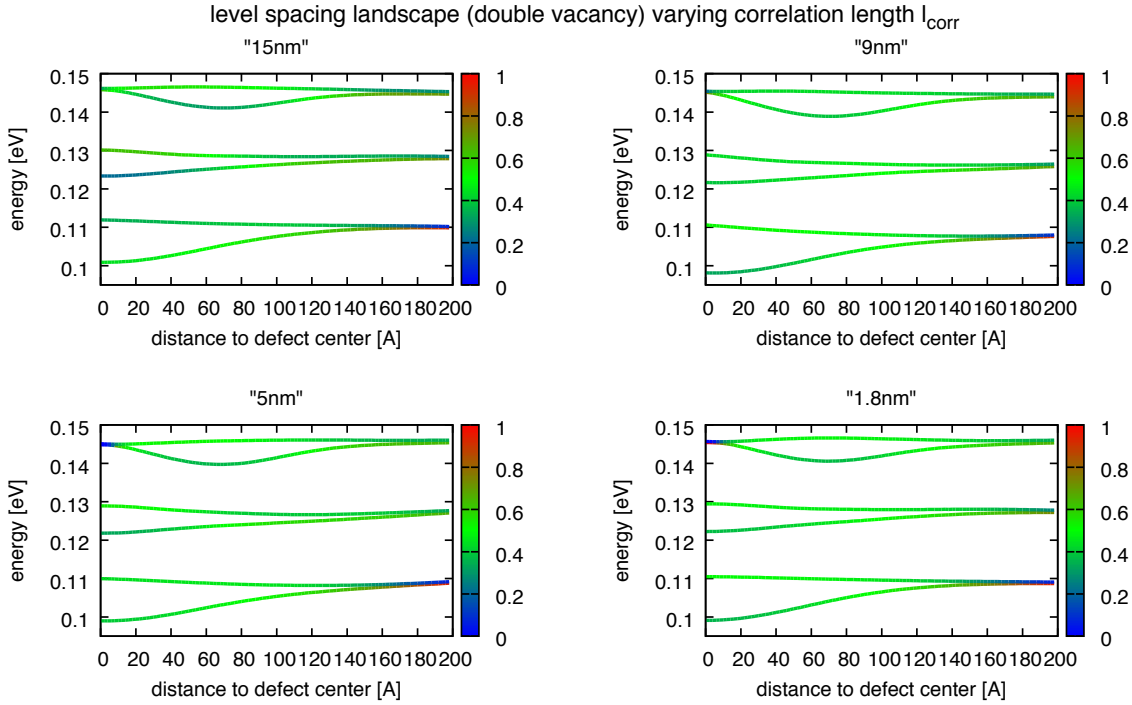

Figure 3.32.: Level spacing of the six lowest QDOT eigenstates depending on the relative distance of QDOT and defect center in x direction for various correlation lengths l_{corr} of the disorder potential **top left)** l_{corr} = 15nm, **bottom left)** l_{corr} = 9nm, **bottom left)** l_{corr} = 5nm, **bottom right)** l_{corr} = 1.8nm. Color coding represents the "K-projection" (see detailed explanation in the beginning of this section) onto the corresponding QDOT state of pristine graphene ($|\langle \Psi_{\text{defect}} | \Psi_{\text{pristine}} \rangle|^2$).

Going further and reducing l_{corr} well below the magnetic length ($l_B \approx 9.4$nm) to 5nm and even 1.8nm (bottom plots of Fig. 3.32 and 3.33) reveals a very general but still interesting property of our system. If the disorder varies on a length scale much smaller than the magnetic length, our quantum mechanical wavefunctions effectively average it away (since we implement symmetric disorder, $\langle V_{\text{dis}} \rangle = 0$).

Our system is thus inherently incapable of resolving the short scale variations of the potential energy and behaves almost as though no disorder was present. The changes in level spacing, while still present, are (especially for $l_{\mathrm{corr}} = 1.8\mathrm{nm}$) reminiscent of the almost global shifts of $l_{\mathrm{corr}} = 15\mathrm{nm}$ (averaging effect). We even recover the pristine character of states five and six (bottom right of Fig. 3.32).

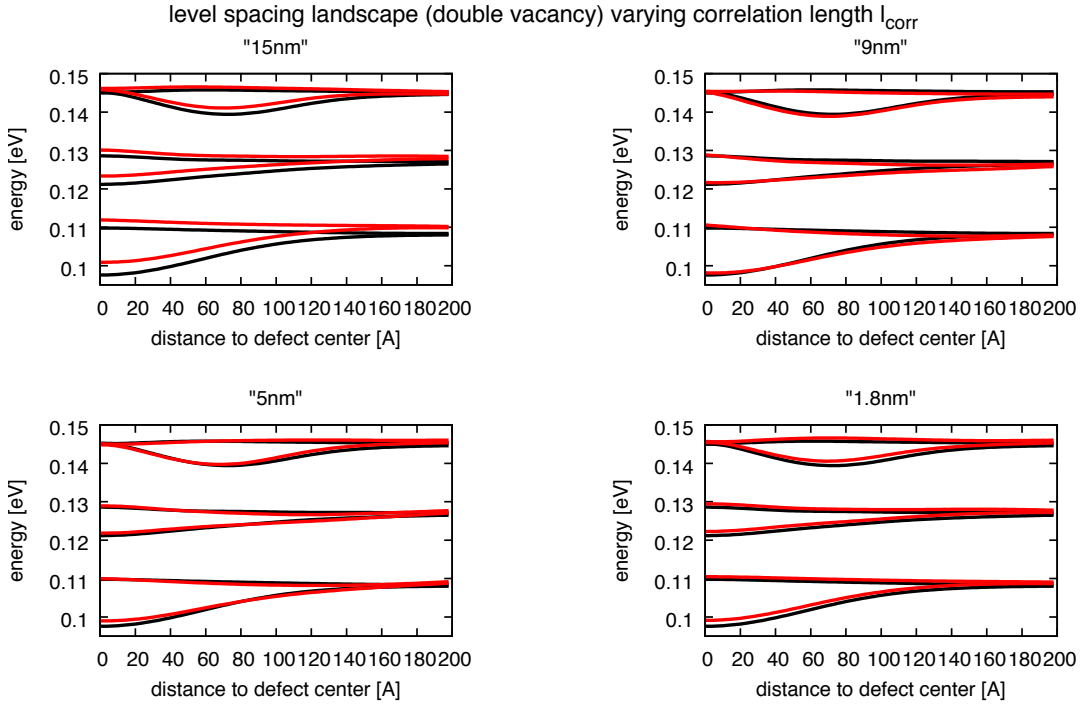

Figure 3.33.: Level spacing landscape of the double vacancy defect for varying disorder potential correlation lengths of **top left)** $l_{corr} = 15\mathrm{nm}$, **bottom left)** $l_{corr} = 9\mathrm{nm}$, **bottom leftt)** $l_{corr} = 5\mathrm{nm}$, **bottom right)** $l_{corr} = 1.8\mathrm{nm}$. $\sqrt{\langle V_{dis}^2 \rangle} = 4\mathrm{meV}$ fixed.

We conclude that both orbital Δ_j^O and valley Δ_j^k splittings as functions of QDOT-defect distance are very robust against both long- and short-range disorder of various amplitudes. Experimental realization of our calculations should thus, at least in principle, not fail due to substrate induced disorder.

3.3. Transition dynamics

3.3.1. Landau Zener Formalism

Once we have deduced the QDOT orbitals of our QDOT-defect system for a set of relative distances between QDOT and defect center we will have acquired cuts through a set of two dimensional energy surfaces. With the value for each distance coming from independent eigenvalue calculations this represents the "static" energy surface and is thus in principle identical to an infinitely slow dynamical probing of this energy landscape.

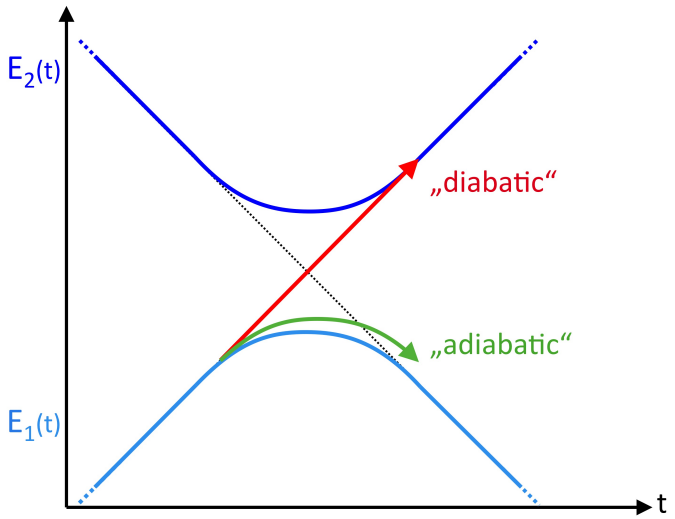

Figure 3.34.: Typical avoided level crossing of a two level quantum system. The red and green arrow represent the two possible transitions when propagating a prepared state "past" the crossing.

The next step will be to investigate transition dynamics in our system. Theoretically we can imagine moving the STM tip in the x,y-plane and thus move our QDOT with a certain velocity $\vec{v}$ towards, from or around any present defect along a trajectory of our choosing. Experimental realization of such a thought experiment will inevitably have to rely on an array of electrical gates that create and move our QDOT potential since an STM tip will be restricted to very slow movement. One interesting phenomenon occurs at an avoided level crossing.

Granted that our orbital splitting Δ_j^O is large enough — compared to the valley splitting Δ_j^k — we can treat the system as an effective two level system with a time dependent Hamiltonian. The stereotypical textbook form of such an avoided level crossing in a two-level system ($|\downarrow\rangle$, $|\uparrow\rangle$) can be seen in Fig. 3.34.

The Hamiltonian that describes this system can be written as:

$$H(t) = \frac{1}{2}\begin{bmatrix} \alpha t & \Delta_{12} \\ \Delta_{12} & -\alpha t \end{bmatrix} \tag{3.5}$$

Starting at the lower of the two states, $|\downarrow\rangle$, at a time far left of the crossing we would now like to investigate how this state propagates "past" the crossing. In principle only two possible scenarios can happen (see Fig. 3.34):

I) "adiabatic propagation"
(the system remains on the initial energy level)

II) "diabatic transition"
(the system transitions onto the other energy level)

Landau Zener theory [19, 20] provides a formalism to calculate the probability of these events. A very short derivation is given in the following. Plugging the ansatz $|\Psi(t)\rangle \coloneqq a_1(t)\,|\uparrow\rangle + a_2(t)\,|\downarrow\rangle$ into the time dependent Schrödinger equation using the Hamiltonian in (3.5) gives two coupled equations for the coefficients $a_1(t)$ and $a_2(t)$:

$$\dot{a}_1(t) = -\frac{i\alpha t}{2}a_1(t) - \frac{i\Delta_{12}}{2}a_2(t) \tag{3.6}$$

$$\dot{a}_2(t) = \frac{i\alpha t}{2}a_1(t) - \frac{i\Delta_{12}}{2}a_1(t) \tag{3.7}$$

As we aim to find an expression for $(\frac{\dot{a}_1}{a_1})$ in the limit of large t, simply decoupling the above equations yields a single equation that solely contains $a_1(t)$.

$$\ddot{a}_1(t) = -\Big\{\frac{i\alpha}{2} + \frac{\Delta_{12}^2}{4} + \frac{\alpha^2 t^2}{4}\Big\}a_1(t) \tag{3.8}$$

At $t \to \infty$, a_1 should display constant modulus with the only time dependence given by a complex phase. Using $a_1(t) \coloneqq |a_1|e^{i\phi(t)}$ gives:

$$\Big\{-i\ddot{\phi}(t) - \dot{\phi}^2(t) + \frac{i\alpha}{2} + \frac{\Delta_{12}^2}{4} + \frac{\alpha^2 t^2}{4}\Big\}a_1(t) = 0 \tag{3.9}$$

Separating this equation into real and imaginary parts we find the real part to give:

$$\dot{\phi}(t) = \pm\frac{1}{2}\sqrt{\Delta_{12}^2 + \alpha^2 t^2} \underbrace{\approx}_{t\to\pm\infty} \frac{\alpha t}{2}\Big(1 + \frac{\Delta_{12}^2}{2\alpha^2 t^2}\Big) \tag{3.10}$$

It is now a common trick to assume that $(\frac{\dot{a}_1}{a_1}) = -i\dot{\phi}$ is well defined when expanded onto the complex plane, thus allowing one to circumvent the exact solution of $a_1(t)$ when deriving the Landau Zener formula.

Now we can identify the real integration with one along an infinite half circle $\hat{hc}$ ($z := Re^{i\theta}$):

$$\int_{-\infty}^{\infty} \frac{\dot{a}_1}{a_1} dt = -\int_{\hat{hc}} \frac{\dot{a}_1}{a_1}(z) dz \tag{3.11}$$

$$ln\Big(\frac{a_1(\infty)}{a_1(-\infty)}\Big) = i \lim_{R\to\infty} \int_0^{\pm\pi} \Big(\frac{i\alpha R^2 e^{2i\theta}}{2} + \frac{i\Delta_{12}^2}{4\alpha}\Big) d\theta \tag{3.12}$$

$$ln\Big(\frac{a_1(\infty)}{a_1(-\infty)}\Big) = \mp\frac{\pi\Delta_{12}^2}{4\alpha} \tag{3.13}$$

With this we have found a relation between $a_1(-\infty)$ and $a_1(\infty)$. For obvious normalization reasons the physically meaningful sign in (3.13) is the negative one. Assuming we begin with $|a_1(-\infty)|^2 = 1$ we can now write the diabatic transition probability P_{LZ} as:

$$P_{LZ} = e^{-\frac{\pi\Delta_{12}^2}{2\alpha}} \tag{3.14}$$

3.3.2. Controlling the adiabatic/diabatic transition

Having successfully calculated the static "energy landscape" of an edgeless QDOT in the vicinity of various defect types we would now like to investigate the dynamic properties of such a system. By that we mean propagating an initial state with a time dependent Hamiltonian that incorporates a QDOT potential (from the STM tip) which moves across the graphene flake at various speeds. In regions where the valley splitting of our defects is small compared to the orbital splitting of our QDOT we may argue to view it (albeit in a rather crude approximation) as a two level system. Features of particular interest are avoided crossings that allow for numerically studying simple transition dynamics and (given the two level approximation) comparing to analytical predictions of Landau Zener theory.

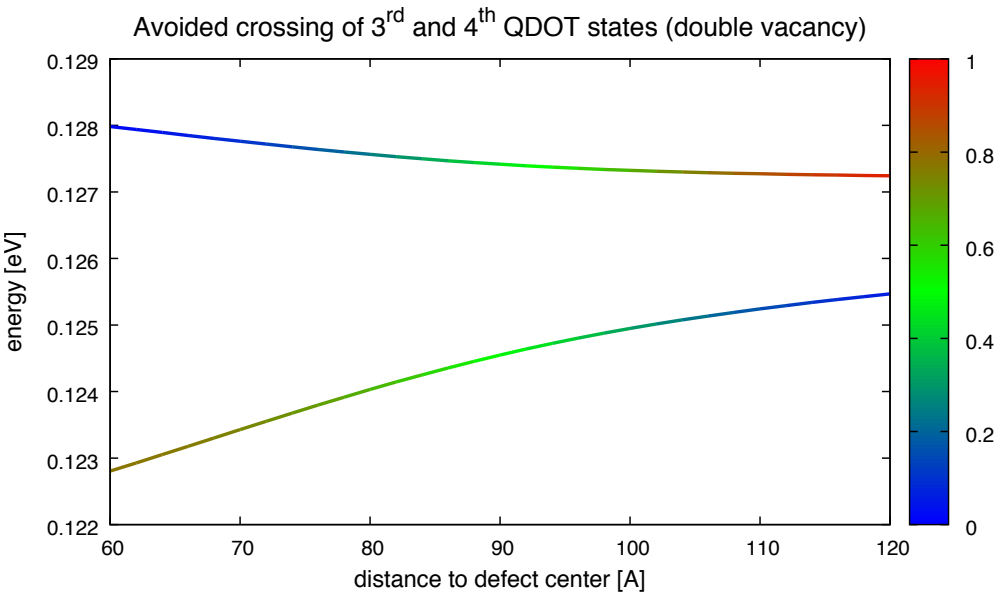

Figure 3.35.: Zoom in of the y direction energy landscape for the double defect. Close up view of the avoided crossing between 3^{rd} and 4^{th} QDOT state used for studying transition dynamics.

Let us focus on the barely recognizable avoided crossing of the double defect system visible at a QDOT shift of about 90Å in $-y$ direction. That this is indeed an avoided crossing between the 3^{rd} and 4^{th} QDOT state becomes clear through the color coding in Fig. 3.35. What we would like to achieve is passing "over" this particular crossing by starting with a "pure" 3^{rd} QDOT state some distance away from it (taken from the static calculations), propagating that very state with a time dependent QDOT potential that moves past the crossing at different speeds and then check the composition of our final state by projecting onto the static 3^{rd} and 4^{th} QDOT state.

According to Landau Zener theory we should find adiabatic behaviour for slow speeds and an increasing probability for an adiabatic transition at higher speeds. To elucidate this proposition we have to slightly adapt (3.14) for our scenario. We substitute the temporal derivative by $\frac{\partial(E_4-E_3)}{\partial t} \approx \frac{\partial y}{\partial t}\frac{\partial(E_4-E_3)}{\partial y} = v\partial_y(E_4-E_3)$ and obtain:

$$P_{LZ} = e^{-\frac{2\pi\Delta_{34}^2}{\hbar v \partial_y (E_4(y)-E_3(y))}} \tag{3.15}$$

A closer look at our avoided crossing (Fig. 3.35) allows us to estimate Δ_{34} ($\approx 5.6076 \cdot 10^{-22}$J) as half the level separation at the crossing and the average slope of the level separation $\partial_y(E_4 - E_3)$ ($\approx 2.0561 \cdot 10^{-12}$J/m). Those parameters are all thats necessary to plot the expected diabatic transition probability (3.15) as a function of v (blue line in Fig. 3.41). The application of Landau Zener theory to our crossing might not be fully appropriate because:

- Starting with one of the initially calculated "static" states we will have to smoothly and slowly accelerate ((3.16), see Fig. 3.36) our QDOT potential (3.17) to minimize the leakage of probability into other eigenstates of the system:

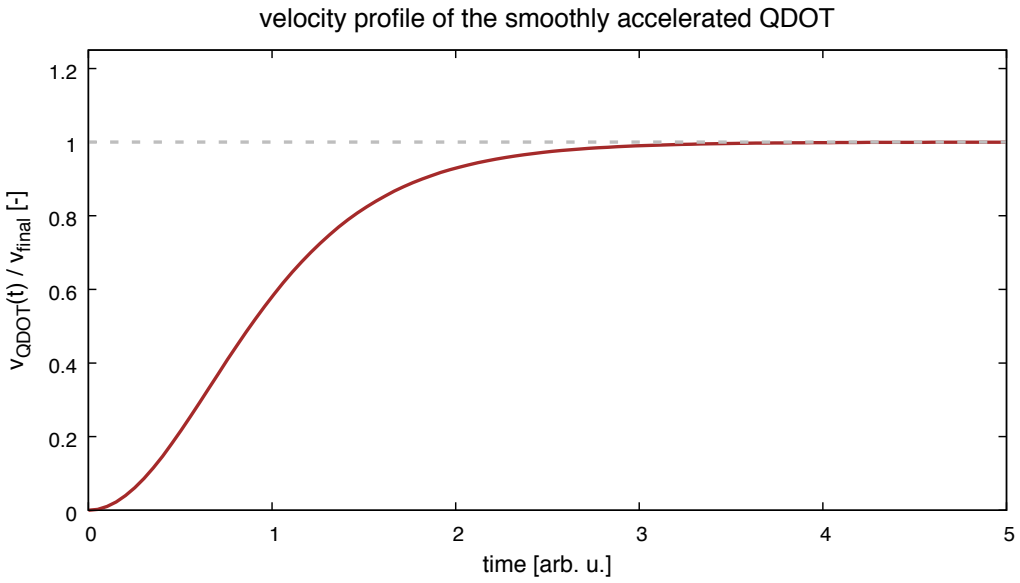

Figure 3.36.: Velocity profile (3.16) used for smoothly accelerating our initial QDOT state via a time dependent potential. Parameter a in (3.16) allows for tuning of the acceleration in response to the starting distance available for each calculation.

$$v(t) := \left(1 - \frac{1}{e^{a\cdot t}+1}\right)^2 \tag{3.16}$$

$$V_{STM}(x,y,t) \quad \rightarrow \quad V_{STM}(\vec{r}-\vec{r_0}(t)) \qquad \text{with} \qquad \vec{r_0}(t)=\vec{r}_0+\vec{v}(t) \qquad (3.17)$$

- We will only be able to propagate a state over some limited distance with the crossing somewhere in the middle (P_{LZ} only assumes a single crossing and gives probabilities for asymptotic limits).

- Keeping the acceleration as low as possible while ensuring that the region of the avoided crossing is traversed with some nearly constant final velocity will require a long enough run-up distance. Getting the QDOT up to speed is often limited by trying not to pass another avoided crossing when accelerating towards the chosen avoided crossing.

- In contrast to our static calculations of the previous chapter the newly developed time propagation code did (at the time of calculation) only feature hermitian Hamiltonians, limiting us to hard boundaries. Given the size of the QDOT, once the crossing was traversed we were most likely in a region of the flake were reflection at these hard walls also deteriorates the validity of our projection procedure.

- Using a very recently written time propagation code (by T. Jawecki and T. Fabian based on [32]) that is not yet fully parallelized we are somewhat limited in total simulation time. The choice of avoided crossing (double defect, $y_{shift} = -90$Å, 3^{rd} and 4^{th} level) turned out to be the only one where both diabatic and adiabatic behaviour could be observed. If the crossing is too narrow, the low speeds necessary for adiabaticity are computationally out of reach whereas if the crossing is too large we lack enough runway to smoothly get our QDOT up to the necessary speed for a diabatic transition to occur (without interplaying with a neighbouring crossing).

- We reuse our static QDOT states investigated in the previous chapter to project our dynamically propagated state onto and thus identify its change of "character" during propagation. Fig. 3.37 illuminates the kind of error introduced in this process. While the strength of our STM potential is varied for the identification of our level separation in the "static case", time propagation sees our STM potential move along a given trajectory without changing its magnitude. This means that instead of projecting on the static states marked by the red crosses (Fig. 3.37) we should rather project onto the states indicated by the green crosses (Fig. 3.37). Contrary to initial expectations the red cross states (Fig. 3.37) work remarkably well too, which can be explained by the state itself being less sensitive to the magnitude of the potential. Projecting the red cross states onto each other reveals that they are almost perfectly orthogonal. We thus conclude that the use of our red cross states as the "static states" constitutes valid approximation.

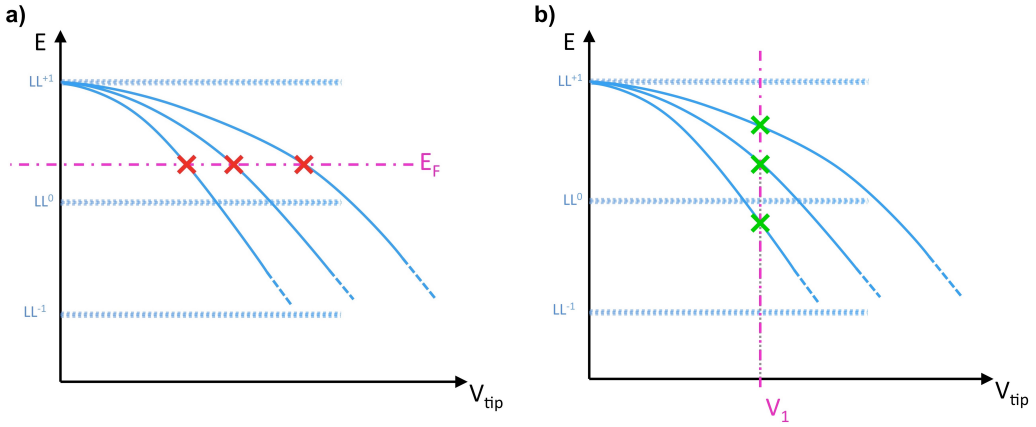

Figure 3.37.: Schematic illustration of different methods for identifying QDOT states. **a)** red crosses mark states calculated for identifying the level separation of the QDOT. **b)** green crosses representing eigenstates of the QDOT at a given constant magnitude of the STM tip potential.

We now propagate our QDOT over the avoided crossing with different speeds (Fig. 3.39). We can clearly see that while always starting with the same initial state we end up with fairly different results once the crossing (at $y \approx 90$Å has effectively been passed. As we previously assessed, the 3^{rd} QDOT state is one that is very localized on the defect. We find that the diabatic transition (large velocity, right column in Fig. 3.39) taking place can be recognized by comparing the degree of localization at the defect site for the initial and final states.

Another interesting aspect of this propagation (one that is quite hard to visualize without a video) is that depending on the speed of motion the QDOT does not move along a straight path but begins to slightly wobble from left to right for increasing velocities. We know from previous work that the honeycomb lattice of graphene makes for some "preferred directions" (Fig. 3.38) which often manifest themselves in either six or threefold patterns when investigating scattering wavefunctions or (as in the previous chapter) eigenstates of lattice defects. We thus propose that the wiggling motion of our defect is due to the wavefunction "trying" to follow these "preferred directions" while repeatedly being reflected by the QDOT well.

With increasing speed the wavefunction gains more momentum and is thus able to penetrate the QDOT potential further, causing a more pronounced wiggling motion to occur (see Fig. 3.39).

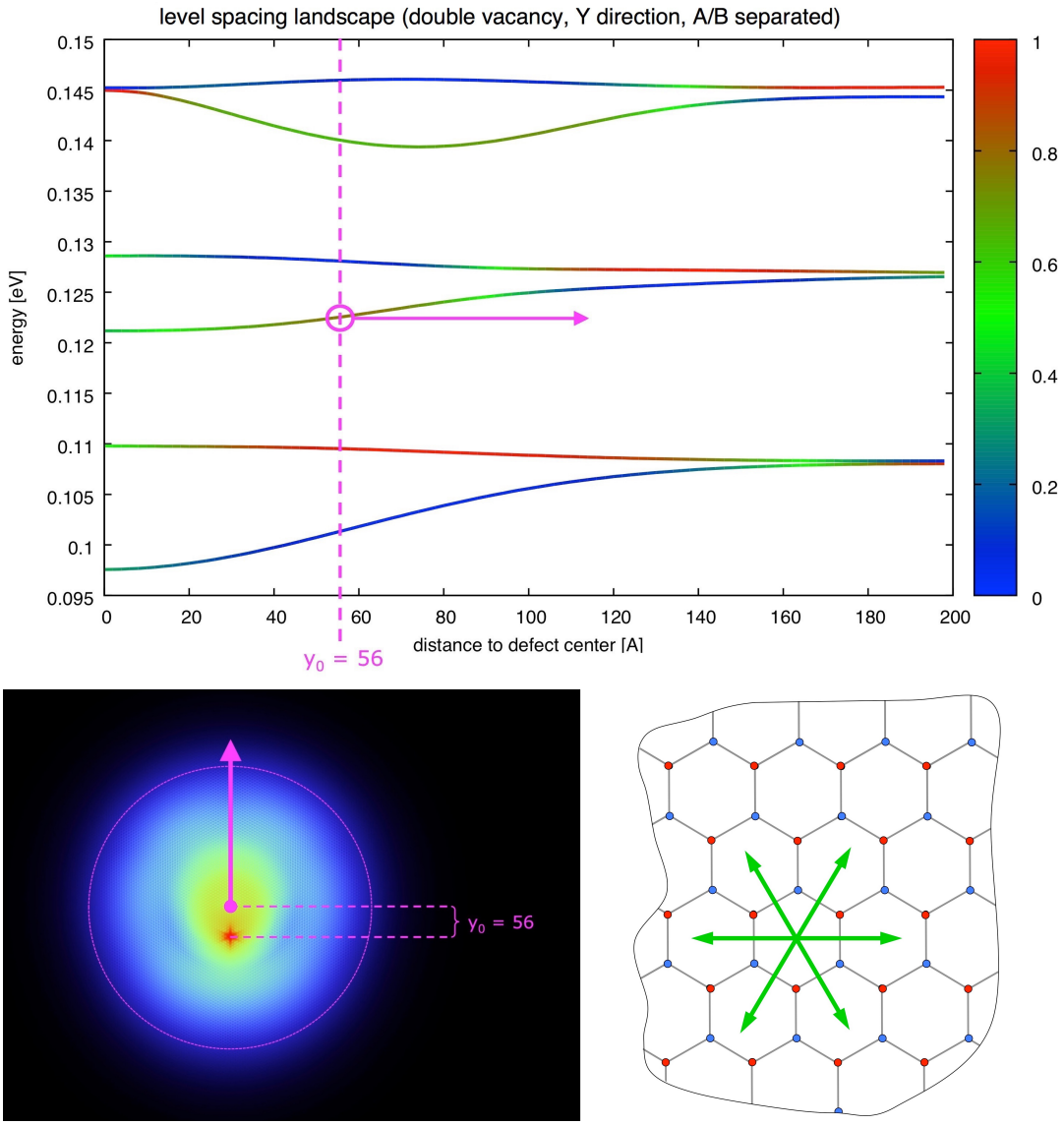

Figure 3.38.: **top)** Energy landscape for the double defect in -y direction with the initial QDOT-defect distance marked by the dashed pink line. Solid pink circle and arrow highlight the starting point and the direction of motion for our time propagation respectively. **bottom left)** Electron density of the initial 3^{rd} QDOT state with pink arrow pointing in the direction of motion and initial offset (in Å) highlighted. **bottom right)** Schematic depiction of the graphene lattice with sublattices in red and blue and green arrows highlighting the "preferred directions" of the QDOT.

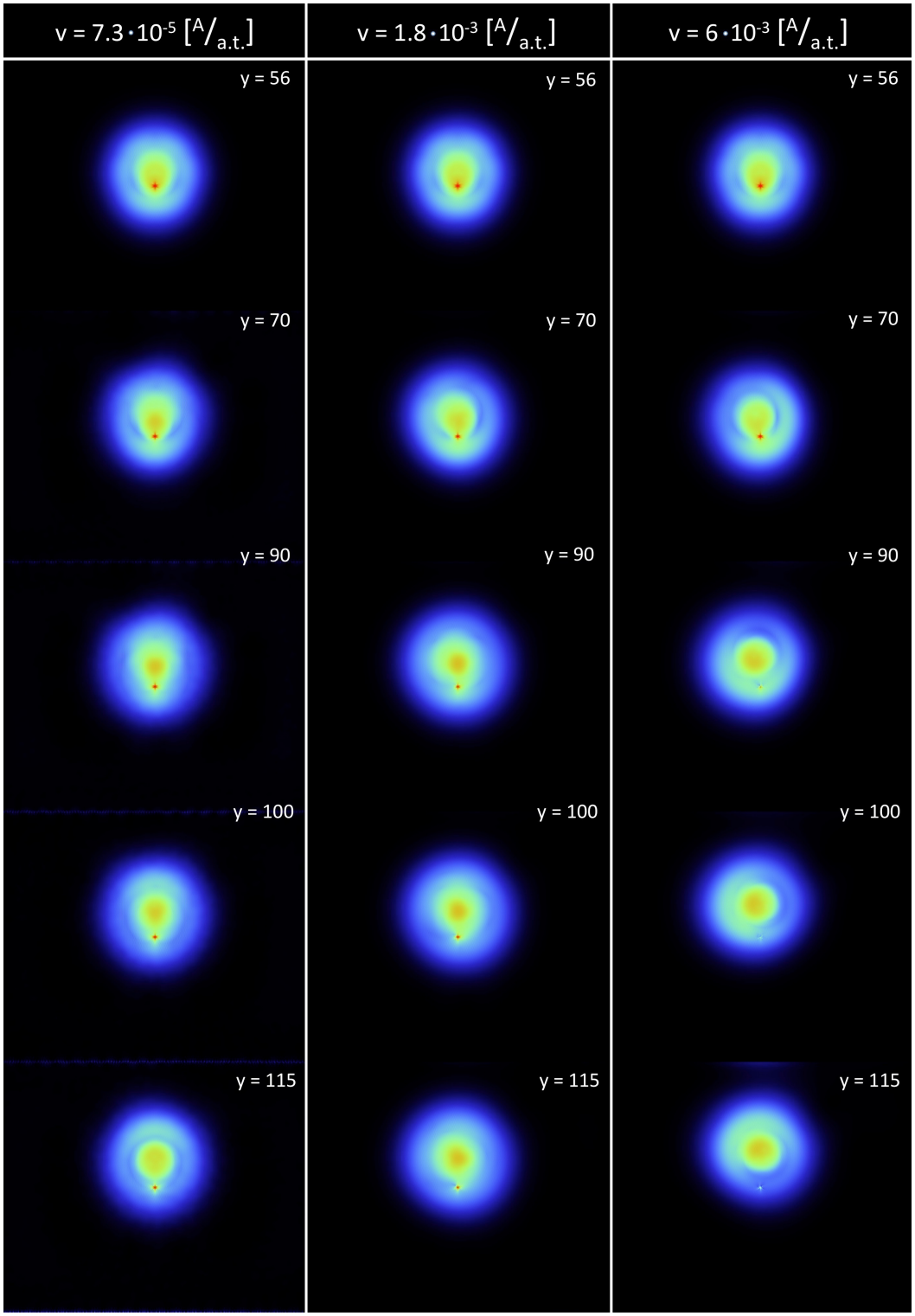

Figure 3.39.: Electron density of the initial QDOT state propagated with three different velocities (columns). Time increases from top to bottom resulting in five "snapshots" at comparable positions (given in Å) for each of the velocities (rows). The wiggling motion encountered at high speeds is reflected in the lack of mirror symmetry with respect to the vertical axis at the rightmost column.

In order to get a numerical estimate for the diabatic transition probability we proceed to calculate the squared overlap of the dynamically propagated wavefunction and the static states obtained in the previous chapter, $\langle$"dyn"|"stat"$\rangle$. For the 3^{rd} and 4^{th} static state ("S3", "S4") we obtain results plotted in Fig. 3.40. Given that our avoided crossing is not very isolated from its neighbouring crossings and our limited starting distance for getting the QDOT up to speed we find excellent agreement with Landau Zener theory. Increasing the traversing speed clearly promotes the likelihood for diabatic change.

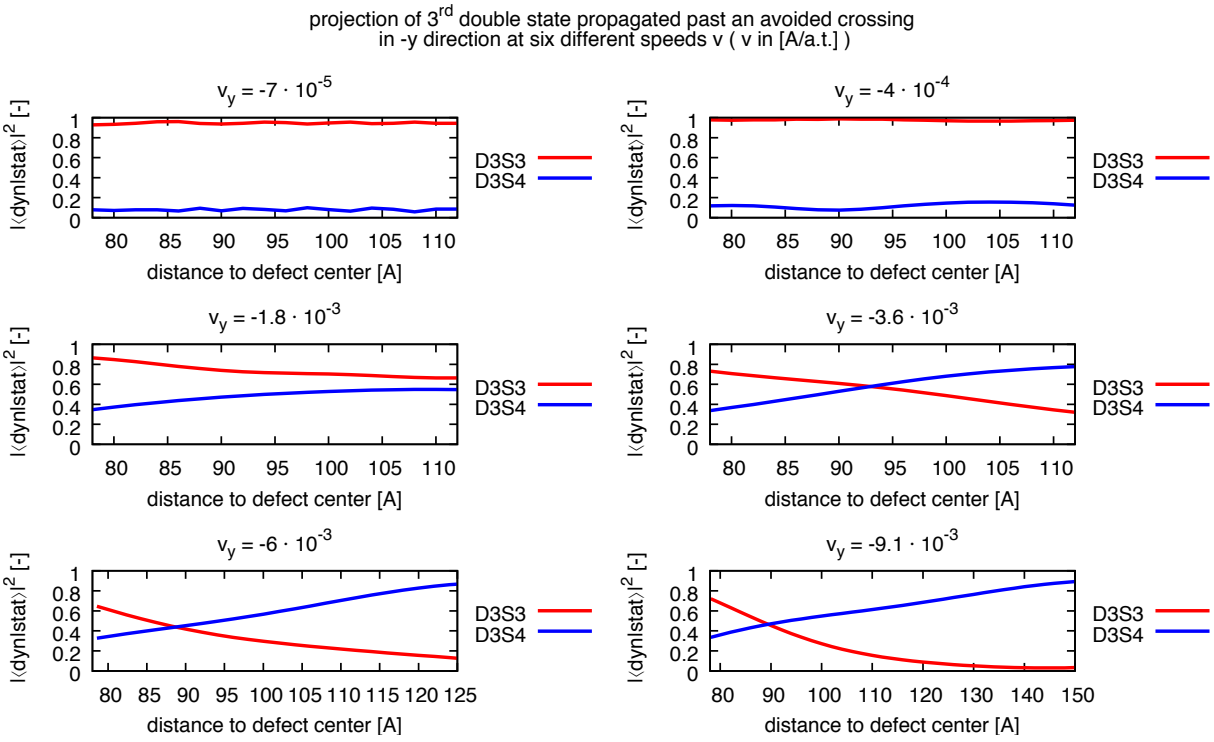

Figure 3.40.: Projection of an initial state dynamically propagated past an avoided crossing at a defect distance of about 90 (x-axis) (initially 3^{rd} QDOT state with double defect present) onto the 3^{rd} (red) and 4^{th} (blue) static QDOT states at the respective position in time. The six subplots correspond to different speeds of QDOT motion.

If we take the value of the blue lines in Fig. 3.40, that is the diabatic projection projection $|\langle D3|S4\rangle|^2$, once its value seems to have converged we have an estimate of the diabatic transition probability. Fig 3.41 compares our numeric values (green crosses) with the prediction of Landau Zener theory. We appear to have made quite a lucky guess for estimating the slope parameter of our crossing as the agreement seems almost too good given all the approximations involved.

While there is indeed some wiggle room to estimate the slopes of pathological avoided crossings such as ours we find that the form of the Landau Zener probability deviates from our simulation results (Fig. 3.41). This is most likely due to the fact that the wiggling motion of our QDOT becomes more pronounced with increasing speeds (thus artificially altering the projection value).

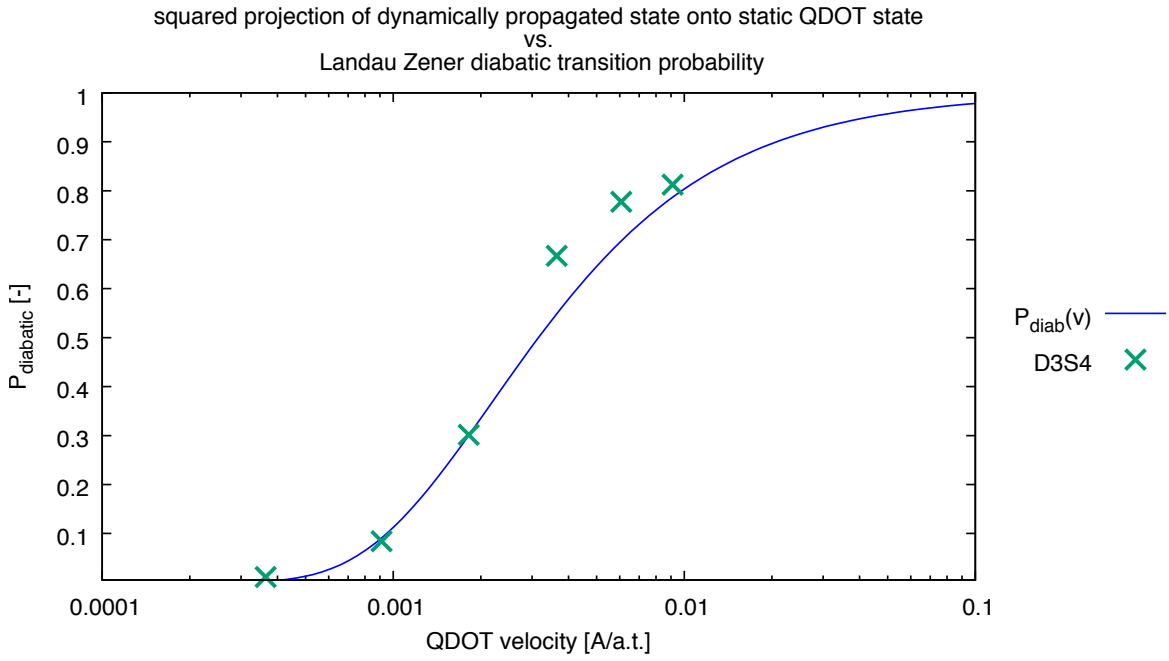

Figure 3.41.: Comparison of the diabatic transition probability as a function of traversing speed, **(green crosses)** calculated from the projection data acquired in the time propagation (rightmost value of the blue lines in the previous figure, Fig. 3.5), **(blue line)** represents the Landau Zener diabatic transition probability $P_{LZ}(v) = e^{-\frac{2\pi\Delta_{34}^2}{\hbar v \partial E_{34}}}$ with parameters for level splitting and average slope estimated for this particular avoided crossing (double defect, QDOT shifted in $-y$ direction about 90Å).

Regardless of the above mentioned error sources which undoubtedly leave vast room for improvement we were able to investigate the dependence of the diabatic transition probability on the traversing speed of our QDOT potential and qualitatively reproduce the results of Landau Zener theory.

3.4. Defect-defect interaction

Motivated by our tedious search for a suitable avoided crossing for our transition dynamics investigation we would now like to try and specifically tailor a level spacing landscape by combining several defects at chosen distances from each other. Since the number of possible parameters seemingly explodes with the added degrees of freedom (x, y distance) for every added defect we will focus on two vertically stacked double vacancies. We do so since the pronounced directionality of this defect indicates possibly rich effects while only combining two defects.

The limitations of such a defect array description are manyfold. Similar to embedding single defects we have to keep in mind that our DFT description with a periodic supercell will most likely include defect-defect interactions with its periodic images if our super cell is not sufficiently large. While one might think that embedding two defects in some vicinity of each other could benefit from these shortcomings, such an assumption can only hold for two identical defects positioned akin to the periodicity of our super cell description. Using a number of different defects in some complex arrangement will inevitably suffer from multiple such description errors.

3.4.1. Two double-vacancies vertically stacked

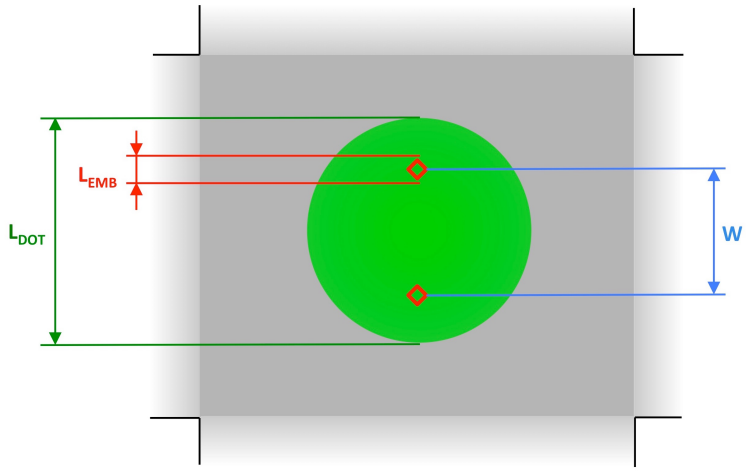

Figure 3.42.: Schematic depiction of the system under consideration. Graphene flake as a grey rectangle with open boundary conditions on all four sides indicated via black lines and fading grey colour. Embedding sites of the two defects indicated by red markers. Vertical defect distance marked as W.

Since for the time being we restrict ourselves to two identical double vacancy defects stacked exactly vertically (y direction) with distances W of 17.5nm and 22.5nm (see Fig. 3.42), we omit detailed investigation of the proximity limits of our description. Due to the fact that the defect size (L_{EMB} in Fig. 3.42) and the QDOT size (L_{DOT} in Fig. 3.42) differ by about an order of magnitude we can place the two defects at a distance W at which they can essentially be viewed as two separately embedded defects.

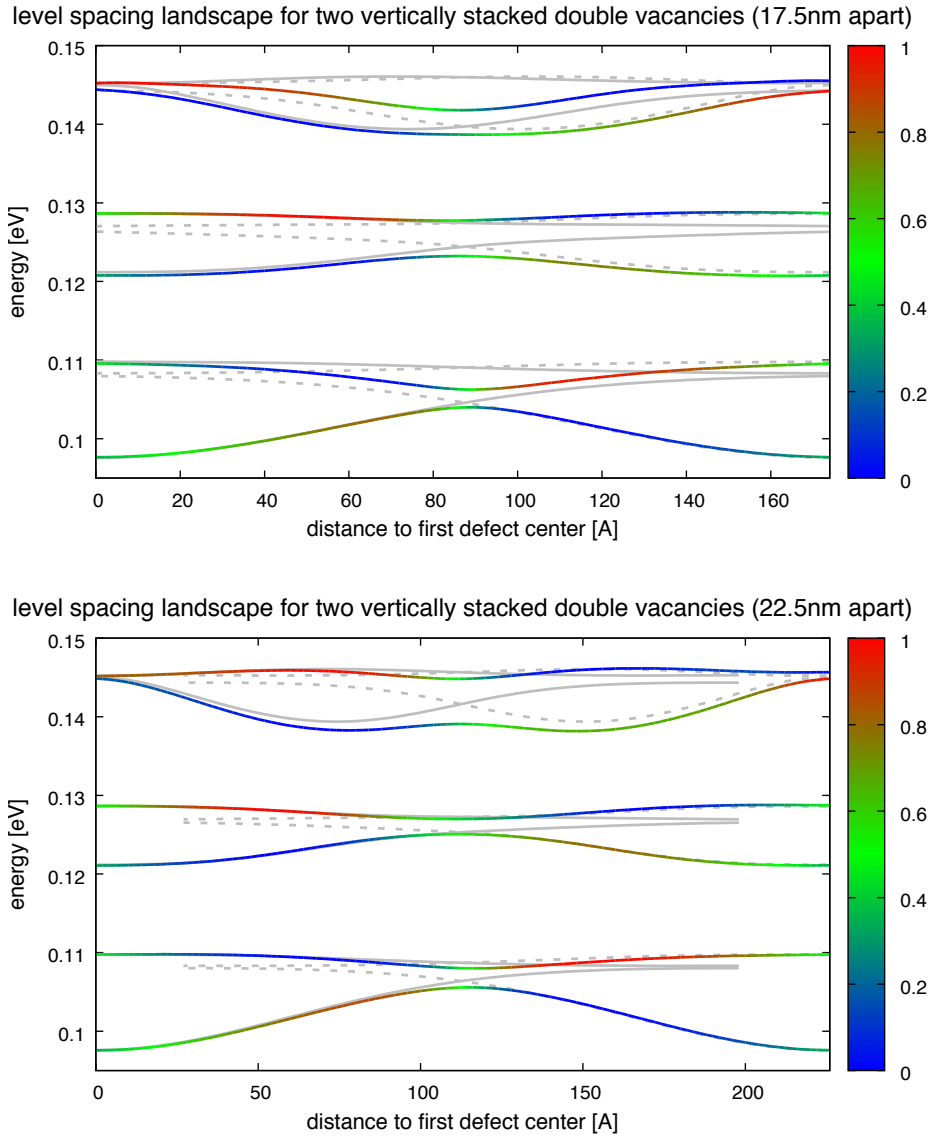

Figure 3.43.: Level spacing of the six lowest QDOT eigenstates depending on the relative distance of QDOT and defect center for the cases of a single defect embedded (grey / grey dashed) and two double vacancy defects embedded with the color scale representing $|\langle \Psi_{\mathrm{defect}} | \Psi_{\mathrm{pristine}} \rangle|^2$. The defects are placed at a distance of **top)** $W = 17.5$nm, **bottom)** $W = 22.5$nm.

The size of our QDOT then allows the wavefunction to simultaneously interact with both defect sites. As mentioned before, we would like to produce avoided crossings in the level spacing landscape when traversing our QDOT potential from defect center 1 to defect center 2. Our first calculation, presented in Fig. 3.43 (top) , shows the resulting level spacing landscape for two double vacancies that are 175Å apart (blue) on top of the prior results with only one defect embedded (black). We clearly succeeded in forming avoided crossings which for levels 1,2,4 and 6 result are much smaller valley splitting Δ_j^k (approx. 20-40meV) than for the single-defect-system. Contrary to that, level 3 and 4 feature a slightly stronger splitting (approx. 60meV) in the two-defect system.

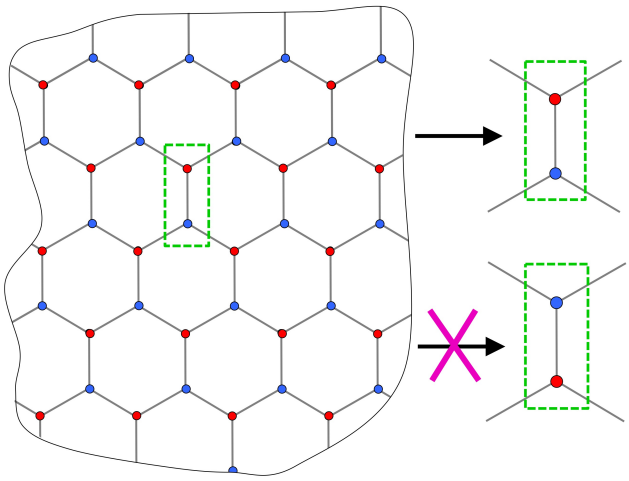

Figure 3.44.: Schematic explanation for the independence of the sublattice directionality (double vacancy) with respect to the specific embedding site of choice.

Inspecting the corresponding density plots of our QDOT states (Fig. 3.45) for both defects equidistant to the QDOT center shows other interesting features. The sublattice-projected density (to the right of every large total density plot) features the prominent directionality of the double vacancy. Strikingly, this directionality is the same for both defect sites. However this remarkable property is not specific to the particular embedding situation as can be easily understood with Fig. 3.44. When removing the two C atoms vertically (instead of the two other 120 deg inclined directions) we will inevitably remove the same A/B configuration (that is, for our sublattice counting, A on top of B) regardless of the specific pair chosen.

Recalculating these properties with the defects further apart (225Å) reveals a different set of avoided crossings (Fig. 3.43 bottom). Naively one would now expect narrower crossings throughout, since the average distance of the QDOT to a defect is larger. While this assumption holds for the lowest avoided crossings (1-2, 3-4), which are somewhat narrower, levels five and six are now further apart. This can be understood when remembering the fact that the higher states extend further towards the QDOT edge. Comparing state six in Fig. 3.45 and Fig. 3.46 shows an, at first glance, reasonably similar density distribution, however, focusing on the defect sites shows that the state is much more localized on the defects for $W = 175$Å, which could explain the decrease in energy and thus the reduced valley splitting.

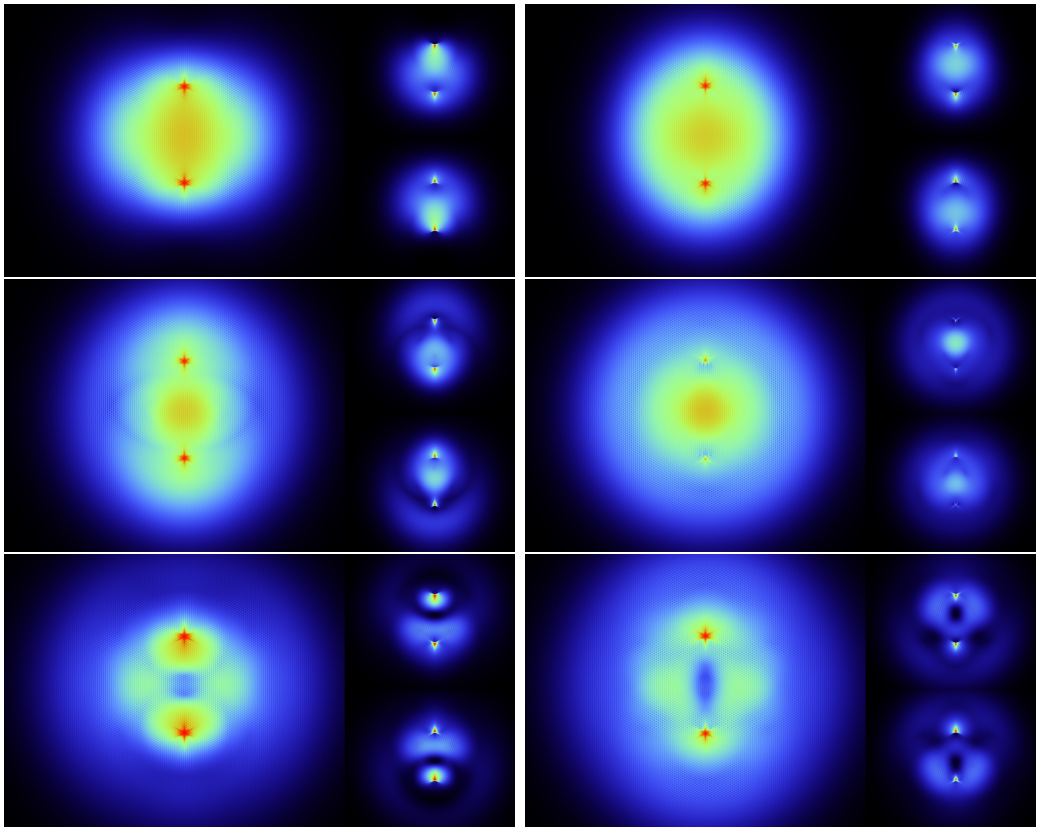

Figure 3.45.: Probability density of the first six QDOT states (with the QDOT potential centered between the two defect sites,W = 17.5nm) along with the densities present on each sublattice plotted in two smaller boxes stacked vertically to the right of each total density plot . Order: (top left) - D1, (top right) - D2, (center left) - D3, (center right) - D4, (bottom left) - D5, (bottom right) - D6, with D* indicating a Defect state.

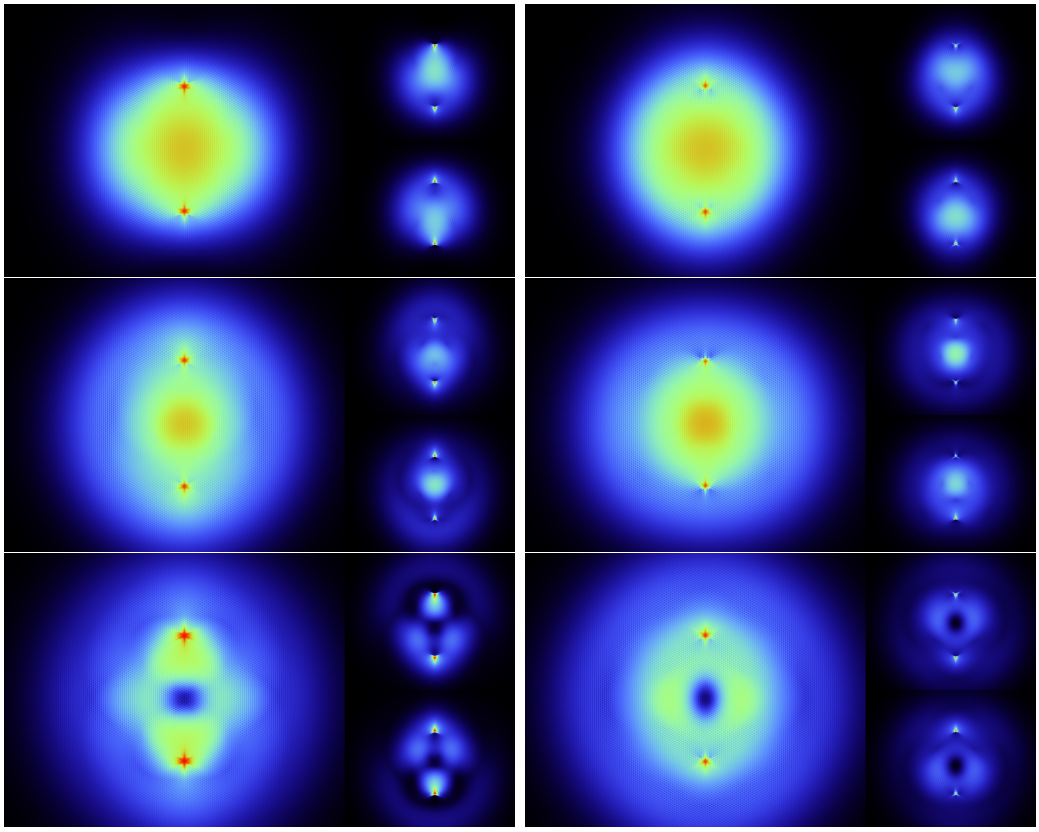

Figure 3.46.: Probability density of the first six QDOT states (with the QDOT potential centered between the two defect sites, $W = 22.5$nm) along with the densities present on each sublattice plotted in two smaller boxes stacked vertically to the right of each total density plot. Order: (top left) - D1, (top right) - D2, (center left) - D3, (center right) - D4, (bottom left) - D5, (bottom right) - D6, with D* indicating a Defect state.

As condensed in Fig. 3.47, we have shown that it is — to some extent — possible to tailor avoided crossings with specific widths by placing the defects in different distances to each other. While such control is simple in theory, experimental realization of a few well separated defects seems at least plausible and makes for possible interesting future comparisons.

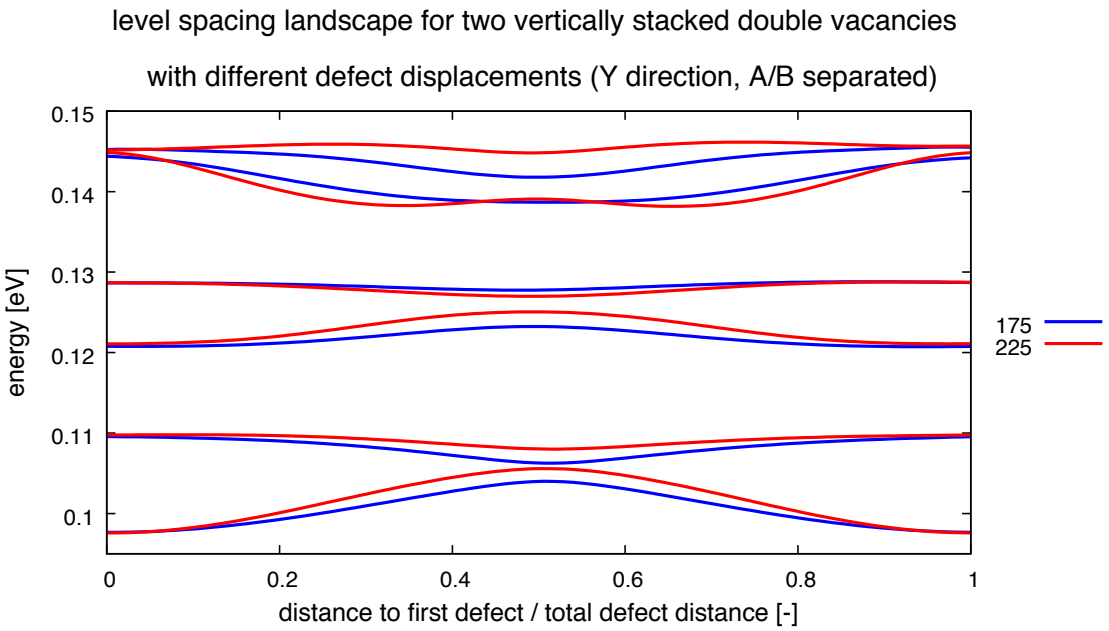

Figure 3.47.: Comparison of the level spacing landscape for two vertically stacked double vacancy defects embedded at distances $W = 175$Å (blue) and $W = 225$Å (red). Note that the x axis no longer depicts actual distances but measures them relative to the corresponding embedding distance W.

3.4.2. Two double-vacancies with relative rotation

While assuming somewhat controlled defect creation in an experimental setup we cannot realistically expect to accurately control the orientation of a directional defect type. That is we cannot control which of the three possible directions (120° rotated to each other, see Fig. 3.48) for a double vacancy will be realized at a specific site. If however there was a method with adequate reproducibility one could consider the relative angle as an additional parameter to influence the level spacing landscape. We briefly study the effects of different embedding directions by rotating one of the double vacancies by 120°.

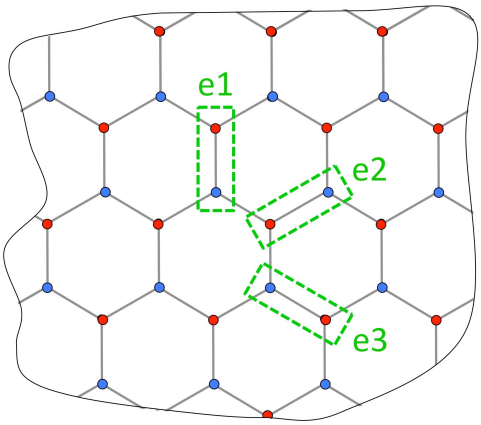

Figure 3.48.: Schematic depiction of the three possible directional (e1, e2, e3) realizations of a double vacancy defect.

Examining the resulting level spacing landscape we find that this change of direction for one of the defect sites leads to an asymmetric valleysplitting as can be seen in Fig. 3.49. There is however a much more fundamental change regarding the nature of our avoided crossings. This change appears to affect the three orbital levels quite differently.

We can, in fact, no longer really speak of an avoided crossing between the 1^{st} and 2^{nd} level for the rotated defect system since the nature of the respective wavefunctions no longer changes at the point of smallest valley splitting — as is the case for the unrotated system. By that we mean that the unrotated system abruptly swaps the ordering of the very pristine-like 1^{st} and 2^{nd} states at the halfway point between both defect sites. This happens for both defect-defect distances W that were investigated but remains completely absent when one of the defects is rotated 120°. The rotated system has robust pristine-like states (1^{st} and 2^{nd} levels) with their ordering determined by the unrotated defect (compare Fig. 3.50 and Fig. 3.43, unrotated defect always to the right). The influence of the rotated defect appears suppressed and is thus incapable of causing an abrupt change in the respective wavefunctions.

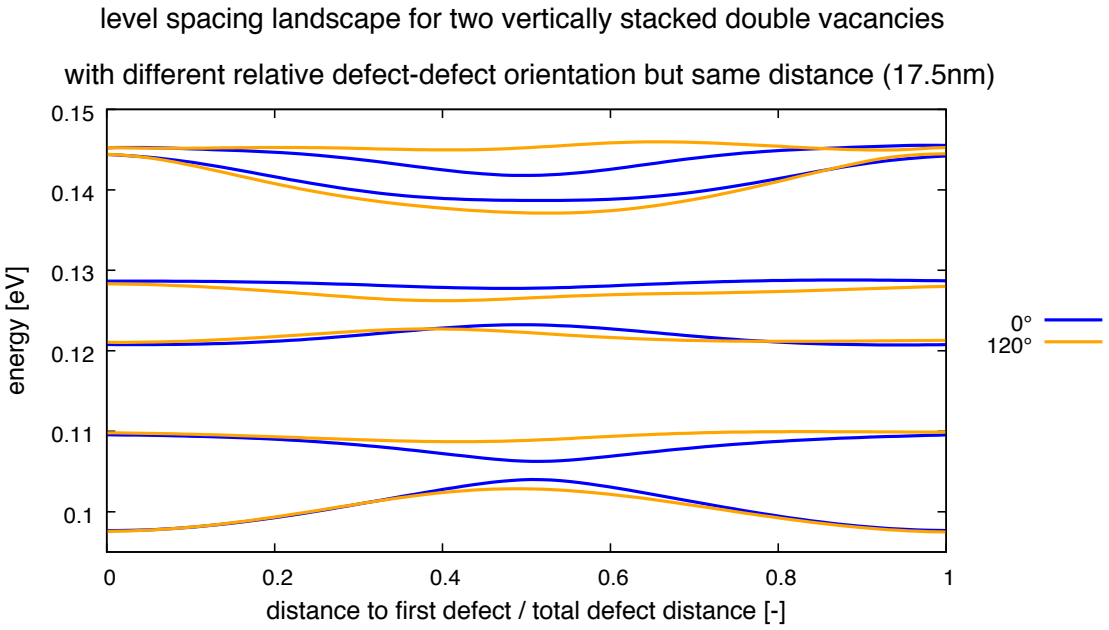

Figure 3.49.: Comparison of the level spacing landscape for two vertically stacked double vacancy defects embedded at distance W = 175Å.Blue line representing a system of equally oriented defects. Orange line representing a system with one defect (left side in plot) rotated 120°.

The position dependent valley splitting Δ_j^k of the highest investigated orbital (5^{th} and 6^{th} states) is significantly affected. The specific value at the halfway point is about twice as large as that in the unrotated system and resembles that of the larger defect-defect distance (Compare Fig. 3.50 and Fig. 3.47).

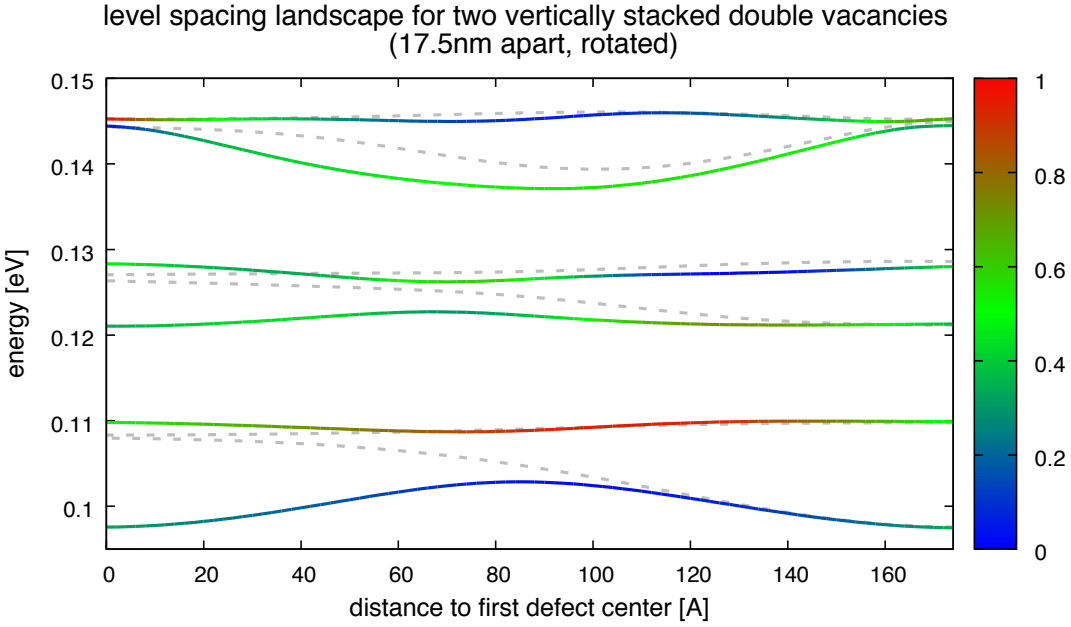

Figure 3.50.: Level spacing of the six lowest QDOT eigenstates depending on the relative distance of QDOT and defect center for the cases of a single defect embedded (grey dashed) and two double vacancy defects embedded with the color scale representing $|\langle \Psi_{\text{defect}} | \Psi_{\text{pristine}} \rangle|^2$. The defects are placed at a distance of $W = 17.5$nm with the top-defect rotated 120° (left in plot).

Checking our embedding by plotting the probability density of the 1^{st} QDOT level for both systems (equally oriented defects, top defect rotated 120°) we can clearly identify the top defect to be rotated (Fig. 3.51). The prominent directionality (north- / south- weighted projections on sublattices) acts as handy indicator for the defect orientation. We also notice that the second defect appears slightly more populated in the rotated system for both QDOT positions depicted (QDOT center congruent with top-defect position and QDOT center congruent with bottom-defect position) even though the defect-defect distance W is identical (up to restrictions due to lattice positions) in both systems.

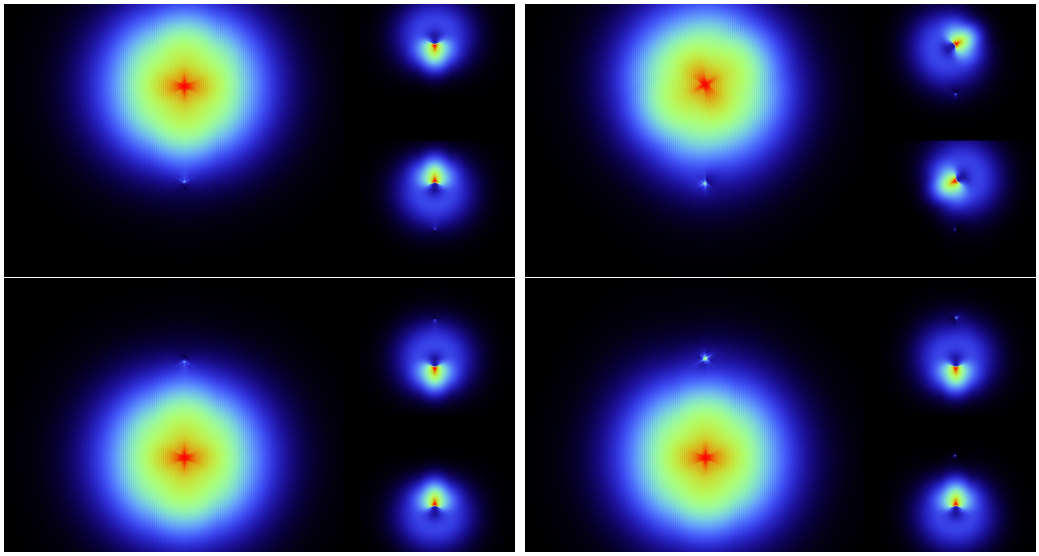

Figure 3.51.: Probability density of the first QDOT state of the **left column)** system with equally oriented double vacancy defects **right column)** system with two double vacancy defects rotated 120° relative to each other. Both systems feature the same defect-defect distance of $W = 17.5$nm. **row 1)** QDOT at top-defect site, **row 2)** QDOT at bottom-defect site.

We thus conclude that both defect-defect distance W and the relative orientation of the two double vacancies can in principle be used to actively manipulate the general level spacing landscape as well as specifically change the width (valley splitting Δ_j^k) of an avoided crossing. While experimental realization of such precise control will be challenging, there is always the option to simply recreate the specific defect realization achieved in experiment on a theoretic level.

4. Summary & Outlook

We have succeeded in producing a converged DFT calculation of the single vacancy defect. Vital insights from [11] and quite some computational effort (Vienna Scientific Cluster) helped in converging to the experimentally approved reconstruction with a magnetic moment of $2\mu_B$.. Next steps involve the wannierization of this DFT solution thus adding the single vacancy defect to our portfolio of wannierized DFT defects thereby providing a "tool" for future utilization in tight binding calculations (e.g quantum transport, spin scattering,...).

Improving embedding schemes (DFT $\rightarrow$ wannier $\rightarrow$ TB) for various graphene lattice defects by enforcing original defect symmetries that were lost due to the required periodicity of the DFT supercell and precise 10^{th} next-neighbour tight binding description throughout the system have proven critical for investigating the influence on the level spacing of an edgeless quantum dot in the vicinity of any such lattice defect.

We calculated the change in level spacing when traversing the lattice defect region with our QDOT potential in different directions. It is possible to predict the effects of a certain defect type to some extent via its geometrical properties (overall size, degree of sublattice symmetry breaking,...). We have however also found interesting directionality effects which for certain defect types (e.g. double vacancy defect) indicate that moving the QDOT away from the defect site in either +y direction or -y direction inverts the ordering within the (originally almost degenerate) sublattice subspaces.

Studying transition dynamics by smoothly accelerating the quantum dot in a prepared state followed by dynamically traversing the defect site allowed us to control the diabatic (or adiabatic) transition probability by tuning the QDOT velocity. Comparison with two level Landau Zener theory yields surprisingly good agreement, given the numerous approximations involved.

Lastly we tried tailoring an avoided crossing with a specific width by combining two double vacancy defects (aligned vertically at a distance W). Different embedding distances W and embedding orientations showed somewhat intuitive changes in the resulting width of the avoided crossing. Since the number of possible parameters of such a defect array seemingly explodes when considering already a handful of defects one might think of interesting configurations to be investigated in future projects.

5. Acknowledgements

The computational results presented, have been achieved [in part] using the Vienna Scientific Cluster (VSC).

Lastly I would like to thank all the people without whom this thesis would have been so much more consumptive and harder (if not impossible). Starting with my supervisor Florian Libisch, who always found a few minutes to answer my questions, Valerie Smeijkal for all the helpful discussions in group meetings, Thomas Fabian for his help with the time propagation code, to last but definitely not least Lukas Linhart who always put my many problems before his own work and thus saved me a lot of headaches.

Thank you Lili, for always making the occasional gloomy day so much brighter and my parents, whose unconditional love and support have helped me throughout my entire life.

References

[1] N. Freitag, L. Chizhova, P. Nemes-Incze, C. Woods, R. Gorbachev, Y. Cao, A. Geim, K. Novoselov, J. Burgdörfer, F. Libisch, M. Morgenstern, *"Electrostatically Confined Monolayer Graphene Quantum Dots with Orbital and Valley Splittings"*, Nano Lett. 2016, 16, 9, 5798-5805

[2] W. Nolting, *"Grundkurs Theoretische Physik 7 (Viel-Teilchen-Theorie)"*, 1997, Springer publishing company

[3] N. Freitag, T. Reisch, L. Chizhova, P. Nemes-Incze, C. Holl, C. Woods, R. Gorbachev, Y. Cao, A. Geim, K. Novoselov, J. Burgdörfer, F. Libisch, M. Morgenstern, *"Large tunable valley splitting in edge-free graphene quantum dots on boron nitride"*, Nature Nanotechnology **13**, 392-397 (2018)

[4] Thomas Ihn, *"Semiconductor Nanostructures (quantum states and electronic transport)"*, 2010, Oxford University Press

[5] Guido Burkard, *"Spintronik in Graphen"*, Physik Journal 13 (2014)

[6] A. A. Mostofi, J. R. Yates, G. Pizzi, Y.-S. Lee, I. Souza, D. Vanderbilt, N Marzari, *"An updated version of wannier90: A Tool for Obtaining Maximally Localised Wannier Functions"*, Comput. Phys. Commun. **185**, 2309 (2014)

[7] N Marzari, D. Vanderbilt, *"Maximally localized generalized Wannier functions for composite energy bands"*, Phys. Rev. B **56**, 12847 (1997)

[8] I. Souza, N Marzari, D. Vanderbilt, *"Maximally localized Wannier functions for entangled energy bands"*, Phys. Rev. B **65**, 035109 (2001)

[9] L. Linhart, J. Burgdörfer, F. Libisch *"Accurate modeling of defects in graphene transport calculations"*, Phys. Rev. B **97**, 035430 (2018)

[10] D. Kochan, S Irmer, M. Gmitra, J. Fabian, *"Resonant Scattering by Magnetic Impurities as a Model for Spin Relaxation in Bilayer Graphene"*, PRL **115**, 196601 (2015)

[11] A. M. Valencia, M. J. Caldas *"Single vacancy defect in graphene: Insights into its magnetic properties from theoretical modeling"*, Phys. Rev. B **96**, 125431 (2017)

[12] J. J. Palacios, J. Fernandez-Rossier, *"Vacancy induced magnetism in graphene and graphene ribbons"*, arXiv:0802.2029v1

[13] W. Kohn, F. Bassani, F. Funi, M. P. Tosi *"Highlights of Condensed Matter Theory"*, Amsterdam, 1985

[14] K. Capelle, C. A. Ullrich, G. Vignale, *"Degenerate ground states and non-unique potentials: breakdown and restoration of density functionals"*, arXiv:cond-mat/0610322v1

[15] K. Capelle, *"A Bird's-Eye View of Density-Functional Theory"*, Brazilian Journal of Physics vol. 36 no. 4A, (2006)

[16] H. Y. Chen, V. Apalkov, T. Chakraborty, *"Fock-Darwin States of Dirac Electrons in Graphene-Based Artificial Atoms"*, Phys. Rev. Lett. **97**, 186803 (2007)

[17] G. Giavaras, F. Nori, *"Tunable quantum dots in monolayer graphene"*, Phys. Rev. B **85**, 165446 (2012)

[18] G. Giavaras, P. A. Maksym, M. Roy, *"Magnetic field induced confinement-deconfinement transition in graphene quantum dots"*, J. Phys. **21**, 102201 (2009)

[19] C. Zener, *"Non-adiabatic crossing of energy levels"*, Proc. R. Soc. Lond. A 137 (1932)

[20] C. Wittig, *"The Landau Zener Formula"*, Journal of Physical Chemistry B, **109**, 8424-30 (2005)

[21] L. Linhart, (master thesis), *"Electron scattering in graphene by accurately modeled lattice defects"*, (2016)

[22] F. Libisch, S. Rotter, J. Güttinger, C. Stampfer, J. Burgdörfer, *"Transition to Landau levels in graphene quantum dots"*, Phys. Rev. B **81** 245411 (2010).

[23] S. Rotter, (PhD thesis), *"Ballistic quantum transport at high energies and high magnetic fields"*, 2004, Vienna University of Technology

[24] S. Rotter, (master thesis), *"A Modular Recursive Green's Function Method for Quantum Transport"*, 1999, Vienna University of Technology

[25] F. Libisch, (PhD thesis), *"Electronic structure and transport in mesoscopic devices"*, 2009, Vienna University of Technology

[26] A. Girschik, (PhD tesis) *"Scattering in Complex Media: Coherent Transport at the Cross-over to Anderson Localization"*, 2015, Vienna University of Technology

[27] K. S. Novoselov, V. I. Falko, L. Colombo, P.R. Gellert, M. G. Schwab, K. Kim,*"A roadmap for graphene"*, Nature **490** 11458 (2012).

[28] Z. Lenarcic, A. Ramsak, (lecture notes), *"Landau levels in graphene"*, 2010, Univerza v Ljubljani.

[29] T. Fabian, (master thesis), *"mode basis approach to quantum transport calculations"*, (2017)

[30] S. Sanvito, C. J. Lambert, J. H. Jefferson, A. M. Bratkovsky, *"General green's function formalism for transport calculations with spd Hamiltonians and giant magnetoresistance in co- and ni- based magnetic multilayers"* Phys. Rev. B **59** 11936 (1999).

[31] H.P. Boehm, A. Clauss, G.O. Fischer, U. Hofmann, *"Dünnste Kohlenstofffolien"* Z. Naturforschg. **17b** 150-153 (1962).

[32] T. Jawecki, W. Auzinger, O. Koch, *"Computable upper error bounds for Krylov approximations to matrix exponentials and associated ϕ-functions"*, arXiv:1809.03369v2 (2019).

[33] A. Hashimoto, K. Suenaga, A. Gloter, K. Urita, S. Iijima, *"Direct evidence for atomic defects in graphene layers"*, Nature (London) **430**, 870 (2004)

[34] J. Meyer, A. Geim, M. Katsnelson K. Novoselov, T. Booth, S. Roth, *"The structure of suspended graphene sheets"*, Nature (London) **446**, 60 (2007)

[35] M. Ugeda, I. Brihuega, F. Guinea, J. Gomez-Rodriguez, *"Missing atom as a source of carbon magnetism"*, Phys. Rev. Lett. **104**, 096804 (2010)

[36] A. Robertson, B. Montanari, K. He, C. Allen, Y. Wu, N. Harrison, A. Kirkland, J. Warner, *"Structural reconstruction of the graphene monovacancy"*, ACS Nano **7**, 4495 (2013)

[37] Y. Zhang, S. Li, H. Huang, W. Li, J. Qiao, W. Wang, L. Yin, K. Bai, W. Duan, L. He, *"Scanning tunneling microscopy of the π-magnetism of a single carbon vacancy in graphene"*, Phys. Rev. Lett. **117**, 166801 (2016)

[38] A. Castro Neto, F. Guinea, N. Peres, K. Novoselov, A. Geim, *"The electronic properties of graphene"*, Rev. Mod. Phys. **81**, 109-162 (2009)

[39] G. Kresse and J. Hafner, *"Ab initio molecular dynamics for liquid metals"*, Phys. Rev. B **47**, 558 (1993)

[40] G. Kresse and J. Hafner, *"Ab initio molecular-dynamics for the liquid-metal amorphous-semiconductor transition in germanium"*, Phys. Rev. B **49**, 14251 (1994)

[41] G. Kresse and J. Furthmüller, *"Efficiency of ab-initio total energy calculations for metals and semiconductors using a plane-wave basis set"*, Comput. Mater. Sci. **6**, 15 (1996)

[42] G. Kresse and J. Furthmüller, *"Efficient iterative schemes for ab-initio total-energy calculations using a plane-wave basis set"*, Phys. Rev. B **54**, 11169 (1996)

[43] M. Morgenstern, N. Freitag, A. Nent, P. Nems-Incze, M. Liebmann, *"Graphene Quantum Dots Probed by Scanning Tunneling Microscopy"*, Ann. Phys. **529**, 1700018 (2017)

[44] K. Novoselov, A. Geim, S. Morozov, D. Jiang, Y. Zhang, S. Dubonos, I. Grigorieva, A. Firsov, *"Electric Field Effect in Atomically Thin Carbon Films"*,Science **306**, 666 (2004)

[45] F. Bonaccorso, A. Lombardo, T. Hasan, Z. Sun, L. Colombo, A. Ferrari, *"Production, Processing and Placement of Graphene and Two Dimensional Crystals"*, Mat. Today **15**, 564 (2012)

[46] D. Abergel, V. Apalkov, J. Berashevich, K. Ziegler, T. Chakraborty, *"Properties of Graphene: A Theoretical Perspective"*, Adv. Phys. **59**, 261 (2010)

[47] T. Chakraborty,*"Quantum Dots"*, 1999, Elsevier Science

[48] P. Recher, B. Trauzettel, *"Quantum dots and spin qubits in graphene"*, Nanotechnology **21**, 302001 (2010)

[49] K. Ono, D. Austing, Y. Tokura, S. Tarucha, *"Current Rectification by Pauli Exclusion in a Weakly Coupled Double Quantum Dot System"*, Science **299**, 679 (2003)

[50] P. Recher, E. Sukhorukov, D. Loss, *"Quantum Dots as Spin Filter and Spin Memory"*, Phys. Re. Lett. **85**, 1962 (2000)

[51] R. Hanson, L. Kouwenhoven, J. Petta, S. Tarucha, L. Vandersypen, *"Spins in few-electron quantum dots and Spin Memory"*, Rev. Mod. Phys. **79**, 1217 (2007)

[52] M. Katsnelson, K. Novoselov, A. Geim, *"Chiral tunneling and the Klein paradox in graphene"*, Nature Physics **2**, 620-625 (2006)

[53] S. Schnez, K. Ensslin, M. Sigrist, T. Ihn, *"Analytic model of the energy spectrum of a graphene quantum dot in a perpendicular magnetic field¨*, Phys. Rev. B **78**, 195427 (2008)

List of Figures

A. Relativistic Landau levels

The change in quantization for the energy of an electron moving through a solid with a finite magnetic field applied is known as the formation of Landau-levels. Since the dispersion relation of graphene, when restricted to one of the Dirac cones, equals that of a massless Dirac fermion which can be described via the Dirac equation, one can simply apply the formalism of minimal coupling to this manifestly Lorentz-invariant equation to derive the eigenenergies of the Landau levels.

Starting with a homogeneous magnetic field $\vec{B}$ in z-direction and a vector potential $\vec{A}$ in Coulomb gauge (A.1).

$$\vec{B} \coloneqq \begin{pmatrix} 0 \\ 0 \\ B \end{pmatrix} \qquad \vec{\nabla} \cdot \vec{A} \coloneqq 0 \qquad \vec{A} = B \begin{pmatrix} -y \\ 0 \\ 0 \end{pmatrix} \tag{A.1}$$

We insert this vector potential via minimal coupling in a Weyl equation which is the simpler case of the Dirac equation for massless fermions that only involves a two-dimensional spinor. Making use of the low dimensionality of graphene, $p_z = 0$, yields a system of two equations (A.2).

$$v_{Fermi} \cdot \underbrace{\left(\vec{p} - \frac{e}{c}\vec{A}\right) \cdot \vec{\sigma}}_{\vdots} \cdot \begin{pmatrix} u \\ v \end{pmatrix} = E \cdot \begin{pmatrix} u \\ v \end{pmatrix} \tag{A.2}$$

$$\overbrace{\begin{bmatrix} 0 & \left(\hat{p}_x - \frac{e}{c}\hat{A}_x\right) - i\left(\hat{p}_y - \frac{e}{c}\underbrace{\hat{A}_y}_{=0}\right) \\ \left(\hat{p}_x - \frac{e}{c}\hat{A}_x\right) + i\left(\hat{p}_y - \frac{e}{c}\underbrace{\hat{A}_y}_{=0}\right) & 0 \end{bmatrix}}^{\vdots}$$

Expressing the spinor component v in the lower line and inserting into the upper one gives:

$$v_F^2 \cdot \left[\hat{p}_x - i\hat{p}_y - \frac{e}{c}\hat{A}_x\right] \cdot \left[\hat{p}_x + i\hat{p}_y - \frac{e}{c}\hat{A}_x\right] \cdot u = E^2 \cdot u \tag{A.3}$$

$$\left[\hat{p}_x^2 + \hat{p}_y^2 + i\frac{e}{c}\underbrace{\left[\hat{p}_y, \hat{A}_x\right]_-}_{i\hbar B} + \frac{e^2B^2}{c^2}\hat{y}^2 - 2\frac{e}{c}B\hat{p}_x\hat{y}\right] \cdot u = \underbrace{\frac{E^2}{v_F^2}}_{:=\epsilon} \cdot u \tag{A.4}$$

$$\left[\hat{p}_y^2 + \underbrace{\hat{p}_x^2 + \frac{e^2B^2}{c^2}\hat{y}^2 - 2\frac{e}{c}B\hat{p}_x\hat{y}}_{\frac{e^2B^2}{c^2}\left(\hat{y} - \frac{c}{eB}\hat{p}_x\right)^2}\right] \cdot u = \underbrace{\left[\epsilon + \underbrace{\frac{eB\hbar}{c}}_{\text{"energy shift"}}\right]}_{\epsilon'} \cdot u \tag{A.5}$$

Identifying a constant shift to the energy scale and completing the square (A.5) results in an equation that can be interpreted as a harmonic oscillator with the frequency ω (A.6) and thus delivers quantized eigenenergies (A.7) which ultimately lead to the relativistic Landau levels of graphene:

$$\left[\hat{p}_y^2 + \frac{m\omega^2}{2}(\hat{y} - \hat{y}_0)^2\right] u = \epsilon' u \qquad \text{with} \qquad \omega = 2\frac{eB}{c} \tag{A.6}$$

$$\epsilon_n' = \hbar\omega(n + \frac{1}{2}) \stackrel{!}{=} \frac{E^2}{v_F^2} + \frac{\hbar eB}{c} \tag{A.7}$$

$$E_n = v_F \cdot sgn(n)\sqrt{\frac{2\hbar e}{c}|B||n|} \qquad \text{with} \qquad n \in \mathbb{Z} \tag{A.8}$$

The linear dispersion relation of graphene, caused by its resemblance to the Dirac equation for massless particles, leads to Landau levels with a square root dependence on the magnetic field in contrast to "ordinary" Landau levels that linearly depend on B.